

**Multicomponent Approaches for the Generation of Structurally Diverse  
Microporous Coordination Polymers**

by

Ananya Dutta

A dissertation submitted in partial fulfillment  
of the requirements for the degree of  
Doctor of Philosophy  
(Chemistry)  
in The University of Michigan  
2015

Doctoral Committee:

Professor Adam J. Matzger, Chair  
Assistant Professor Pavel Nagorny  
Professor Melanie S. Sanford  
Assistant Professor Donald J. Siegel

© Ananya Dutta 2015  
All Rights Reserved

*Dedicated to my sister*

*Dr. Arpita Dutta*

## **Acknowledgements**

I would first like to thank my research advisor Professor Adam J. Matzger for mentoring me throughout my graduate career. I am also very thankful to Professor Melanie S. Sanford, Professor Pavel Nagorny, and Professor Donald J. Siegel for serving on my dissertation committee. My countless thanks go to the all past and present members of Matzger lab: Antek, Koh, Jenny, Austin, Eranda, Jeremy, Onas, Rachel, Kira, Leah, Ping, Jake, Jon, Raj, LiZi, Laura, Kortney, Amanda, Rosalyn, Ly, Jialiu, and Kyle. Especially, I greatly appreciate Dr. Antek Wong-Foy's assistance in sorption and crystallography related experiments. I thank the Department of Chemistry at University of Michigan for providing an excellent set of facilities and a vibrant departmental staff. A special thanks goes to Dr. Jeff Kampf without whose help many of my crystal structures would remain unpublished. I also highly appreciate assistance from Dr. Alexandrov Evgeny at Samara State University and Professor Davide M. Proserpio at Universita' degli Studi di Milano regarding TOPOS and discussion on net. At last, I am ever grateful to my family and Dipanjan who have encouraged me relentlessly and demonstrated immense amount of patience to deal with me.



## Table of Contents

Dedication.....	ii
Acknowledgements.....	iii
List of Figures.....	vii
List of Tables.....	xii
Abstract.....	xiii
Chapter 1 Introduction.....	1
1.1 Traditional Porous Materials.....	1
1.2 Microporous Coordination Polymers.....	3
1.3 Synthetic Strategies for Production of MCPs.....	4
1.3.1 Coordination Polymerization.....	4
1.3.2 Coordination Copolymerization.....	6
1.4 Organization of Thesis.....	13
1.4.1 Coordination Copolymerization of Three Carboxylate Linkers into a Pillared-layer Framework.....	13
1.4.2 A Non-regular Layer Arrangement of a Pillared-layer Coordination Polymers: Avoiding Interpenetration via Symmetry Breaking at Nodes.....	15
1.4.3 Porous Solids Arising from Synergistic and Competing Modes of Assembly: Combining Coordination Chemistry and Covalent Bond Formation.....	16
1.5 References.....	18
Chapter 2 Coordination Copolymerization of Three Carboxylate Linkers into a Pillared-layer Framework.....	21
2.1 Introduction.....	21
2.2 Results and Discussion.....	23
2.3 Conclusions.....	31
2.4 Experimental Section.....	31
2.4.1 Synthesis of MCPs.....	31

2.4.2 PXRD Patterns of UMCM-10, -11, and -12.....	32
2.4.3 Single Crystal X-Ray Diffraction for UMCM-10 and -12.....	36
2.4.4 <sup>1</sup> H NMR Spectroscopic Data for UMCM-10, -11, and -12.....	38
2.4.5 TGA Traces of UMCM-10, -11, and -12.....	40
2.4.6 Gas Sorption Measurements of UMCM-4, -10, -11, and -12.....	41
2.4.7 PXRD Patterns of UMCM-4, -10, and -12 at Elevated Temperatures and Air..	46
2.4.8 Microscopic Images of Dye Diffusion Experiments.....	50
2.4.9 Linear Dichroism Experiment on UMCM-4 Crystals.....	53
2.5 References.....	54
Chapter 3 A Non-regular Layer Arrangement of a Pillared-layer Coordination Polymer: Avoiding Interpenetration via Symmetry Breaking at Nodes.....	57
3.1 Introduction.....	57
3.2 Results and Discussion.....	59
3.3 Conclusions.....	64
3.4 Experimental Section.....	64
3.4.1 Synthesis of UMCM-15.....	64
3.4.2 Morphology of UMCM-15.....	65
3.4.3 <sup>1</sup> H NMR Spectroscopic Data of Digested UMCM-15.....	66
3.4.4 Structural Modelling and X-ray Diffraction Analyses.....	66
3.4.5 Nile Red Diffusion Experiments.....	70
3.4.6 TGA Trace of UMCM-15.....	70
3.4.7 Activation of UMCM-15 and Gas Sorption Experiments.....	71
3.5 References.....	71
Chapter 4 Porous Solids Arising from Synergistic and Competing Modes of Assembly: Combining Coordination Chemistry and Covalent Bond Formation.....	73
4.1 Introduction.....	73
4.2 Results and Discussion.....	74
4.3 Conclusions.....	82
4.4 Experimental Section.....	83
4.4.1 Synthesis of Materials.....	83
4.4.2 PXRD Patterns of MOF-177-NH <sub>2</sub> , UMCM-306, -307, and -308.....	86

4.4.3 Single Crystal X-ray Diffraction for UMCM-306.....	87
4.4.4 <sup>1</sup> H NMR Spectroscopic Data of Digested MOF-177-NH <sub>2</sub> , UMCM-306, -307, and -308.....	88
4.4.5 Raman Spectroscopic Data of MOF-177-NH <sub>2</sub> , UMCM-306, and -308.....	89
4.4.6 Microscopic Images after Aging Experiments.....	91
4.4.7 TGA Traces of MOF-177-NH <sub>2</sub> , UMCM-306, -307, and -308.....	92
4.4.8 Activation of Materials and Gas Sorption Experiments.....	93

## List of Figures

Figure 1. 1. Example structure of a zeolite (sodalite).....	2
Figure 1. 2. Synthesis scheme of MOF-5 and structure of MOF-5 constructed from $Zn_4O(O_2CR)_6$ and BDC linker. ....	4
Figure 1. 3. Linker extension from BDC to 2,6-naphthalenedicarboxylate (NDC) promotes twofold interpenetration of <i>pcu</i> frameworks.....	6
Figure 1. 4. Structure of pillared-layer MCP $[Cu_2(pzdc)_2(L)]_n$ viewed along different axes. ....	7
Figure 1. 5. a) Pillared-layer structure and b) layer arrangement of DMOF $[Zn_2(BDC)_2(DABCO)]_n$ .....	8
Figure 1. 6. Schematic showing coordination copolymerization of multiple linkers of same length and coordinating functionalities, however decorated with different non-coordinating functional groups. The first illustration is for random copolymerization and the second one shows formation of a core-shell architecture via controlling the order of precursors' addition.....	10
Figure 1. 7. Small variations of relative linker length of UMCM-1 give rise to completely new frameworks of distinct topologies.....	11
Figure 1. 8. An increase in linker length from BDC in UMCM-1 to T <sup>2</sup> DC results into formation of a completely new structure UMCM-2.....	12
Figure 1. 9. Coordination terpolymerization of three carboxylate linkers (two involved in layer formation and one serving as pillar) into a pillared-layer framework. ....	14
Figure 1. 10. Schematic comparing commonly observed layer arrangement stemming from a single dicarboxylate linker and the layer arrangement originating from combination of linkers around the metal nodes. ....	15
Figure 1. 11. Conceptual representation of different materials generated from coordination processes only (in absence of the dialdehyde) and combination of coordination processes and imine formation (in presence of the dialdehyde). ....	17

Figure 2. 1. Conceptual representation of the construction of different 3D networks from a 2D layer (composed of two linkers and SBU in all cases) connected <i>via</i> pillars (varying in pillar length).	22
Figure 2. 2. Linker combinations yielding pillared-layer MCPs with the $Zn_4O(O_2CR)_6$ SBU ....	24
Figure 2. 3. PXRD patterns of MCPs. The (020) reflections correspond to half of the layer spacings.....	25
Figure 2. 4. Structures of (a) UMCM-4 (b) UMCM-10 (c) UMCM-11 (generated from model) and (d) UMCM-12. The 2D layer (e) is preserved in each structure and illustrated for UMCM-4. Different pore dimensions are measured with subtraction of the van der Waals radii of the atoms.....	26
Figure 2. 5. a) Nitrogen sorption isotherms and b) sorption traces in the low pressure region for UMCM-4, -10, -11, and -12.....	28
Figure 2. 6. Summary of size exclusion results for dye incorporation into UMCM-4, -10, -11, and -12. Nile red, Reichardt's dye, and Coomassie Brilliant Blue G are represented in violet, light brown, and light blue spheres. The color of the shown Sectioned crystals indicate success or failure of dye impregnation into the corresponding MCP crystals.....	30
Figure 2. 7. PXRD patterns of UMCM-10 (black: simulated, red: as synthesized, blue: activated). .....	33
Figure 2. 8. PXRD patterns of UMCM-11 (black: simulated, red: as synthesized, blue: activated). .....	34
Figure 2. 9. PXRD patterns of UMCM-12 (black: simulated, blue: as synthesized, red: activated). .....	34
Figure 2. 10. PXRD patterns of MCP synthesized using terphenyl pillar linker (black: simulated, red: experimental). ....	35
Figure 2. 11. PXRD patterns of MCP synthesized using biphenyl pillar linker (black: simulated, red: experimental). ....	35
Figure 2. 12. $^1H$ NMR spectrum of activated UMCM-10 digested in 20% DCI in $D_2O$ diluted with $d^6$ -DMSO. ....	38
Figure 2. 13. $^1H$ NMR spectrum of activated UMCM-11 digested in 20% DCI in $D_2O$ diluted with $d^6$ -DMSO. ....	39

Figure 2. 14. <sup>1</sup> H NMR spectrum of activated UMCM-12 digested in 20% DCl in D <sub>2</sub> O diluted with d <sup>6</sup> -DMSO. ....	39
Figure 2. 15. TGA trace of activated UMCM-11. ....	40
Figure 2. 16. TGA trace of activated UMCM-10. ....	40
Figure 2. 17. TGA trace of activated UMCM-12. ....	41
Figure 2. 18. Self-consistency plots for determining P/P <sub>0</sub> range for BET analysis based on isotherms shown in Figure 2.5. ....	43
Figure 2. 19. Pore size distribution of activated UMCM-4. ....	43
Figure 2. 20. Pore size distribution of activated UMCM-10. ....	44
Figure 2. 21. Pore size distribution of activated UMCM-12. ....	44
Figure 2. 22. H <sub>2</sub> sorption isotherms of UMCM-4 (purple), -12 (orange), and -10 (blue) .....	45
Figure 2. 23. CO <sub>2</sub> sorption isotherms of UMCM-4 (purple), -12 (orange), and -10 (blue).....	45
Figure 2. 24. PXRD patterns of activated UMCM-10 at different temperatures.....	47
Figure 2. 25. PXRD patterns of activated UMCM-4 at different temperatures.....	46
Figure 2. 26. PXRD patterns of activated UMCM-12 at different temperatures.....	47
Figure 2. 27. PXRD patterns of activated UMCM-4 before and after exposure to air.....	48
Figure 2. 28. PXRD patterns of activated UMCM-10 before and after exposure to air.....	48
Figure 2. 29. PXRD patterns of activated UMCM-12 before and after exposure to air.....	49
Figure 2. 30. Microscopic images of dyed crystals of UMCM-4, -10, -11, and -12 after Nile red dye diffusion. ....	50
Figure 2. 31. Microscopic images of dyed crystals of UMCM-4, -10, -11, and -12 after Reichardt's dye diffusion.....	51
Figure 2. 32. Microscopic images of dyed crystals of UMCM-4, -10, -11, and -12 after Coomassie Brilliant Blue dye diffusion.....	52
Figure 2. 33. Kinetic diameters of dye molecules were approximated using the minimum cross-sectional area and taking van der Waals radii of atoms into account. ....	53
Figure 2. 34. Microscopic images of UMCM-4 crystal housing oriented Nile Red dye molecules taken before and after 90° rotation with respect to plane polarized light. Exposure time was held constant.....	54

Figure 3. 1. Plausible arrangements of m short (red) and n long (blue) linkers around a 4-connected metal paddlewheel node (purple) ( $m+n=4$ ) and resultant layer structures from self-repetition of these units. ....	58
Figure 3. 2. a) Pillared-layer structure of UMCM-15 and b) layer arrangement of UMCM-15 showing a square and a rectangular pore window. Pore dimensions are measured with subtraction of the van der Waals radii of the atoms. ....	61
Figure 3. 3. Schematic of size exclusion results for Nile red incorporation into the pores of $[\text{Zn}_2(\text{BDC})_2(\text{bipy})]_n$ , $[\text{Zn}_2(\text{NDC})_2(\text{bipy})]_n$ , and UMCM-15. Nile red is represented in the purple sphere. The color of crystals indicate if dye is incorporated into corresponding MCP crystals...	62
Figure 3. 4. Nitrogen isotherm of activated UMCM-15 showing hysteresis.....	63
Figure 3. 5. a) Optical micrograph and b) scanning electron micrograph of UMCM-15.....	65
Figure 3. 6. Aromatic region of $^1\text{H}$ NMR spectra for digested UMCM-15.....	66
Figure 3. 7. Pawley refinement results from simulated and experimental powder X-ray diffraction pattern of UMCM-15 .....	67
Figure 3. 8. TGA trace of activated UMCM-15 .....	70
Figure 4. 1. Conceptual representation of different materials generated from coordination processes only and combination of coordination processes and imine formation.....	74
Figure 4. 2. PXRD patterns of MOF-177-NH <sub>2</sub> (black), UMCM-306 (green), UMCM-307 (red), and UMCM-308 (grey).....	75
Figure 4. 3. Structures of materials: a) MOF-177-NH <sub>2</sub> , b) UMCM-306, c) UMCM-307, and d) UMCM-308. (a, c, and d are generated from the models and validated by powder X-ray diffraction data; b is obtained from single X-ray diffraction data).....	77
Figure 4. 4. Optical micrographs of UMCM-306 and MOF-177-NH <sub>2</sub> at different delay times (t in hr) of terephthalaldehyde addition.....	78
Figure 4. 5. Comparison of the linker orientations in CS1 (a and b) and underlying network topologies (c and d) of two polymorphic frameworks NH <sub>2</sub> -MOF-177 and UMCM-308 constructed from same 6-connected and 3-connected nodes.....	81
Figure 4. 6. Nitrogen sorption isotherms for MOF-177-NH <sub>2</sub> (black), UMCM-306 (green), and UMCM-307 (red).....	82
Figure 4. 7. Comparison of simulated and as-synthesized PXRD patterns of materials .....	87

Figure 4. 8. $^1\text{H}$ NMR spectra of digested MOF-177-NH <sub>2</sub> , UMCM-306, -307, and -308.....	89
Figure 4. 9. Full Raman spectra of materials showing presence of imine C=N stretching at 1634 cm <sup>-1</sup> in UMCM-306 and NH <sub>2</sub> stretching in MOF-177-NH <sub>2</sub> and UMCM-308 at ~3400 cm <sup>-1</sup> . .....	90
Figure 4. 10. Partial Raman spectra of materials showing presence of imine C=N stretching at 1634 cm <sup>-1</sup> in UMCM-306 and NH <sub>2</sub> stretching in MOF-177-NH <sub>2</sub> and UMCM-308 at ~3400 cm <sup>-1</sup> . .....	90
Figure 4. 11. TGA traces of activated materials .....	94



## List of Tables

Table 2. 1. Crystal data and structure refinement for UMCM-10 and -12 .....	37
Table 2. 2. Predicted and experimental surface areas for activated materials obtained from N <sub>2</sub> isotherms.....	42
Table 3. 1. Pawley refinement results of UMCM-15.....	67
Table 3. 2. Refined cell parameters and fractional atomic coordinates of UMCM-15.....	67
Table 4. 1. Crystal data and structure refinement for UMCM-306 .....	88

## **Abstract**

Microporous coordination polymers (MCPs), materials built from metal clusters bridged with organic linkers, constitute a rapidly growing class of porous solids. The conventional synthetic strategies for production of MCPs involve coordination polymerization of one type linker with a single metal. Despite the success of this method, there exist several challenges with regard to producing highly porous and commercially viable MCPs. These disadvantages include interpenetration of frameworks upon linker extension causing a reduction in porosity and the requirement for synthetically complex linkers to achieve high porosity leading to a drastic increase in cost. This thesis is focused on multicomponent approaches for synthesis of structurally diverse MCPs. In addition, using multiple building units enables suppression of interpenetration, higher predictability over network topology, and an overall reduction in cost. Chapter 2 describes a coordination copolymerization approach of three carboxylate linkers; this strategy was employed to generate a series of isorecticular (having the same network topology) pillared-layer MCPs wherein structures were tuned uniaxially via controllable replacement of pillar linker. Moreover, pillar linker extension occurred in absence of interpenetration resulting in highly porous MCPs. The coordination terpolymerization strategy described in chapter 2 is also exploited to alter the connectivity within the layer arrangement of a pillared-layer MCP in chapter 3. Using a mixture of commercially available linkers of differing lengths enabled formation of a pillared-layer MCP with a non-regular layer structure and no interpenetration. In

chapter 4 the power of the multicomponent approach is leveraged through covalent bond formation in tandem with coordination chemistry. A linker was designed which allows either coordination processes or a combination of coordination processes and covalent bond formation to occur in presence of Zn(II). Upon addition of various reaction partners, materials with variable architectures and pore characteristics are obtained. This approach, in addition to being a compelling material discovery method, also offers a fundamental understanding of factors influencing the two distinct modes of assembly.

# Chapter 1

## Introduction

### 1.1 Traditional Porous Materials

Porous carbonaceous materials are one of the earliest classes of porous solids. The use of porous carbon as an industrial sorbent has been reported as early as the 1700s<sup>1</sup> demonstrating its role as a decolorizing agent in cane sugar refining process. High surface area carbons are currently one of the most widely employed industrial sorbents finding use in a variety of applications including water<sup>2</sup> and gas<sup>3</sup> purification, catalyst supports,<sup>4, 5</sup> and adsorption-based fuel storage and delivery.<sup>6, 7</sup> Activated carbons possess high porosity and surface area.<sup>8</sup> Although there exists a number of models<sup>9</sup> representing the structure of activated carbon, the basic unit consists “a twisted network of defective hexagonal carbon layers, cross-linked by aliphatic bridging groups”.<sup>10</sup> The physical properties of activated carbons such as interlayer spacing, pore volume, and surface area may vary depending on synthetic conditions.<sup>11</sup> Despite its wide use, activated carbons have several drawbacks, especially from the standpoint of having a disordered structure and a lack of structural tunability.

Porous inorganic solids are well-known alternatives to activated carbon. Studies on porous inorganic solids, although some occur naturally, began near mid-1700s.<sup>12</sup> Porous inorganic crystalline solids broadly include two main categories of materials: aluminosilicates<sup>13</sup> and aluminophosphates. Zeolites are “3D crystalline, hydrated alkaline or alkaline-earth

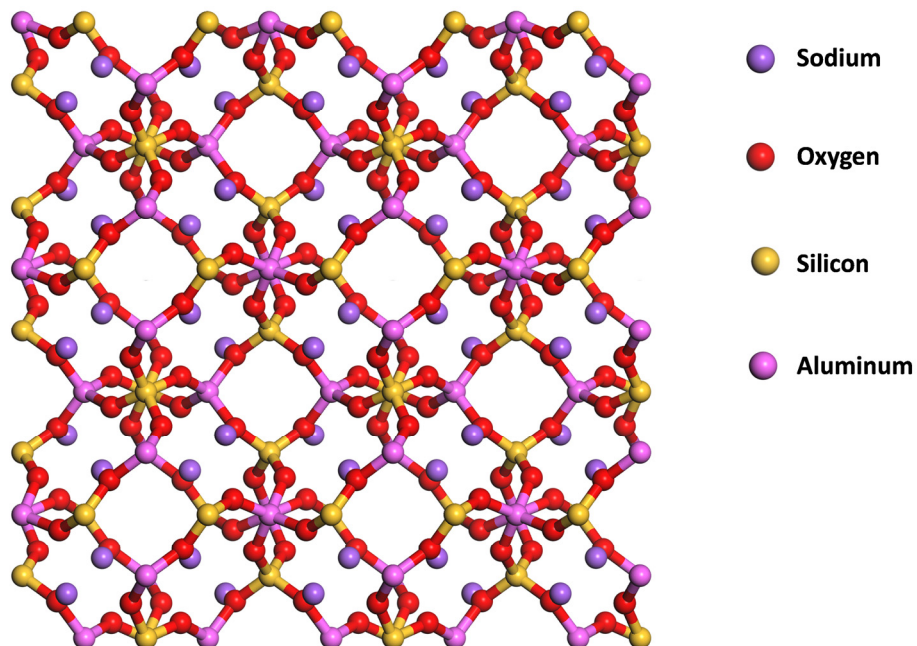


Figure 1. 1. Example structure of a zeolite (sodalite).

aluminosilicates with the general formula  $M^{n+}_{x/n}[(AlO_2)_x(SiO_2)_y]^{x-} \cdot wH_2O$  ( $M$ =metal)<sup>10</sup> which possesses an ordered structure contrary to activated carbons (Figure 1.1). The backbone of a zeolite framework is comprised of Al and Si atoms situated in tetrahedral holes and connected via oxide (-O-) linking units giving rise to a porous network. The pore space often includes  $M^{n+}$  ions and water molecules.<sup>14</sup> The porosity can be exposed via the elimination of water molecules or other labile guests. Synthetic zeolites were first created in 1862.<sup>15</sup> The porosity of zeolites is widely exploited in molecular sieving,<sup>16</sup> gas and liquid phase separations,<sup>17</sup> ion exchange,<sup>18</sup> and catalytic processes.<sup>19</sup> On the other hand, aluminophosphates, structurally similar to zeolites, consists of Al and P atoms in tetrahedral holes connected by oxygen atoms leading to a porous network. Some of the P atoms in aluminophosphates are often synthetically replaced by Si atoms which generates a negatively charged framework and the charge is balanced by insertion of protons. This mechanism gives rise to a chemically distinct silicoaluminophosphates network endowed with Brønsted acidity.<sup>20</sup> The first publication on microporous crystalline

aluminophosphates appeared in 1982 from a group Union Carbide researchers.<sup>21</sup> Thereafter they have been applied to a variety of applications, primarily as molecular sieves<sup>22</sup> and in catalysis.<sup>23</sup>

## 1.2 Microporous Coordination Polymers (MCPs)

Until 1989, the field of porous solids was dominated by activated carbons and porous inorganic materials. In 1989, Robson and coworkers reported a coordination polymer<sup>24</sup> of diamondoid topology constructed from a tetratopic organic linker, 4,4',4'',4'''-tetracyanotetraphenylmethane and Cu(I) metal ions. This publication<sup>25</sup> first demonstrated a design principle for synthesis of coordination polymers where the geometries of the metal ion and organic linker could be translated to an expected topology of the resultant coordination network. Subsequent publications<sup>26, 27</sup> by Robson and coworkers illustrated that a variety of coordination polymers with tunable architectures can be available based on distinct geometries of the organic linkers and metal ions. However, porosity of these coordination polymers was not studied as they suffered from a lack of stability upon guest removal. A decade later the groups of Yaghi and Williams separately synthesized two MCPs, MOF-5<sup>28</sup> and HKUST-1,<sup>29</sup> which are presently considered the most extensively studied and archetypal MCPs (metal-organic framework is abbreviated as MOF and HKUST stands for Hong-Kong University of Science and Technology<sup>30</sup>). MOF-5 (Figure 1.2) and HKUST-1 showed superior stability upon guest removal and high accessible porosities were evidenced by gas sorption as contrasted to those MCPs reported by the Robson group. In 2004, MOF-177,<sup>31</sup> a highly porous MCP was reported which set a record for the highest surface area porous solid by exceeding the surface area values of activated carbons or zeolites. After the publication of these materials, the field of MCP attracted tremendous interest due to two primary reasons: a) a combination of versatility of the precursors and highly ordered structures<sup>32</sup> which was unseen or difficult to achieve in activated carbons and

porous inorganic solids and b) applicability of MCPs in a diverse array of applications including gas and liquid sorption<sup>33-36</sup> and separation,<sup>37</sup> sensing,<sup>38</sup> non-linear optics,<sup>39</sup> and heterogeneous catalysis.<sup>40</sup>

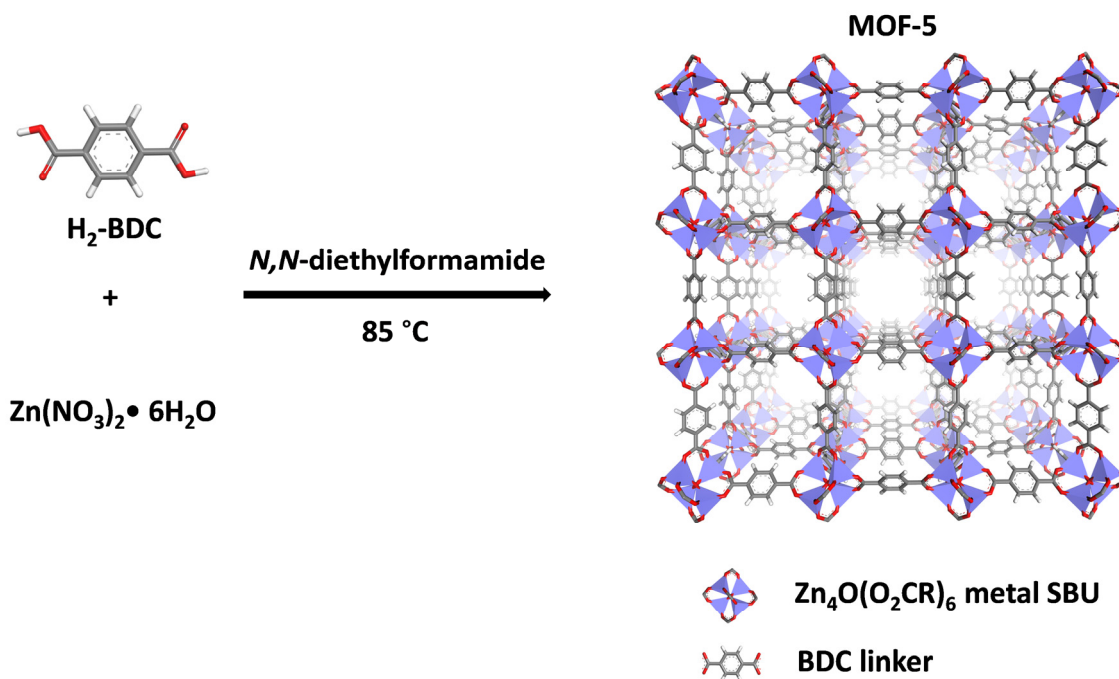


Figure 1. 2. Synthesis scheme of MOF-5 and structure of MOF-5 constructed from  $Zn_4O(O_2CR)_6$  and BDC linker.

### 1.3 Synthetic Strategies for Production of MCPs

#### 1.3.1 Coordination Polymerization

A vast majority of MCPs are synthesized from a single high symmetry linker coordinated to one type metal ion or cluster. MOF-5<sup>28</sup> and HKUST-1<sup>29</sup> are prototypical examples of such coordination polymers. MOF-5, a cubic MCP with 1.3 nm pore diameter, is synthesized from 1,4-benzenedicarboxylic acid (H<sub>2</sub>-BDC) and Zn(II) dissolved in *N,N*-diethylformamide followed by heating (Figure 1.2). MOF-5 is comprised of  $Zn_4O(O_2CR)_6$  metal cluster/ secondary building units (SBU) linked by BDC leading to a porous framework possessing a Brunauer–Emmett–Teller (BET) surface area of  $\sim 3800\text{ m}^2/\text{g}$  and a free volume of 77%. On the other hand, HKUST-

1 is an outcome of coordination polymerization of 1,3,5-benzenetricarboxylic acid (H<sub>3</sub>-BTC) and Cu(II) metal ion under solvothermal conditions. HKUST-1 is composed of the Cu<sub>2</sub>(O<sub>2</sub>CR)<sub>4</sub> metal SBU connected by BTC linkers. It possesses a cage structure with two distinct pores of 1.1 nm and 0.6 nm diameters. The BET surface area of HKUST-1 is ~ 1900 m<sup>2</sup>/g and the free pore volume is 69.5%. An attractive feature of this type coordination polymer is the ease with which the structure can be tuned. For example, lengthening the span between coordinating groups on a linker can lead to a series of isorecticular<sup>41</sup> (having same network topology) MCPs where the pore size of the resultant coordination polymer is directly proportional to the linker length.

Though the one linker and one metal strategy experienced an unparalleled growth, there are several drawbacks with this approach. Extending the linker by introducing spacer groups, a theoretically viable<sup>42</sup> means to produce coordination polymers with increased surface area and porosity, often is synthetically complex and drastically increases the costs of MCPs.<sup>43</sup> In this context, it must be noted that in order to compete with traditional sorbents such as activated carbons and zeolites, the cost of MCP synthesis must be substantially reduced. Moreover, the linker extensions designed to form structures with high accessible surface areas often promote interpenetration<sup>41, 44</sup> of two or more frameworks which ultimately reduces the porosity and surface area<sup>45</sup> of the material limiting their applications. Interpenetration<sup>46</sup> (Figure 1.3) is a physical entanglement of two or more frameworks where one framework intergrows into the void space of other. Empirically it has been observed that the high symmetry linkers often lead to production of frameworks with high symmetry substructures which are susceptible to interpenetration. For an example, 95% of MCPs derived from octahedral metal nodes with one kind of edge have been shown to favor *pcu* (primitive cubic) net<sup>47</sup> and readily interpenetrate. This phenomenon is also notable from the standpoint of lack of topological diversity. The



Reticular Chemistry Structure Resource (RCSR)<sup>48</sup>, a database of crystal nets, reveals a total of 11 nets possible for octahedral nodes with one kind of edge; however the majority of MCPs adopts the *pcu* topology.

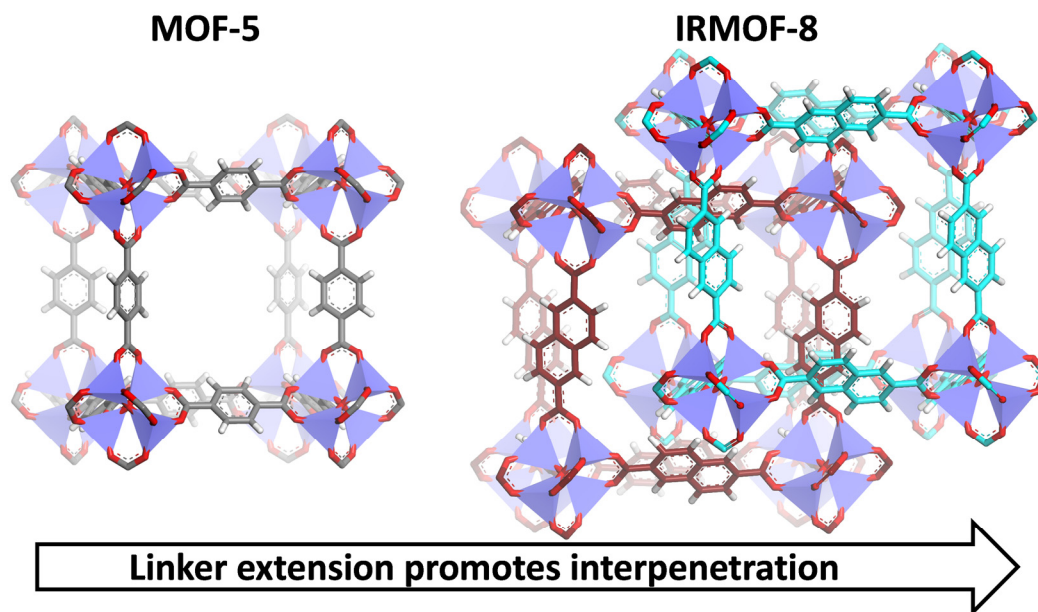


Figure 1. 3. Linker extension from BDC to 2,6-naphthalenedicarboxylate (NDC) promotes twofold interpenetration of *pcu* frameworks.

### 1.3.2 Coordination Copolymerization

In light of the limitations of MCPs derived from a single linker and a single metal and in search for structurally diverse and economically viable MCPs, researchers have developed a different strategy for production of MCPs: coordination copolymerization.<sup>49-51</sup> This approach involves employing more than one linker with a metal to give rise to a porous framework. Combining two linkers with a metal enables access to structural features and physical properties in the resultant materials which are otherwise unavailable from the pure linkers. Two linkers may possess the same or different coordinating functionalities and/or topologies. In 1999,<sup>49</sup> two linkers with different coordinating functionalities, carboxylate and neutral nitrogen based group,

were exploited to make a porous pillared-layer MCP  $[\text{Cu}_2(\text{pzdc})_2(\text{L})]_n$  (pzdc=pyrazine-2,3-dicarboxylate, L=neutral nitrogen based pillar linker such as pyrazine and 4,4'-bipyridine) (Figure 1.4). A few years later in 2004,<sup>52</sup> Kim and co-workers incorporated a mixture of BDC and 1,4-diazabicyclo[2.2.2]octane (DABCO) into another pillared-layer DMOF  $[\text{Zn}_2(\text{BDC})_2(\text{DABCO})]_n$  framework (Figure 1.5). Notably, DMOF is one of first examples of showing guest dependent dynamic behavior. The framework displayed a “breathing” phenomenon upon removal and re-addition of the guest molecules. The guest-free framework also set a record of the highest hydrogen uptake<sup>33</sup> at that time.

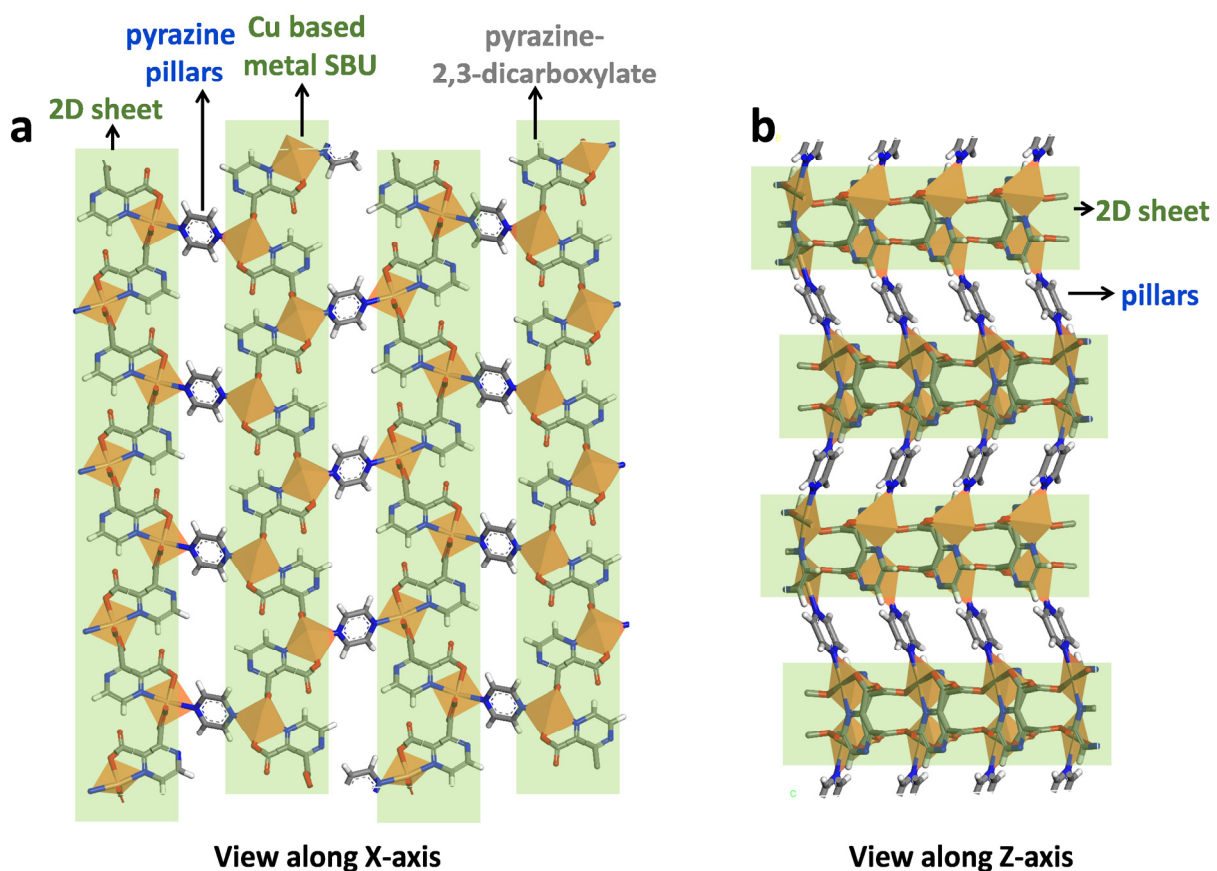


Figure 1. 4. Structure of pillared-layer MCP  $[\text{Cu}_2(\text{pzdc})_2(\text{L})]_n$  viewed along different axes.

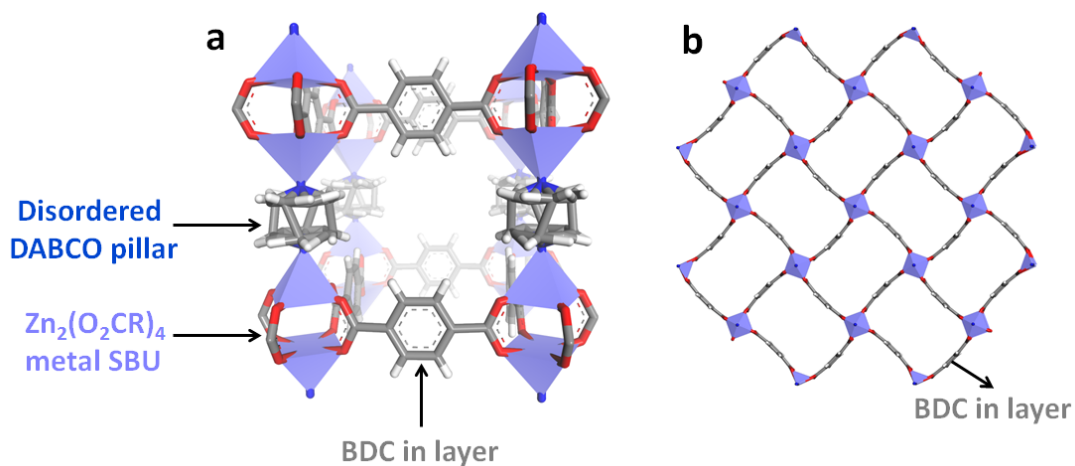


Figure 1. 5. a) Pillared layer structure and b) layer arrangement of DMOF  $[\text{Zn}_2(\text{BDC})_2(\text{DABCO})]_n$ .

Employing two linkers of identical coordinating functionality to generate a MCP appeared in 2008.<sup>50</sup> In this work, Matzger and coworkers<sup>50</sup> synthesized a porous coordination copolymer comprised of two organic linkers of different topologies yet the same carboxylate coordinating functionality, ditopic  $\text{H}_2$ -BDC and tritopic 1,3,5-tris(4-carboxyphenyl)benzene ( $\text{H}_3$ -BTB). Solvothermal reaction of  $\text{H}_2$ -BDC with  $\text{Zn}(\text{II})$  yields MOF-5,<sup>28</sup> a cubic MCP with *pcu* net whereas combination of  $\text{H}_3$ -BTB with  $\text{Zn}(\text{II})$  affords MOF-177,<sup>31</sup> a highly porous MCP having *qom* net topology. Mixing  $\text{H}_2$ -BDC with  $\text{H}_3$ -BTB in the presence of  $\text{Zn}(\text{II})$  leads to production of a completely new structure UMCM-1<sup>50</sup> possessing pore characteristics distinct than those of MOF-5 and MOF-177. Single crystal X-ray diffraction study revealed the presence of (Figure 1.8) central mesoporous hexagonal channels of 3.1 nm dimension surrounded by 1.4 nm microporous cages in UMCM-1, the features not available in the MCPs derived from pure linkers. Notably, formation of UMCM-1, dependent on synthetic feed ratio of  $\text{H}_2$ -BDC and  $\text{H}_3$ -BTB, occurred exclusively at ratios between 3:2 and 1:1. Outside of this range produced MOF-5 (with<sup>53</sup> or without defects), MOF-177, or physical mixtures of two phases. Applying

coordination copolymerization of two linkers with identical coordinating functionality in a combinatorial fashion allowed production of many high-performance MCPs<sup>43, 54</sup> with unprecedented network topologies enabled by the vast supply of commercially available and/or readily accessible organic linkers. Yaghi and co-workers<sup>55</sup> demonstrated the power of this approach by preparing MOF-210, a MCP derived from two carboxylate linkers, 1,3,5-tris(4-carboxyphenyl)triethynylbenzene (H<sub>3</sub>-BTE) prepared by one-step Sonogashira coupling and commercially available 4,4'-biphenyldicarboxylic acid (H<sub>2</sub>-BPDC), in presence of Zn(II). BET surface area of MOF-210 is as high as 6240 m<sup>2</sup>/g placing it amongst the highest surface area porous solids. This fact is even more striking if this value is compared to that of NU-100<sup>56</sup> (6143 m<sup>2</sup>/g), a MCP constructed from a single linker prepared by seven linear and ten total steps of a convergent synthesis and Cu(II).

Matzger and coworkers also studied the copolymerization of two carboxylate linkers of identical topology in presence of Zn(II). Mixing two carboxylate linkers having the same length yet decorated with different non-coordinating functionalities achieved random copolymers<sup>57, 58</sup> or core-shell architecture via controlling the order of precursors' addition (Figure 1.6).<sup>58</sup> Extending this random copolymerization method Yaghi group prepared eighteen multivariate<sup>55</sup> MOF-5 derivatives using nine differentially functionalized BDC linker. Nine of these MCPs were comprised of binary mixtures of linkers whereas the other nine were ternary or higher order. On the other hand, mixing two linkers of differing lengths did not lead to random copolymerization, rather enabled access to new structures endowed with unique structural features. For example, combination of H<sub>2</sub>-NDC, the organic linking unit of interpenetrated IRMOF-8,<sup>41</sup> and H<sub>2</sub>-BPDC, the linker in interpenetrated IRMOF-10,<sup>41</sup> in presence of Zn(II) creates a novel MCP, UMCM-9.<sup>43</sup> UMCM-9 is non-interpenetrated and possesses an ultrahigh surface area of ~5300 m<sup>2</sup>/g.<sup>43, 59</sup>

this surface area is particularly impressive given the fact that the linkers are commercially available.

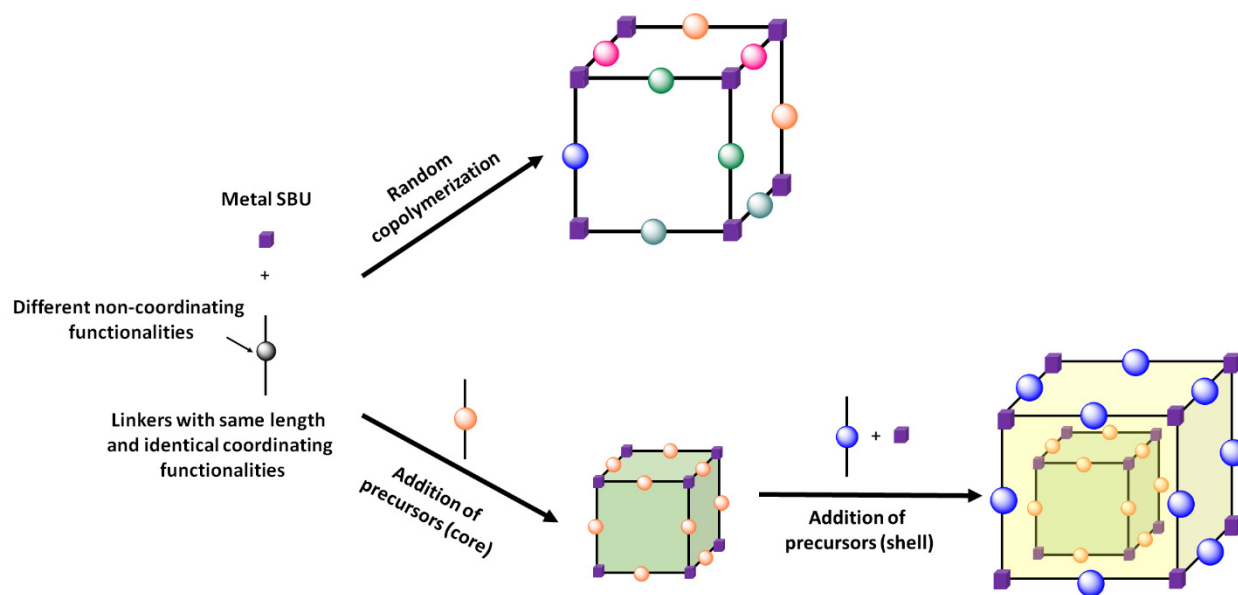


Figure 1. 6. Schematic showing coordination copolymerization of multiple linkers of same length and coordinating functionalities, however decorated with different non-coordinating functional groups. The first illustration is for random copolymerization and second one shows formation of a core-shell architecture via controlling the order of precursors' addition.

Despite the popularity of the two linkers and one metal strategy there exist a few disadvantages such as difficulties in rational design of frameworks and obtaining phase pure materials. The lack of predictability of network topology is considered the prime drawback of this strategy. The linker feed ratio and relative linker length strongly influence the outcome of coordination copolymerization resulting in a reduced predictability over network topology. The key reasons behind this dependence on feed ratio and relative linker length is diversity in possible linker arrangements around a metal SBU and thermodynamic factors influencing the assembly processes. Although a study<sup>50</sup> relating the statistics of plausible linker dispositions around a  $Zn_4O(O_2CR)_6$  SBU and the molar feed ratio of linkers has been performed to substantiate the formation of UMCM-1, this kind of correlation is not universally effective. On the other hand, the relative linker length<sup>60</sup> provides a guideline if coordination copolymerization is feasible or

not at a given linker combination; this means coordination copolymerization does not occur beyond a certain threshold value of linker length ratio. However, such geometric consideration is only applicable in some specific cases where two linkers are di- and tritopic. Moreover, this

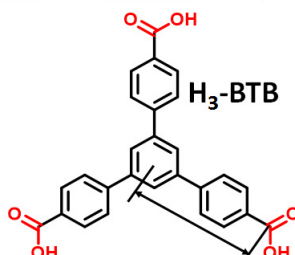
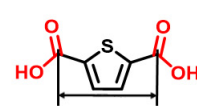
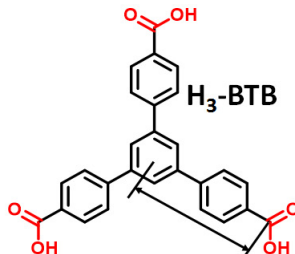
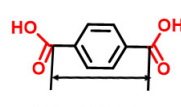
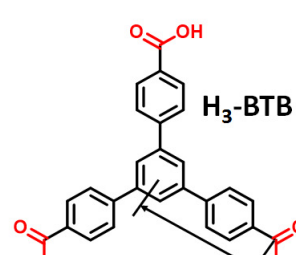
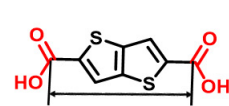
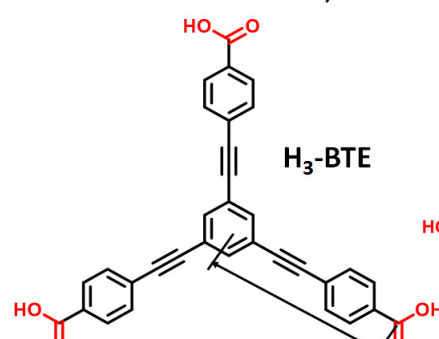
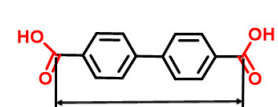
Tritopic linker	Ditopic linker	$l_{\text{ditopic}}/l_{\text{tritopic}}$	Resultant MCPs
 <p><b>H<sub>3</sub>-BTB</b></p>	 <p><b>H<sub>2</sub>-TDC</b></p>	0.73	UMCM-3
 <p><b>H<sub>3</sub>-BTB</b></p>	 <p><b>H<sub>2</sub>-BDC</b></p>	0.80	UMCM-1
 <p><b>H<sub>3</sub>-BTB</b></p>	 <p><b>H<sub>2</sub>-T<sup>2</sup>DC</b></p>	1.02	UMCM-2
 <p><b>H<sub>3</sub>-BTE</b></p>	 <p><b>H<sub>2</sub>-BPDC</b></p>	0.96	MOF-210

Figure 1. 7. Small variations of relative linker length of UMCM-1 give rise to completely new frameworks of distinct topologies.<sup>54, 60</sup>

parameter does not shed light on the final net topology frustrating rational design. As an example one rational pathway to systematically tune the structure of UMCM-1, i.e. varying the pore dimension while maintaining the overall net topology, can be replacement one or both linkers with a topologically identical yet different length ones, an effective strategy<sup>41</sup> exercised in coordination polymerization (Figure 1.7). UMCM-1 has a relative linker length ( $l_{\text{ditopic}}/l_{\text{tritopic}}$ ) of 0.80. Matzger and coworkers<sup>61</sup> combined thieno[3,2-b]thiophene-2,5-dicarboxylic acid ( $\text{H}_2\text{-T}^2\text{DC}$ ), a topologically identical yet longer linker than  $\text{H}_2\text{-BDC}$ , and  $\text{H}_3\text{-BTB}$  ( $l_{\text{ditopic}}/l_{\text{tritopic}} = 1.02$ ) in the presence of  $\text{Zn}(\text{II})$ . The solvothermal reaction of these components affords UMCM-2. The structure of UMCM-2 was revealed to be drastically different than UMCM-1 rather than being an extended UMCM-1 (Figure 1.8). Furthermore, Yaghi and coworkers mixed  $\text{H}_3\text{-BTE}$  and  $\text{H}_2\text{-BPDC}$  ( $l_{\text{ditopic}}/l_{\text{tritopic}} = 0.96$ ), extended analogues of  $\text{H}_3\text{-BTB}$  and  $\text{H}_2\text{-BDC}$

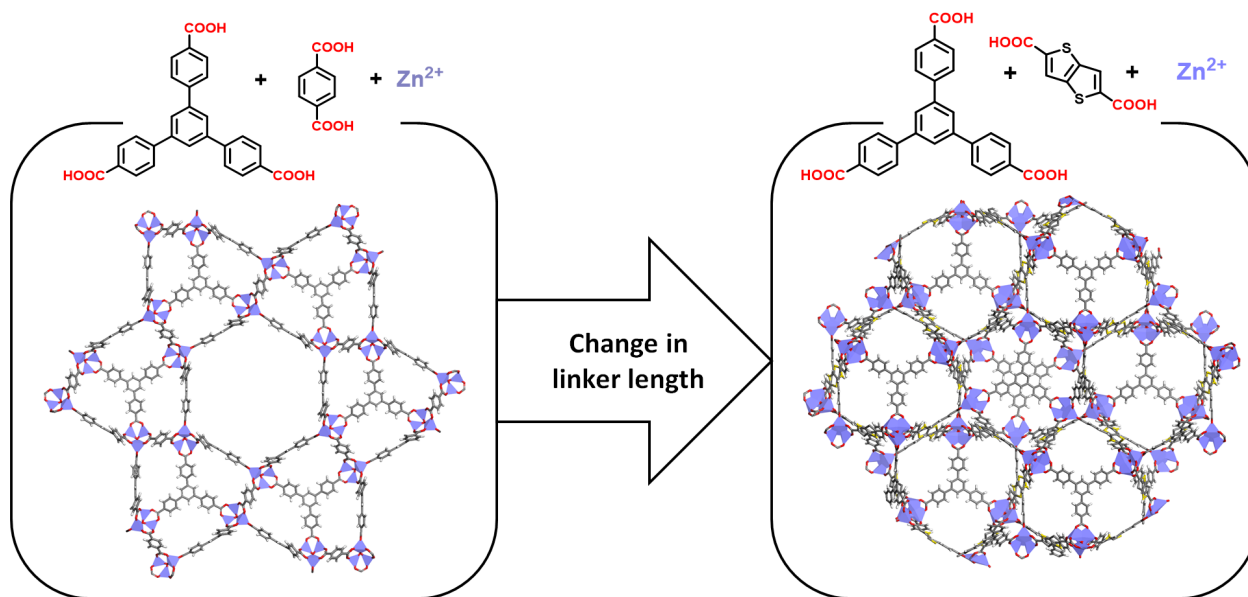


Figure 1. 8. An increase in linker length from BDC in UMCM-1 to  $\text{T}^2\text{DC}$  results into formation of a completely new structure UMCM-2.

respectively, in presence of  $\text{Zn}(\text{II})$  to produce MOF-210, structurally not similar to UMCM-1. To summarize, subtle variations of relative linker lengths of mixtures of di- and tritopic carboxylate

linkers dramatically affect the final topologies complicating the design.<sup>60, 62</sup> With regard to the phase purity of coordination polymers, it should be noted that coordination copolymerization involves the possibility of formation of multiple phases. In addition to mixed linker phases, MCP resulting from pure linker can also form. This sometimes can introduce laborious synthetic investigations and complications in characterization.

## **1.4 Organization of Thesis**

This thesis focuses on multicomponent approaches for the synthesis of microporous coordination polymers through linker and network design in order to generate structurally diverse porous materials.

### **1.4.1 Coordination Copolymerization of Three Carboxylate Linkers into a Pillared-layer Framework<sup>63</sup>**

Incorporation of three distinct linkers with identical carboxylate functionality into a pillared-layer MCP is described in this chapter 2. Traditional pillared-layer MCPs generally arise from coordination copolymerization of two linkers possessing different coordination functionalities in the presence of a metal. For an example, DMOF<sup>52</sup>  $[\text{Zn}_2(\text{BDC})_2(\text{DABCO})]_n$ , a prototypical pillared-layer MCP (Figure 1.5), is composed of dinuclear  $\text{Zn}_2(\text{O}_2\text{CR})_4$  paddlewheel metal SBUs bridged by BDC linker to generate 2D layers of  $\text{Zn}_2(\text{BDC})_2$  which are connected in the third dimension by 1,4-diazabicyclo[2.2.2]octane (DABCO) pillar linkers. The pillared-layer structure based on a carboxylate linker and a neutral nitrogen based pillar has been proven a reliable motif for the construction of porous frameworks with controllable pore sizes.<sup>64</sup> Simple length modification of a pillar has been shown to modulate the pore structures of MCPs in a systematic way.<sup>64</sup> However, a majority of the pillared-layer MCPs suffer from lack of framework



stability and permanent porosity which may be attributed to the lack of robustness of the metal 2

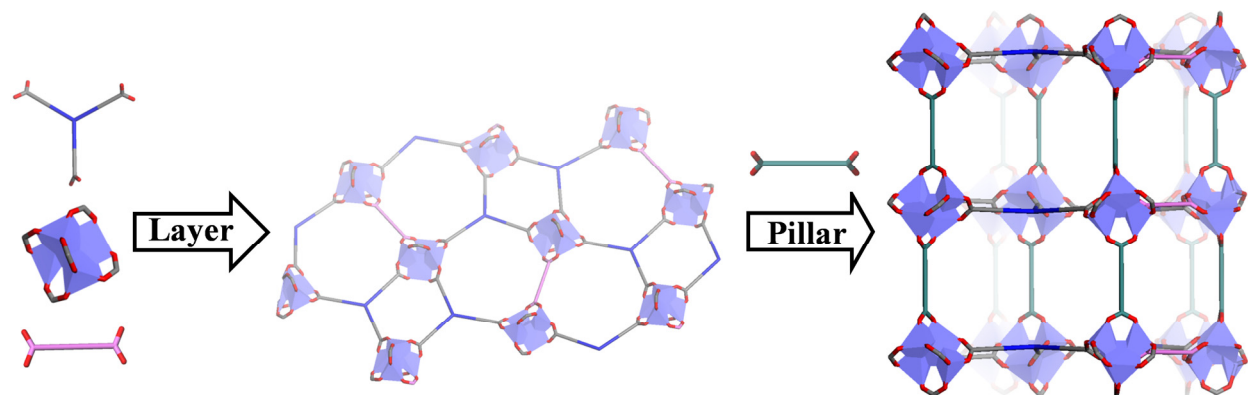


Figure 1. 9. Coordination terpolymerization of three carboxylate linkers (two involved in layer formation and one serving as pillar) into a pillared-layer framework.

SBU and the relatively weak coordinate covalent bonds between the metal ion and the neutral nitrogen based pillar linker.<sup>65</sup> Moreover, expanding the linker length often leads to n-fold ( $n \geq 2$ ) interpenetration in final structures.<sup>66</sup> To overcome these challenges, we have developed a coordination terpolymerization strategy (Figure 1.9). This approach enables formation of MCPs based on a configurationally robust SBU and anionic carboxylate linkers to impart a strong bonding between metal and pillar linker yielding a rigid framework. The employment of three carboxylate linkers into a framework also allows selective replacement of one pillar linker to another while keeping the layer arrangement unperturbed; this tunability resulted in a series of pillared-layer MCPs, UMCM-4, -10, -11, and -12, with variable pillars and an identical layer. Notably, lack of predictability of network topology upon variation of linker length, generally encountered in coordination copolymerization of two carboxylate linkers, was not observed in this work by judicious selection of the net. Moreover, the pillar linker extension from UMCM-4 to UMCM-12 occurs in absence of interpenetration resulting in high surface area materials. The pore size modulation by this uniaxial expansion on the pillar side also showed a great impact on molecular sieving of large organic molecules.

### 1.4.2 A Non-regular Layer Arrangement of a Pillared-layer Coordination Polymers: Avoiding Interpenetration via Symmetry Breaking at Nodes<sup>67</sup>

The coordination terpolymerization strategy described in chapter 2 is now exploited to alter the connectivity within the layer arrangement of a pillared-layer MCP. In this chapter 3 coordination copolymerization of three linkers, two carboxylate linkers and 4,4'-bipyridine, is utilized to form a non-regular layer arrangement and thwart the interpenetration of frameworks

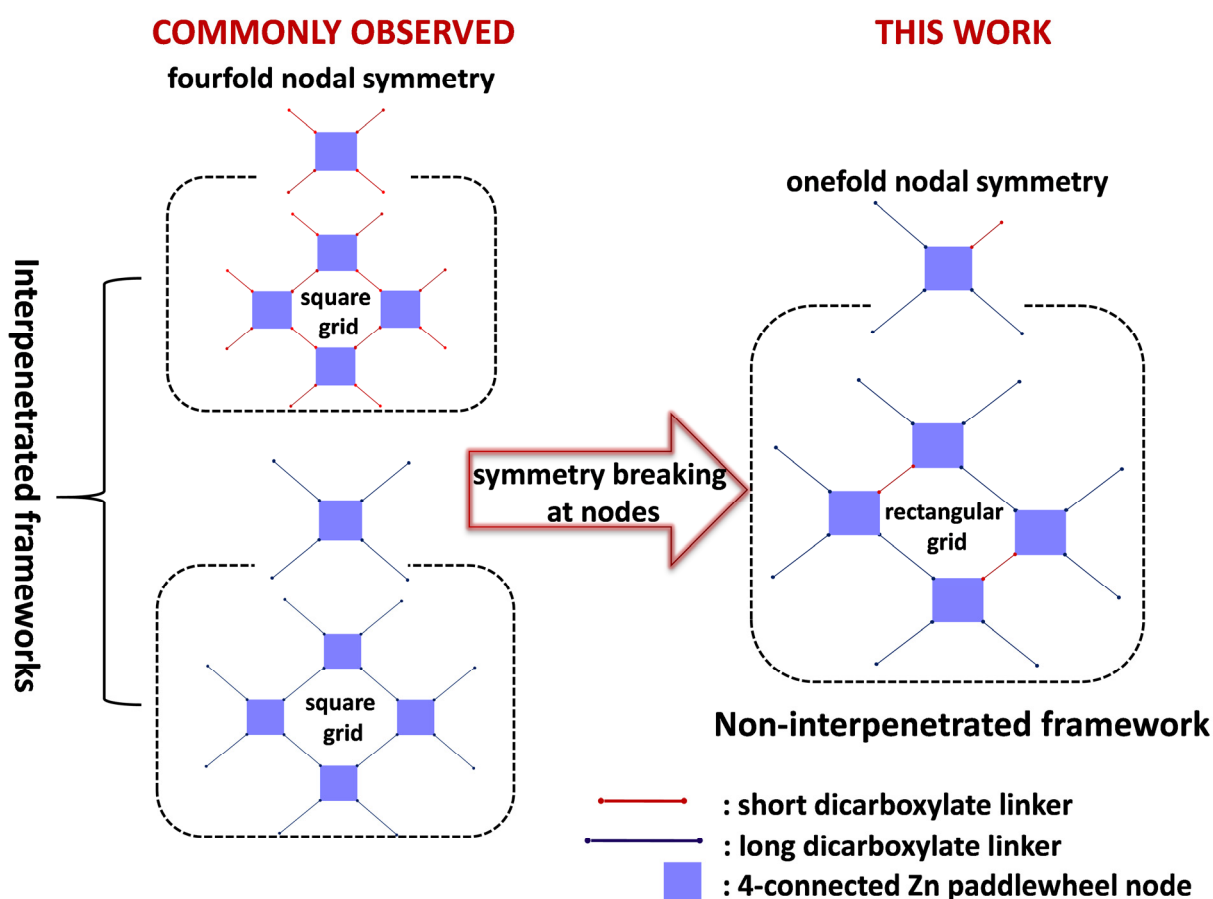


Figure 1. 10. Schematic comparing commonly observed layer arrangement stemming from a single dicarboxylate linker and the layer arrangement originated from combination of linkers around the 4-connected metal nodes.

(Figure 1.10). Varying the dimension of the 2D square grid of DMOF-like pillared-layer MCPs with alternative dicarboxylates to is very common in the literature.<sup>68</sup> However, tuning the geometry of the 2D grid from square to rectangular or else is without precedent. Furthermore, extension of the carboxylate linker in the layer often promotes the network interpenetration.<sup>52, 68</sup> In this chapter we study the result of employing two dicarboxylate linkers of differing lengths with 4,4'-bipyridine pillar in the presence of Zn(II) (Figure 1.10). Combination of these components generates UMCM-15, a MCP possessing a rectangular layer structure. In UMCM-15, the commonly observed fourfold symmetry at the metal SBU nodes is broken to onefold. This reduction of nodal symmetry, which originates from the unique arrangement of two dicarboxylate linkers around the metal cluster, suppresses the interpenetration of networks in UMCM-15. Moreover, using mixtures of commercially available linkers of differing lengths as a means to produce porous materials with non-regular structure and reduced interpenetration demonstrates a striking potential of generating a rich landscape of structurally diverse MCPs from simple feedstocks.<sup>43</sup>

### **1.4.3 Porous Solids Arising from Synergistic and Competing Modes of Assembly: Combining Coordination Chemistry and Covalent Bond Formation<sup>69</sup>**

Design and synthesis of porous solids employing both coordination chemistry and covalent bond formation is described in this work. In chapter 2 and 3 the multicomponent approaches have been exploited only through coordination chemistry. In this chapter, the power of the multicomponent approach is realized through covalent bond formation in tandem with coordination chemistry (Figure 1.11). A linker was designed for this study based on a widely used linker H<sub>3</sub>-BTB<sup>31</sup> where the central benzene ring was modified with a second site of reactivity: a primary amino group. This functionality provides an opportunity for imine

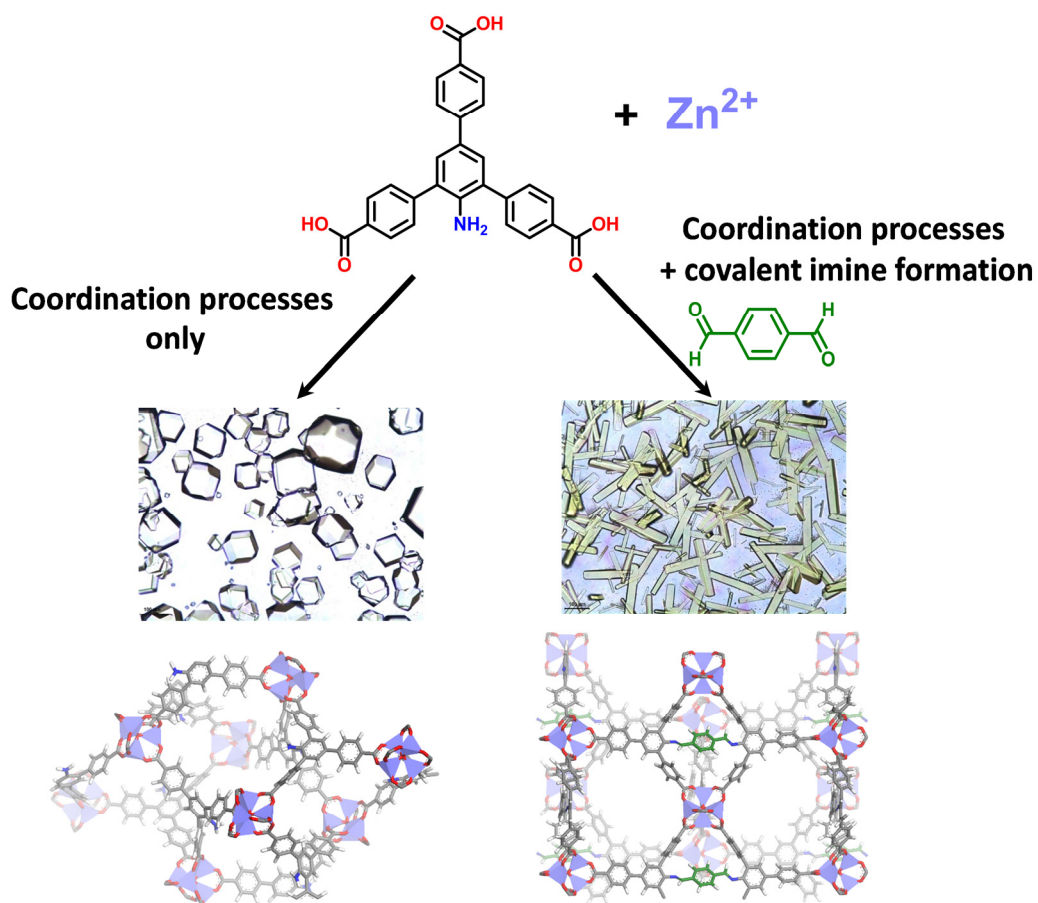


Figure 1. 11. Conceptual representation of different materials generated from coordination processes only (in absence of the dialdehyde) and combination of coordination processes and imine formation (in presence of the dialdehyde).

formation to take place upon reaction with a carbonyl group. In the absence of a carbonyl partner the solvothermal reaction of the linker and Zn(II) yields amino-MOF-177.<sup>31</sup> Upon addition of a dialdehyde component in the reaction mixture a new material, UMCM-306, is generated. The combination of two different chemistries, coordination and covalent imine bond formation, occurs in UMCM-306. This approach, in addition to being a compelling material discovery method, also offers a platform for developing fundamental understanding of factors influencing the competing modes of assembly. We also demonstrate that even temporary formation of

reversible connections between components can be leveraged to make new phases offering design routes to polymorphic frameworks.<sup>70</sup>

## 1.5. References

1. E. Robens, *Chem. Ing. Tech.*, 2010, **82**, 763-768.
2. M. Ahmedna, W. E. Marshall, A. A. Hussein, R. M. Rao and I. Goktepe, *Water Res.*, 2004, **38**, 1062-1068.
3. S. Sircar, T. C. Golden and M. B. Rao, *Carbon*, 1996, **34**, 1-12.
4. S. H. Joo, S. J. Choi, I. Oh, J. Kwak, Z. Liu, O. Terasaki and R. Ryoo, *Nature*, 2001, **412**, 169-172.
5. J. M. Planeix, N. Coustel, B. Coq, V. Brotons, P. S. Kumbhar, R. Dutartre, P. Geneste, P. Bernier and P. M. Ajayan, *J. Am. Chem. Soc.*, 1994, **116**, 7935-7936.
6. T. Voskuilen, T. Pourpoint and A. Dailly, *Adsorption*, 2012, **18**, 239-249.
7. A. C. Dillon, K. M. Jones, T. A. Bekkedahl, C. H. Kiang, D. S. Bethune and M. J. Heben, *Nature*, 1997, **386**, 377-379.
8. M. Suzuki, *Carbon*, 1994, **32**, 577-586.
9. Bandoz, T.J., M.J. Biggs, K.E. Gubbins, Y. Hattori, T. Iiyama, K. Kaneko, J. Pikunic, and K.T. Thomson, "Molecular Models of Porous Carbons," in *Chemistry and Physics of Carbons*, L.R. Radovic (Ed.), Vol. 28, Marcel Dekker, New York, 2003.
10. S. Kitagawa, R. Kitaura and S.-i. Noro, *Angew. Chem. Int. Ed.*, 2004, **43**, 2334-2375.
11. Z.-A. Qiao, Y. Wang, Y. Gao, H. Li, T. Dai, Y. Liu and Q. Huo, *Chem. Commun.*, 2010, **46**, 8812-8814.
12. A. F. Masters and T. Maschmeyer, *Microporous and Mesoporous Mater.*, 2011, **142**, 423-438.
13. Porous alumina and silica are two largely exploited commercial sorbents in separation industry. Their structures are similar to aluminosilicates except they possess only one metal, either Al or Si, bound with O atoms.
14. A. K. Cheetham, G. Férey and T. Loiseau, *Angew. Chem.*, 1999, **111**, 3466-3492.
15. H. de Sainte Claire Deville, *C. R. Hebd. Seances Acad. Sci.* 1862, **54**, 324.
16. J. D. Sherman, *Proc. Natl. Acad. Sci. USA*, 1999, **96**, 3471-3478.
17. G. R. Gavalas, in *Materials Science of Membranes for Gas and Vapor Separation*, John Wiley & Sons, Ltd, 2006, pp. 307-336.
18. C. J. Rhodes, *Sci. Prog.*, 2010, **93**, 223-284.
19. J. Weitkamp, *Solid State Ionics*, 2000, **131**, 175-188.
20. H. O. Pastore, S. Coluccia and L. Marchese, *Annu. Rev. Mater. Res.*, 2005, **35**, 351-395.
21. S. T. Wilson, B. M. Lok, C. A. Messina, T. R. Cannan and E. M. Flanigen, *J. Am. Chem. Soc.*, 1982, **104**, 1146-1147.
22. M. E. Davis, C. Saldarriaga, C. Montes, J. Garces and C. Crowdert, *Nature*, 1988, **331**, 698-699.
23. M. Hartmann and S. P. Elangovan, in *Advances in Nanoporous Materials*, ed. E. Stefan, Elsevier, 2010, vol. Volume 1, pp. 237-312.
24. B. F. Hoskins and R. Robson, *J. Am. Chem. Soc.*, 1989, **111**, 5962-5964.

25. Porous coordination polymers such as Prussian Blue and Hoffman clathrates had been known for decades prior to Robson's work. However, Robson first highlighted the "design" aspect for synthesis of a coordination polymer with a predictable net.
26. B. F. Abrahams, B. F. Hoskins and R. Robson, *J. Am. Chem. Soc.*, 1991, **113**, 3606-3607.
27. B. F. Hoskins and R. Robson, *J. Am. Chem. Soc.*, 1990, **112**, 1546-1554.
28. H. Li, M. Eddaoudi, M. O'Keeffe and O. M. Yaghi, *Nature*, 1999, **402**, 276-279.
29. S. S.-Y. Chui, S. M.-F. Lo, J. P. H. Charmant, A. G. Orpen and I. D. Williams, *Science*, 1999, **283**, 1148-1150.
30. MCP is termed using different names such as metal-organic framework (MOF), porous coordination polymer (PCP), and porous coordination network (PCN). Sometimes the name of the material originates from its birthplace such as Hong Kong University of Science and Technology (HKUST), University of Oslo (UIO), and University of Michigan Crystalline Material (UMCM).
31. H. K. Chae, D. Y. Siberio-Perez, J. Kim, Y. Go, M. Eddaoudi, A. J. Matzger, M. O'Keeffe and O. M. Yaghi, *Nature*, 2004, **427**, 523-527.
32. O. M. Yaghi, M. O'Keeffe, N. W. Ockwig, H. K. Chae, M. Eddaoudi and J. Kim, *Nature*, 2003, **423**, 705-714.
33. M. P. Suh, H. J. Park, T. K. Prasad and D.-W. Lim, *Chem. Rev.*, 2012, **112**, 782-835.
34. K. Sumida, D. L. Rogow, J. A. Mason, T. M. McDonald, E. D. Bloch, Z. R. Herm, T.-H. Bae and J. R. Long, *Chem. Rev.*, 2012, **112**, 724-781.
35. R. B. Getman, Y.-S. Bae, C. E. Wilmer and R. Q. Snurr, *Chem. Rev.*, 2012, **112**, 703-723.
36. H. Wu, Q. Gong, D. H. Olson and J. Li, *Chem. Rev.*, 2012, **112**, 836-868.
37. J.-R. Li, J. Sculley and H.-C. Zhou, *Chem. Rev.*, 2012, **112**, 869-932.
38. L. E. Kreno, K. Leong, O. K. Farha, M. Allendorf, R. P. Van Duyne and J. T. Hupp, *Chem. Rev.*, 2012, **112**, 1105-1125.
39. C. Wang, T. Zhang and W. Lin, *Chem. Rev.*, 2012, **112**, 1084-1104.
40. M. Yoon, R. Srirambalaji and K. Kim, *Chem. Rev.*, 2012, **112**, 1196-1231.
41. M. Eddaoudi, J. Kim, N. Rosi, D. Vodak, J. Wachter, M. O'Keeffe and O. M. Yaghi, *Science*, 2002, **295**, 469-472.
42. J. K. Schnobrich, K. Koh, K. N. Sura and A. J. Matzger, *Langmuir*, 2010, **26**, 5808-5814.
43. K. Koh, J. D. Van Oosterhout, S. Roy, A. G. Wong-Foy and A. J. Matzger, *Chem. Sci.*, 2012, **3**, 2429-2432.
44. O. M. Yaghi, *Nat. Mater.*, 2007, **6**, 92-93.
45. J. Hafizovic, M. Bjørgen, U. Olsbye, P. D. C. Dietzel, S. Bordiga, C. Prestipino, C. Lamberti and K. P. Lillerud, *J. Am. Chem. Soc.*, 2007, **129**, 3612-3620.
46. X.-L. Wang, C. Qin, E.-B. Wang, Y.-G. Li, Z.-M. Su, L. Xu and L. Carlucci, *Angew. Chem. Int. Ed.*, 2005, **44**, 5824-5827.
47. N. W. Ockwig, O. Delgado-Friedrichs, M. O'Keeffe and O. M. Yaghi, *Acc. Chem. Res.*, 2005, **38**, 176-182.
48. M. O'Keeffe, M. A. Peskov, S. J. Ramsden and O. M. Yaghi, *Acc. Chem. Res.*, 2008, **41**, 1782-1789.
49. M. Kondo, T. Okubo, A. Asami, S.-i. Noro, T. Yoshitomi, S. Kitagawa, T. Ishii, H. Matsuzaka and K. Seki, *Angew. Chem. Int. Ed.*, 1999, **38**, 140-143.
50. K. Koh, A. G. Wong-Foy and A. J. Matzger, *Angew. Chem. Int. Ed.*, 2008, **47**, 677-680.
51. D. N. Bunck and W. R. Dichtel, *Chem. Eur. J.*, 2013, **19**, 818-827.
52. D. N. Dybtsev, H. Chun and K. Kim, *Angew. Chem. Int. Ed.*, 2004, **43**, 5033-5036.

53. T.-H. Park, A. J. Hickman, K. Koh, S. Martin, A. G. Wong-Foy, M. S. Sanford and A. J. Matzger, *J. Am. Chem. Soc.*, 2011, **133**, 20138-20141.
54. H. Furukawa, N. Ko, Y. B. Go, N. Aratani, S. B. Choi, E. Choi, A. Ö. Yazaydin, R. Q. Snurr, M. O’Keeffe, J. Kim and O. M. Yaghi, *Science*, 2010, **329**, 424-428.
55. H. Deng, C. J. Doonan, H. Furukawa, R. B. Ferreira, J. Towne, C. B. Knobler, B. Wang and O. M. Yaghi, *Science*, 2010, **327**, 846-850.
56. O. K. Farha, A. Özgür Yazaydin, I. Eryazici, C. D. Malliakas, B. G. Hauser, M. G. Kanatzidis, S. T. Nguyen, R. Q. Snurr and J. T. Hupp, *Nat. Chem.*, 2010, **2**, 944-948.
57. T.-H. Park, K. Koh, A. G. Wong-Foy and A. J. Matzger, *Cryst. Growth Des.*, 2011, **11**, 2059-2063.
58. K. Koh, A. G. Wong-Foy and A. J. Matzger, *Chem. Commun.*, 2009, 6162-6164.
59. B. Liu, A. G. Wong-Foy and A. J. Matzger, *Chem. Commun.*, 2013, **49**, 1419-1421.
60. K. Koh, A. G. Wong-Foy and A. J. Matzger, *J. Am. Chem. Soc.*, 2010, **132**, 15005-15010.
61. K. Koh, A. G. Wong-Foy and A. J. Matzger, *J. Am. Chem. Soc.*, 2009, **131**, 4184-4185.
62. W. Chen, J.-Y. Wang, C. Chen, Q. Yue, H.-M. Yuan, J.-S. Chen and S.-N. Wang, *Inorg. Chem.*, 2003, **42**, 944-946.
63. A. Dutta, A. G. Wong-Foy and A. J. Matzger, *Chem.Sci.*, 2014, **5**, 3729-3734.
64. O. J. Garcia-Ricard, J. C. Silva-Martinez and A. J. Hernandez-Maldonado, *Dalton Trans.*, 2012, **41**, 8922-8930.
65. J. Seo, C. Bonneau, R. Matsuda, M. Takata and S. Kitagawa, *J. Am. Chem. Soc.*, 2011, **133**, 9005-9013.
66. B. Chen, S. Ma, F. Zapata, F. R. Fronczek, E. B. Lobkovsky and H.-C. Zhou, *Inorg. Chem.*, 2007, **46**, 1233-1236.
67. A. Dutta, J. Ma, A. J. Matzger, *manuscript in preparation*.
68. H. Chun, D. N. Dybtsev, H. Kim and K. Kim, *Chem. Eur. J.*, 2005, **11**, 3521-3529.
69. A. Dutta, K. Koh, A. G. Wong-Foy and A. J. Matzger, *Angew. Chem. Int. Ed.*, 2015, **54**, 3983-3987.
70. S. R. Caskey, A. G. Wong-Foy and A. J. Matzger, *Inorg. Chem.*, 2008, **47**, 7751-7756.

## Chapter 2

# Coordination Copolymerization of Three Carboxylate Linkers into a Pillared-Layer Framework

Published: A. Dutta, A. G. Wong-Foy, A. J. Matzger, *Chem. Sci.*, 2014, **5**, 3729-3734.

### 2.1 Introduction

Pillared-layer materials have been studied for decades and find applications in ion exchange, cracking of hydrocarbons and a variety of other applications where tailored structure optimizes function.<sup>1</sup> Therefore it is not surprising that one of the earliest and most well-studied classes of microporous coordination polymers (MCPs) are those based on pillaring of 2D sheets.<sup>2</sup> Systematic modulation of pillared-layer structure can be achieved for MCPs containing metal paddle-wheels<sup>3</sup> as secondary building units (SBUs) such as DMOF<sup>4</sup> as well as in materials arising from single-metal SBUs such as the CPL series.<sup>5, 6</sup> The pillar linkers utilized in these examples<sup>2, 7</sup> are organic although a few notable exceptions employing anionic inorganic pillars have recently shown great promise for selective CO<sub>2</sub> separation.<sup>8-10</sup> In all known cases, different functionalities are used in the pillar than those used to construct the 2D layer. In particular, using diamine (e.g. tertiary, aromatic) pillars connecting sheets has proven to be a reliable and controllable route to form 3D networks with predictable topology. However, despite the successes of these pillared-layer MCPs, they have some key disadvantages with regard to producing highly porous and stable frameworks. First, pillared-layer materials based on



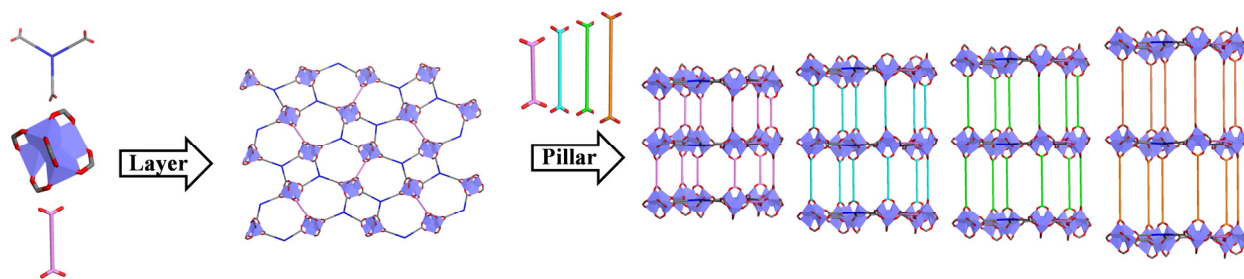


Figure 2. 1. Conceptual representation of the construction of different 3D networks from a 2D layer (composed of two linkers and SBU in all cases) connected *via* pillars (varying in pillar length).

metal paddle-wheel or pinwheel SBUs tend to be structurally dynamic and flexible upon removal and re-addition of molecular guests.<sup>11-14</sup> Second, they sometimes do not possess framework stability and permanent porosity<sup>7, 15</sup> which may be attributed to the “soft“ nature of the SBU<sup>16</sup> and the relatively weak coordinate covalent bonds between the metal ion and the neutral nitrogen based pillar linker. Third, pillared-layer MCPs often give rise to interpenetrated frameworks.<sup>17-19</sup> To overcome these challenges, we sought to develop MCPs based on a configurationally robust SBU and strong bonding between metal and pillar linker to yield a rigid framework. UMCM-4, a coordination copolymer recently developed,<sup>20</sup> is constructed from the  $Zn_4O(O_2CR)_6$  SBU and two topologically different carboxylate linkers and meets these criteria for framework stability. In UMCM-4, 2D layers are connected with di-anionic carboxylate linkers rather than neutral diamines. To systematically alter the structure of UMCM-4 we envisioned that the spacing modulation would involve a copolymerization of three distinct carboxylate linkers in presence of Zn(II) in order to create uniaxial lattice expansion (Figure 2.1). Here we present MCPs (UMCM-10, -11, and -12) incorporating three distinct linkers with identical coordinating functionality in the same coordination polymer. Additionally, as in case of UMCM-4, these MCPs have non-interpenetrated structures which can be attributed to the fact that their nets are not self-duals;<sup>21</sup> this behavior contrasts with the more common pillared-layer structures exhibiting n-fold interpenetration.<sup>17-19</sup> Except for the cases of certain privileged nets such as *rht*,<sup>22</sup> extension of

linkers while avoiding interpenetration<sup>23, 24</sup> is rare. Here we illustrate a series of coordination copolymers derived from three linkers that act as robust analogues of the neutral diamine pillar based materials.

## 2.2 Results and Discussion

UMCM-4  $[\text{Zn}_4\text{O}(\text{TPA})_1(\text{BDC})_{1.5}]_n$  has a non-interpenetrated pillared-layer structure.<sup>20</sup> The 2D layer is constructed from one type of SBU coordinated in the plane to three tritopic linkers, 4,4',4''-tricarboxylatetriphenylamine (TPA), and one ditopic linker, 1,4-benzenedicarboxylate (BDC). The pillar connecting the sheets in the third dimension is BDC. For uniaxial pore size extension to occur, introduction of a second ditopic pillar linker was envisioned to replace the axial BDC. In the case of prototypical paddle-wheel based MCPs, the pillar linkers possess coordinating functionalities distinct from that used for construction of the 2D layer. This orthogonality allows for changing the pillar without altering the 2D layer structure.<sup>2, 7</sup> By contrast, employing three linkers possessing the same coordinating functionality has a minimum of four plausible outcomes: a) the new ditopic linker may not be incorporated in the final structure resulting in UMCM-4, b) the linker may be inserted into the 2D layer, thus distorting the original layer structure, c) the linker may get incorporated in both 2D layer and pillar sites resulting in an unpredictable structure with expansion in multiple dimensions, and d) the linker may occupy solely the pillar position without altering the layer structure. Among all these cases, only the last enables systematic modulation of pore dimensionality (Figure 2.1).

Solvothermal reaction of a mixture of tritopic ( $\text{H}_3$ -TPA) and ditopic ( $\text{H}_2$ -BDC) linkers with the additional second ditopic linker 2,2',6,6'-tetramethylbiphenyl-4,4'-dicarboxylic acid ( $\text{H}_2$ -TMBPDC) in a 1:1:2 molar ratio in the presence of Zn(II) results in a new material incorporating all three linkers designated UMCM-10 (Figure 2.2). Similarly, UMCM-11 and

2-D layer	Tritopic linker				
	Ditopic linker				
Pillar	Ditopic linker				
	MCP	UMCM-4	UMCM-10	UMCM-11	UMCM-13

Figure 2. 2. Linker combinations yielding pillared layer MCPs with the  $Zn_4O(O_2CR)_6$  SBU

UMCM-12 were obtained by replacement of H<sub>2</sub>-TMBPDC with 4,4'-(ethyne-1,2-diyl) dibenzoic acid (H<sub>2</sub>-EDDB) or 2',3',5',6'-tertramethylterphenyl-4,4''-dicarboxylic acid (H<sub>2</sub>-TMTTPDC) as pillar linkers respectively (Figure 2.2) (Section 2.4.1). Methyl substitution on the linkers having more than one benzene rings: 1) greatly enhances linker solubility in the solvent of synthesis and 2) eliminates the use of other co-solvents in order to dissolve the non-methylated pillared linkers which can introduce phase changes. <sup>1</sup>H NMR spectroscopy experiments were performed on acid digests of activated UMCM-10, -11, and -12; three linkers were present in ratios consistent with formation of the desired pillared motif (Section 2.4.4). Utilization of non-alkylated ditopic linkers was also attempted and proved to be successful for biphenyl-4,4'-dicarboxylic acid. However, use of terphenyl-4,4''-dicarboxylic acid yielded UMCM-4 phase primarily due to the poor solubility of the linker in solvent of synthesis (Section 2.4.2). Powder X-ray diffraction patterns of UMCM-4, -10, -11, and -12 (Figure 2.3) show structural similarity among these

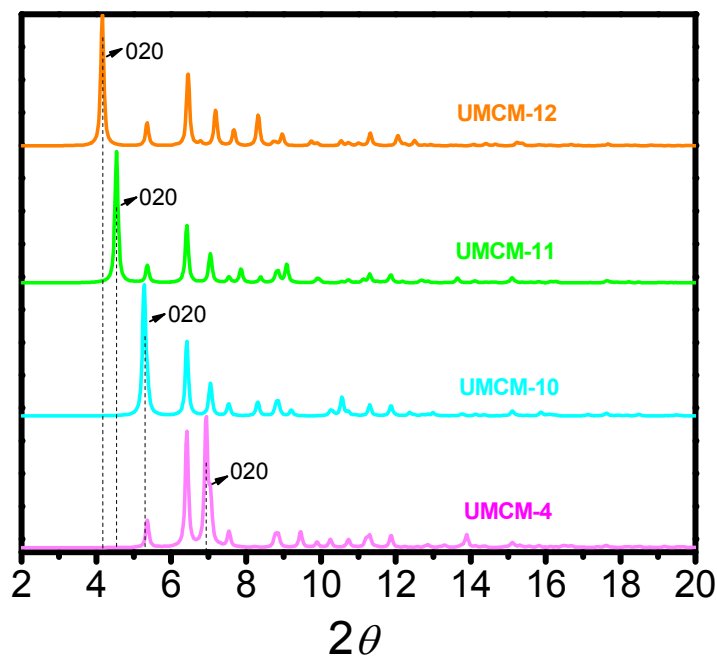


Figure 2. 3. PXRD patterns of MCPs. The (020) reflections correspond to half of the layer spacings.

MCPs which is consistent with maintenance of the 2D layer. Moreover, the (020) reflection corresponding to the periodicity introduced by the pillar shifts to lower  $2\theta$  with increasing pillar length. Unambiguous confirmation of the pillared-layer structure of UMCM-10 and -12 was obtained from single crystal X-ray diffraction (Section 2.4.3). Three tritopic (TPA) and one ditopic (BDC) linkers assemble around the octahedral SBU to generate a layer with two windows of dimensions:  $4.7 \times 7.7 \text{ \AA}^2$  and  $8.7 \times 9.4 \text{ \AA}^2$  (Figure 2.4e) as in the case of UMCM-4. The remaining two ditopic linkers are arranged *trans*- to each other serving as pillars between adjacent layers of spacing  $14.2 \text{ \AA}$  and  $19.2 \text{ \AA}$  in UMCM-10 and -12 respectively (Figure 2.4). Moreover, the structures are non-interpenetrated.<sup>25</sup> Several attempts to grow suitable single crystal of UMCM-11 were unsuccessful. However, a model was constructed computationally by BDC substitution at the pillar position of UMCM-4 with EDDB. The experimental powder patterns are in good agreement with one simulated from the model confirming the pillared-layer

structure of UMCM-11 (Section 2.4.2). This behavior of preserving topology can be contrasted with a recent report<sup>26</sup> that discloses the coordination copolymerization of three carboxylate linkers; addition of a third linker into the feed of UMCM-1,<sup>27</sup> a coordination copolymer derived from two carboxylate linkers, yields a totally new structure rather than an expanded version of UMCM-1.

The success of selective pillar substitution can be traced back to the stability of the 2D layer structure composed of TPA and BDC. Substitution of BDC with a longer ditopic linker would disrupt this layer structure; therefore substitution occurs selectively at the pillar position to avoid perturbing the layer arrangement. Such thermodynamic considerations in dictating the

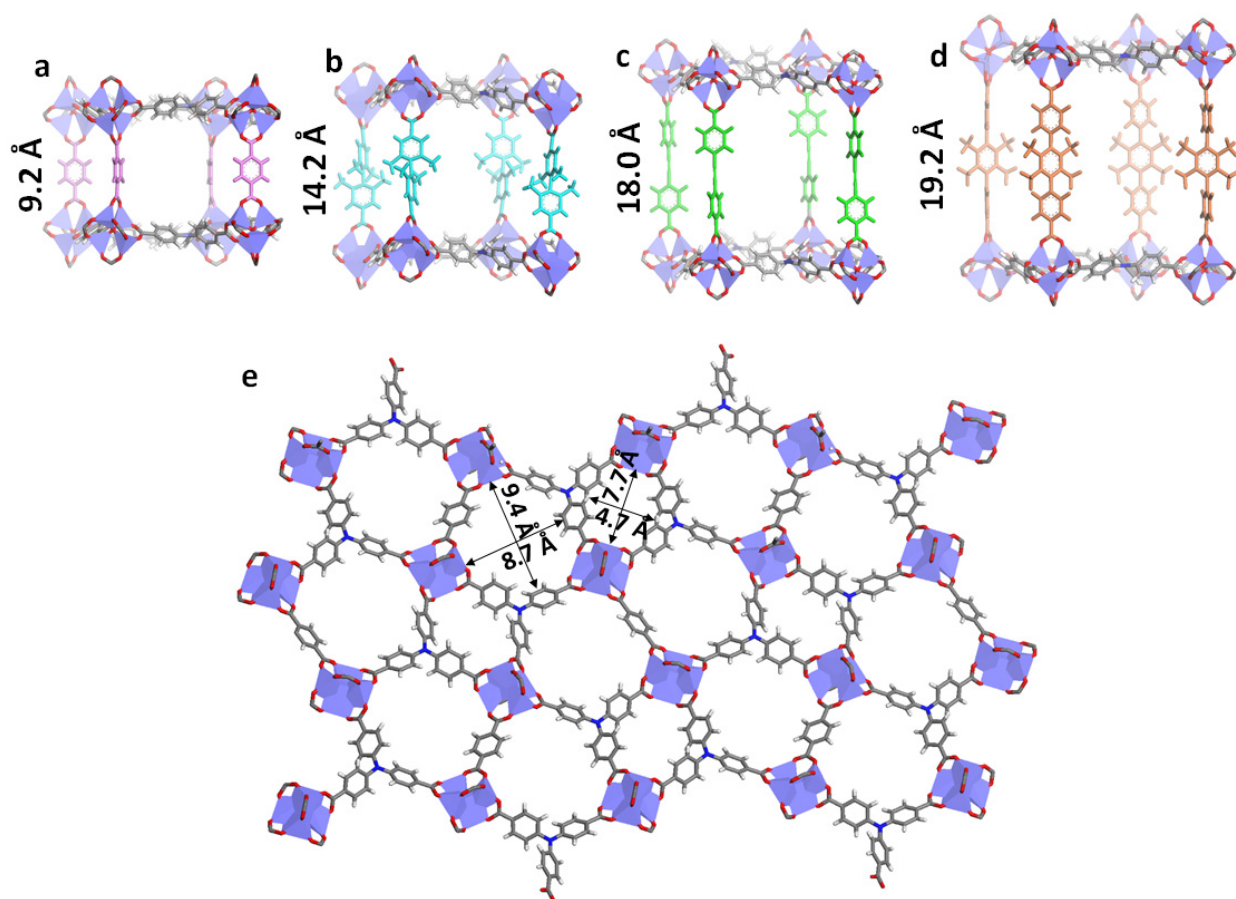


Figure 2. 4. Structures of (a) UMCM-4, (b) UMCM-10, (c) UMCM-11 (generated from model), and (d) UMCM-12. The 2D layer (e) is preserved in each structure and illustrated for UMCM-4. Different pore dimensions are measured with subtraction of the van der Waals radii of the atoms.

stability of coordination copolymers derived from two linkers has previously been invoked.<sup>20</sup> Occurrence of interpenetration within a series of MCPs upon linker extension can be tied to the tendency of materials to close pack. However, if suitable network topologies are chosen this can be avoided. In the case of UMCM-4, -10, -11, and -12, one framework cannot pass through the aperture of another framework without overlapping framework atoms; this indicates that these MCPs possess non self-dual nets.<sup>21</sup> In this context it should be noted that there is a dramatic structural difference between MCPs derived from coordination copolymerization of three linkers and MCPs constructed from pure linkers. For an example, reaction of Zn(II) with H<sub>3</sub>-TPA affords MOF-150 which occurs as a doubly-interpenetrated network<sup>28</sup> and H<sub>2</sub>-TMBPDC reacts in presence of Zn(II) to generate an interpenetrating pair of nets of Zn<sub>4</sub>O(TMBPDC)<sub>3</sub><sup>29</sup> whereas UMCM-10 possesses a non-interpenetrated structure. This finding illustrates the power of symmetry breaking<sup>30</sup> at the network nodes,<sup>20</sup> a common feature in MCPs produced by coordination copolymerization.

Given that the linker extension from UMCM-4 to UMCM-12 occurs in the absence of interpenetration, a significant and systematic increase of N<sub>2</sub> uptake and surface area is expected.<sup>31</sup> These MCPs exhibit high predicted<sup>32</sup> and experimental BET surface areas (Table 2.1) with a substantial increase in N<sub>2</sub> uptake from UMCM-4 to UMCM-12 (Figure 2.5a). The experimental surface area values (UMCM-4: 3632 m<sup>2</sup>/g, UMCM-10: 4001 m<sup>2</sup>/g, UMCM-12: 4849 m<sup>2</sup>/g) are much higher than pillared-layer materials present in the literature.<sup>33</sup> UMCM-4 and -10 show Type I isotherms confirming microporosity (Section 2.4.6) of these materials whereas the isotherm of UMCM-12 is not strictly Type I as it exhibits an extra feature near P/P<sub>0</sub> ~ 0.04 (Figure 2.5b). However, UMCM-11 undergoes a structural change upon activation as judged by PXRD before and after flowing supercritical CO<sub>2</sub> activation<sup>34</sup> (Figure 2.8); this leads

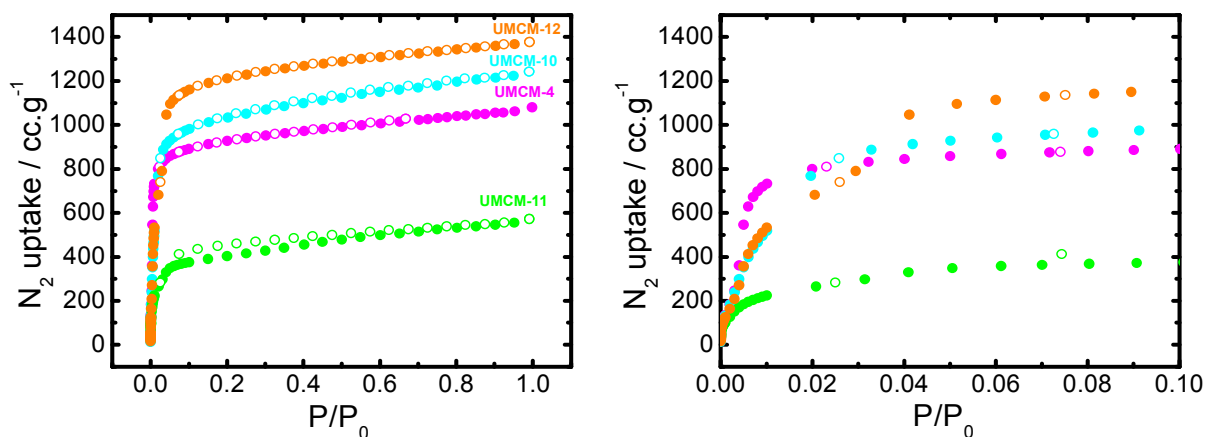


Figure 2. 5. a) Nitrogen sorption isotherms and b) sorption traces in the low pressure region for UMCM-4, -10, -11, and -12.

to BET surface areas ranging from 1100-1600 m<sup>2</sup>/g. We sought to understand the origin in difference in framework stability of these MCPs and envision that the structural instability can arise from the lack of rigidity of the linker connecting two nodes. The distortion of the pillar linker EDDB in UMCM-11 can be ascribed to the relatively high deformability of the triple bond.<sup>35</sup>

Based on high surface areas H<sub>2</sub> storage performance of these materials at high pressure and cryogenic temperature can be projected to approximately 4.8, 6.1, and 6.9 wt% of excess gravimetric H<sub>2</sub> uptake for UMCM-4, -10, and -12 respectively.<sup>36</sup> In this context it should be noted that excess gravimetric uptakes of H<sub>2</sub> of these materials are almost equal (~ 1.3 wt%) at 77K and 1 bar (Figure 2.22). This behavior can be explained by weakening of the interaction of guest molecules with the MCP framework with the expansion of pore dimension from UMCM-4 to UMCM-12 countered by increment of surface areas. This fact sets the expectation for UMCM-12 being the material with highest deliverable H<sub>2</sub> uptake in this series of MCPs and the hypothesis is currently being tested. Given the high porosity of these materials high CO<sub>2</sub> uptake is expected. Indeed CO<sub>2</sub> sorption isotherm of UMCM-4 at 195 K exhibits high CO<sub>2</sub> uptake at 1 bar (767 cc/g) (Figure 2.23). However, the uptakes of UMCM-10 (182 cc/g) and UMCM-12

(560 cc/g) are lower than that of UMCM-4. It is hypothesized that the structural integrity was compromised during CO<sub>2</sub> sorption experiment which was later confirmed by powder X-ray diffraction patterns as well as surface area measurements before and after CO<sub>2</sub> sorption. However, this behavior is not a common occurrence to our knowledge and specifically surprising in the light of the fact that the high surface areas of these materials were obtainable *via* flowing supercritical CO<sub>2</sub> activation.<sup>34</sup>

Environmental and thermal stabilities of MCPs are important issues for application of MCPs. Thus the stability of these materials were investigated at elevated temperatures as well as in humid air. Activated UMCM-4, -10, and -12 were heated at different temperatures ranging from 150 °C to 250 °C. The variable temperature powder X-ray diffraction patterns showed negligible or no change of peak positions and intensities at 200 °C in case of UMCM-10 and at 250 °C for other materials (Figures 2.24 - 2.26). Thermogravimetric analyses showed sharp loss of mass due to decomposition near 400 °C (Figures 2.15 – 2.17). The assessment of structural integrity of activated materials upon exposure to air at room temperature (23 °C, 12 hr, and 23% relative humidity) was done via powder X-ray diffraction. Again powder X-ray diffraction patterns of exposed materials showed no significant change of peak positions and intensities under these conditions (Figures 2.27 – 2.29).

Utilization of the uniaxial expansion strategy is anticipated to have a particular impact on the liquid phase separation of large molecules.<sup>37</sup> In order to test this notion in the context of molecular sieving, three polycyclic organic dyes with different kinetic diameters (indicated in parenthesis) were chosen: Nile red (8.6 Å), Reichardt's dye (14.2 Å), and Coomassie Brilliant Blue G (19.8 Å) (Figure 2.33). Difference in pore size of UMCM-4, -10, -11, and -12 due to uniaxial expansion yet maintenance of identical pore shape was expected to show significant



molecular sieving depending on kinetic diameter of these three dyes. Nile red, possessing the

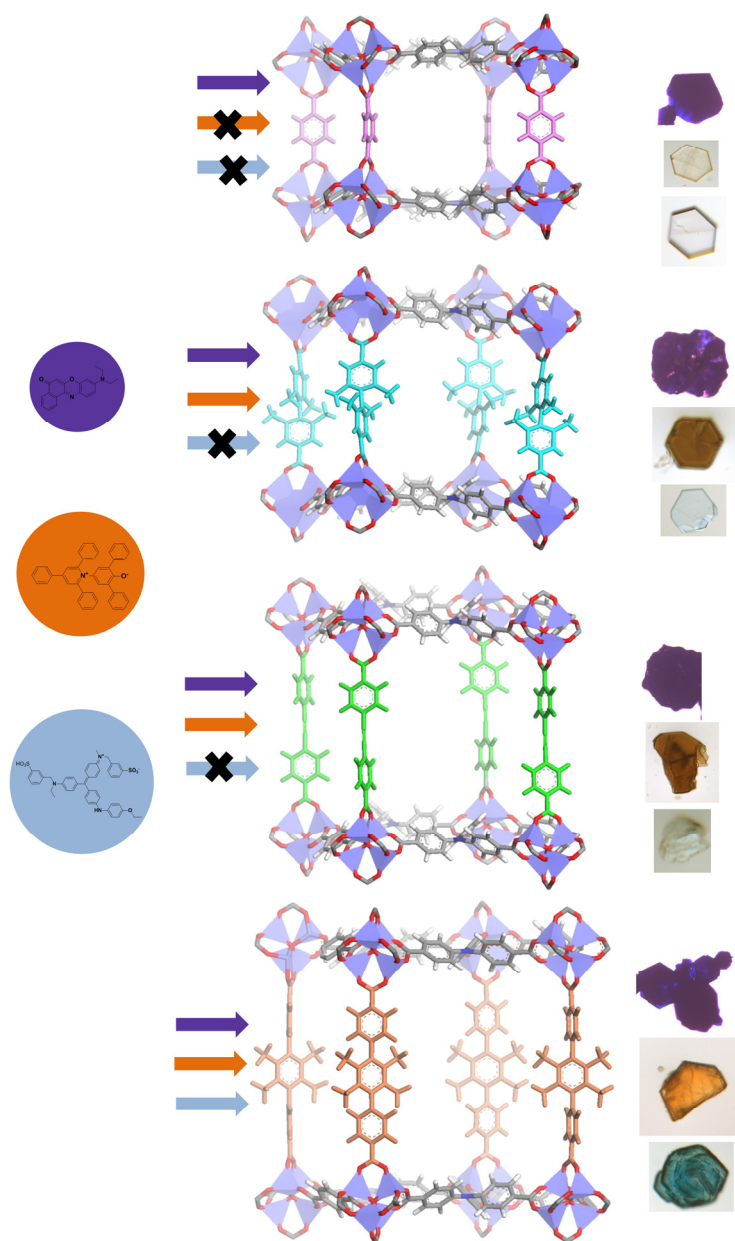


Figure 2. 6. Summary of size exclusion results for dye incorporation into UCMCM-4, -10, -11, and -12. Nile red, Reichardt's dye and Coomassie Brilliant Blue G are represented in violet, light brown and light blue spheres. The color of the shown sectioned crystals indicate success or failure of dye impregnation into the corresponding MCP crystals.

smallest kinetic diameter, can penetrate the pores and is absorbed in all MCPs. On contrary,

Reichardt's dye and Coomassie Brilliant Blue G, being bigger in size than Nile red, can only enter the pores which have comparable or larger dimensions than their kinetic diameters (Figure 2.6).

Even in the case of Nile red, which is able to penetrate all MCPs, the pore size influences the nature of inclusion. Nile red in UMCM-4 shows significant linear dichroism<sup>38, 39</sup> consistent with tight confinement of the planar dye (Figure 2.34). Nile red, being a planar dye, preferentially aligns in the anisotropic pores of UMCM-4 resulting in different absorption spectra as a function of the direction of linearly polarized light. By contrast, due to larger pore dimensions the orientation of Nile red molecules in UMCM-10 through -12 is largely random. Thus, negligible linear dichroism is observed.

## **2.3 Conclusions**

Coordination copolymerization of three linkers offers an attractive approach in the field of MCPs to produce stable pillared-layer structures. Distinct from other well-studied pillared-layer MCPs, UMCM-4, -10, -11, and -12 have all linkers possessing carboxylate functionalities and, in the cases of the largest three members of the series, arises from a combination of three linkers. The uniaxial expansion of MCPs, although extensively exploited in other pillared-layer materials, has not been observed in MCPs based on the ubiquitous  $Zn_4O(O_2CR)_6$  SBU. Moreover, this strategy leads to non-interpenetrated structures upon linker extension enabling molecular sieving of large molecules across the series of MCPs.

## **2.4 Experimental Section**

### **2.4.1 Synthesis of MCPs**

2,2',6,6'-tetramethylbiphenyl-4,4'-dicarboxylic acid (H<sub>2</sub>-TMBPDC),<sup>40</sup> 4,4'-(ethyne-1,2-diyl) dibenzoic acid (H<sub>2</sub>-EDDB),<sup>41</sup> 2,2',3',5',6'-tertramethylterphenyl-4,4''-dicarboxylic acid (H<sub>2</sub>-TMTPDC)<sup>42</sup> were synthesized following the reported methods.

A) Preparation of Zn<sub>4</sub>O(TPA)(BDC)<sub>1/2</sub>(TMBPDC): UMCM-10.

H<sub>2</sub>-BDC (5.48 mg, 0.0330 mmol), H<sub>2</sub>-TMBPDC (19.7 mg, 0.0667 mmol), H<sub>3</sub>-TPA (12.5 mg, 0.0330 mmol) and Zn(NO<sub>3</sub>)<sub>2</sub> · 6H<sub>2</sub>O (119 mg, 0.400 mmol) were dissolved in 5.0 mL of *N,N*-diethylformamide. The mixture was sonicated for 15 min and the solution was clarified by filtration through a glass wool plug. The reaction mixture was heated to 85 °C. After 2 days, crystals of a single phase were obtained. After cooling to room temperature, the product was isolated by decanting the mother liquor and washing with fresh DMF (3 × 15 mL). The yield of the reaction determined from the weight of the solvent-free material (17.3 mg) is 52.4% based on H<sub>3</sub>-TPA.

B) Preparation of Zn<sub>4</sub>O(TPA)(BDC)<sub>1/2</sub>(EDDB): UMCM-11.

H<sub>2</sub>-BDC (5.48 mg, 0.0330 mmol), H<sub>2</sub>-EDDB (17.6 mg, 0.0667 mmol), H<sub>3</sub>-TPA (12.5 mg, 0.0330 mmol) and Zn(NO<sub>3</sub>)<sub>2</sub> · 6H<sub>2</sub>O (119 mg, 0.400 mmol) were dissolved in 5.0 mL of 1:1 (v/v) *N,N*-diethylformamide and *N*-methylpyrrolidinone. The mixture was sonicated for 15 min and the solution was clarified by filtration through a glass wool plug. The reaction mixture was heated to 85 °C. After 5 days, crystals of a single phase were obtained. After cooling to room temperature, the product was isolated by decanting the mother liquor and washing with fresh DMF (3 × 15 mL). The yield of the reaction determined from the weight of the solvent-free material (17.0 mg) is 51.6% based on H<sub>3</sub>-TPA.

C) Preparation of Zn<sub>4</sub>O(TPA)(BDC)<sub>1/2</sub>(TMTPDC): UMCM-12.

H<sub>2</sub>-BDC (6.72 mg, 0.0405 mmol), H<sub>2</sub>-TMTPDC (14.96 mg, 0.040 mmol), H<sub>3</sub>-TPA (7.57 mg, 0.0201 mmol) and Zn(NO<sub>3</sub>)<sub>2</sub> · 6H<sub>2</sub>O (89.2 mg, 0.300 mmol) were dissolved in 5.1 mL of *N,N*-diethylformamide. The mixture was sonicated for 40 min and the solution was clarified by filtration through a glass wool plug. The reaction mixture was heated to 85 °C. After 12 hours, crystals of a single phase were obtained. After cooling to room temperature, the product was isolated by decanting the mother liquor and washing with fresh DMF (3 × 15 mL). The yield of the reaction determined from the weight of the solvent-free material (10.0 mg) is 50.1% based on H<sub>3</sub>-TPA.

#### 2.4.2. PXRD Patterns of UMCM-10, -11, and -12

Samples for powder X-ray diffraction were soaked in mineral oil before collection of data. Data were collected on Rigaku R-Axis Spider diffractometer with an image plate detector and CuK $\alpha$  radiation operating in transmission mode. The powder samples were rotated on the goniometer in  $\phi$  and oscillated in  $\omega$  to minimize preferred orientation.

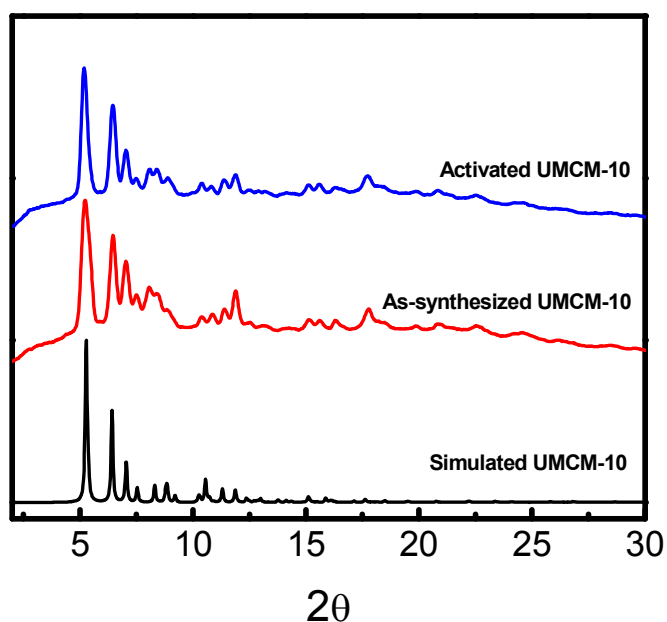


Figure 2. 7. Powder XRD patterns of UMCM-10 (black: simulated, red: as synthesized, blue: activated).

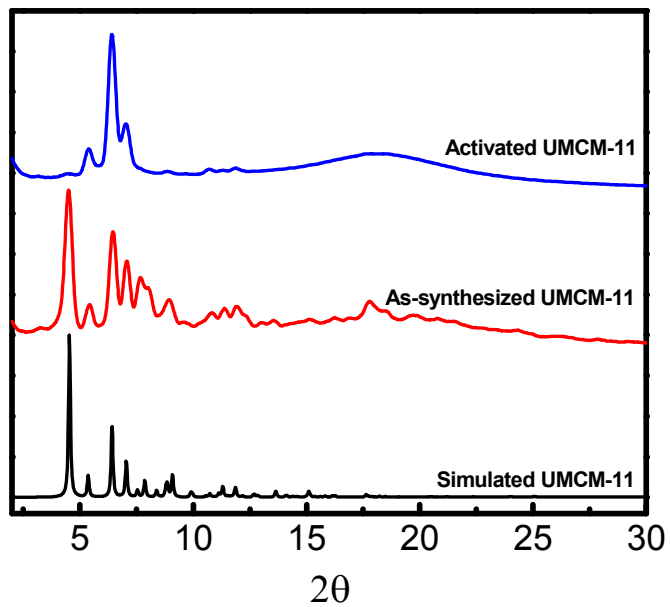


Figure 2. 8. Powder XRD patterns of UMCM-11 (black: simulated, red: as synthesized, blue: activated).

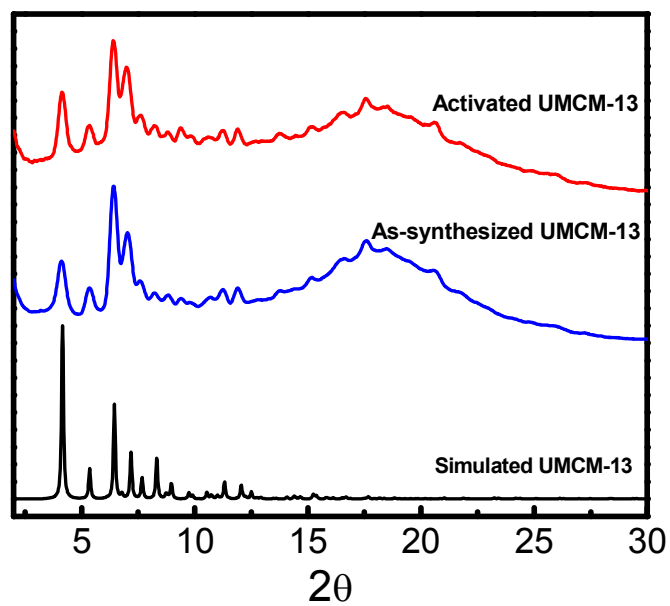


Figure 2. 9. Powder XRD patterns of UMCM-12 (black: simulated, blue: as synthesized, red: activated).

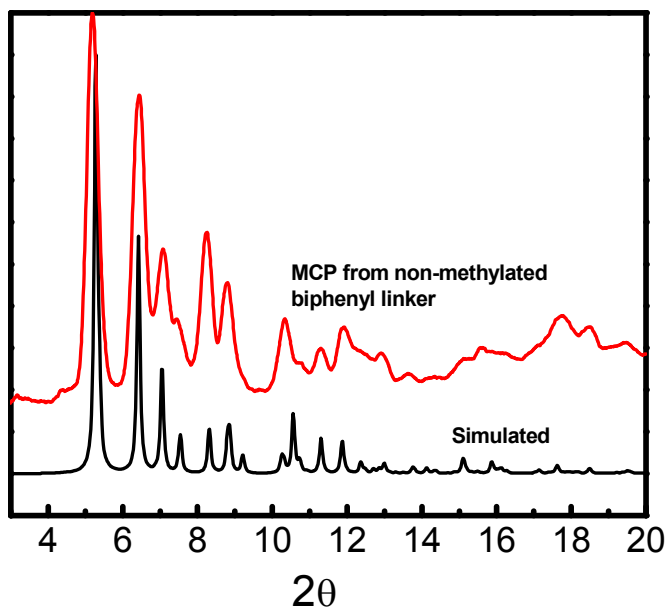


Figure 2. 10. Powder XRD patterns of MCP synthesized using biphenyl pillar linker (black: simulated, red: experimental).

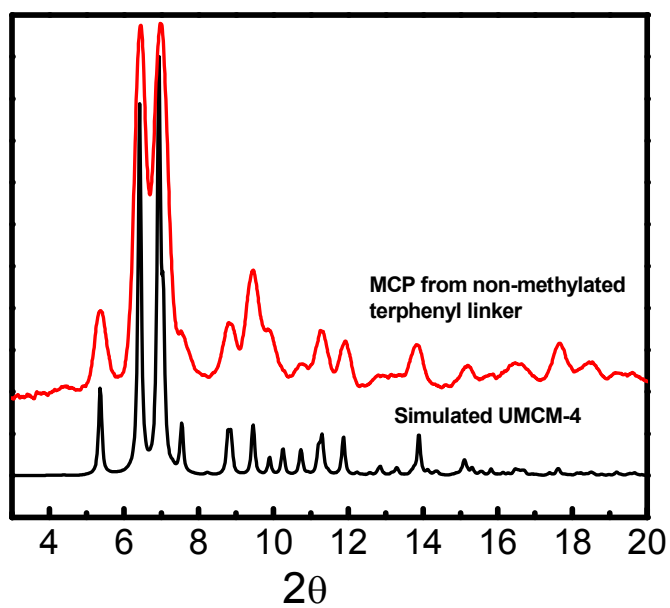


Figure 2. 11. Powder XRD patterns of MCP synthesized using terphenyl pillar linker (black: simulated, red: experimental).

### 2.4.3 Single Crystal X-Ray Diffraction for UMCM-10 and -12

Crystals of UMCM-10  $[\text{Zn}_4\text{O}(\text{TPA})(\text{TMBPDC})(\text{BDC})_{0.5}]_n$  exchanged in  $\text{CH}_2\text{Cl}_2$  were coated in Paratone N oil. A clear block of a crystal ( $0.18 \times 0.12 \times 0.10 \text{ mm}^3$ ) was mounted on a MitiGen MicroMount tip. X-ray diffraction data were collected on a Rigaku R-Axis Spider diffractometer (460 mm  $\times$  256 mm curved imaging plate detector, crystal-to-detector distance was 127.40 mm, graphite monochromated Cu  $K\alpha$  radiation at 2 kW power) at 233 K. A total of 401 oscillation images were collected using widths of  $1.5^\circ$  in  $\omega$ . The exposure time was 8 minutes for all images. Data were collected using the d\*TREK package in the CrystalClear software suite (v. 2.0, Rigaku 2009) to obtain overlapping  $\varphi$  and  $\omega$  scans. Using the FS\_PROCESS package in CrystalClear, the raw intensity data were then reduced to  $F^2$  values with corrections for Lorentz, and polarization effects. Decay of the crystal during data collection was negligible. An empirical absorption correction was applied as implemented by FS\_PROCESS. The structure was solved by direct methods and refined against all data using the CrystalStructure (v. 4.0) software package in the monoclinic space group  $P2_1/c$  (#14)  $Z = 4$  using SHELXL-97 in the crystal structure (v.4.0) software package.<sup>43</sup> Hydrogen atoms were placed at calculated positions (C-H = 0.93 Å) using a riding model with isotropic thermal parameters 1.2 times that of the attached carbon atom. Thermal parameters for all non-hydrogen atoms were refined anisotropically.

Crystals of UMCM-12  $[\text{Zn}_4\text{O}(\text{TPA})(\text{TMBPDC})(\text{BDC})_{0.5}]_n$  exchanged in  $\text{CH}_2\text{Cl}_2$  were coated in Paratone N oil. A clear block of a crystal ( $0.18 \times 0.18 \times 0.06 \text{ mm}^3$ ) was mounted on a cryoloop. X-ray diffraction data were collected on a Rigaku AFC10K Saturn 944+ CCD-based X-ray diffractometer equipped with a low temperature device and Micromax-007HF Cu-target micro-focus rotating anode ( $\lambda = 1.54187 \text{ \AA}$ ) operated at 1.2 kW power (crystal-to-detector

distance was 42.00 mm) at 95K. A total of 2068 images were collected with an oscillation width of 1.0° in  $\omega$ . The exposure time was 10 sec. for the low angle images, 45 sec. for high angle. Analysis of the data showed negligible decay during data collection; the data were processed with CrystalClear 2.0 and corrected for absorption. The structure was solved and refined with the Bruker SHELXTL (version 2008/4) software package, using the space group Pnma with Z = 4 for the formula C<sub>98</sub>H<sub>68</sub>N<sub>2</sub>O<sub>26</sub>Zn<sub>8</sub>. All non-hydrogen atoms were refined anisotropically with the hydrogen atoms placed in idealized positions. Full matrix least-squares refinement based on F<sup>2</sup> converged at R1 = 0.0651 and wR2 = 0.1473 [based on I > 2sigma(I)], R1 = 0.0966 and wR2 = 0.1525 for all data. The SQUEEZE<sup>44</sup> subroutine of the PLATON program suite was used to address the disordered solvent/oil in the large cavity present in the structure.

Table 2. 1. Crystal data and structure refinement for UMCM-10 and -12

Compound	UMCM-10	UMCM-12
Empirical formula	C <sub>43</sub> H <sub>30</sub> NO <sub>13</sub> Zn <sub>4</sub>	C <sub>98</sub> H <sub>68</sub> N <sub>2</sub> O <sub>26</sub> Zn <sub>8</sub>
Formula Weight	1030.23	2212.50
Temperature of run	233K	95K
Crystal dimensions	0.18 × 0.12 × 0.10 mm <sup>3</sup>	0.18 × 0.18 × 0.06 mm <sup>3</sup>
Wavelength	1.54187 Å	1.54187 Å
Crystal system	Monoclinic	Orthorhombic
Space group	P2 <sub>1</sub> /c	Pnma
Unit cell parameters	a = 17.1259(4) Å b = 32.5986(8) Å c = 25.1806(18) Å 13866.2(11) Å <sup>3</sup> α = 90° β = 99.471(7)° γ = 90°	a = 24.8949(5) Å b = 42.564(3) Å c = 32.7857(6) Å 34741(3) Å <sup>3</sup> α = 90° β = 90° γ = 90°
Z	4	4
Density (calculated)	0.493 g/cm <sup>3</sup>	0.423 g/cm <sup>3</sup>
Absorption coefficient	0.957 mm <sup>-1</sup>	0.776 mm <sup>-1</sup>
F(000)	2076	4472
Theta range for data collection	6.64 to 66.53	2.08 to 65.08
Index ranges	-20 ≤ h ≤ 19, -37 ≤ k ≤ 37, -23 ≤ l ≤ 29	-29 ≤ h ≤ 29, -50 ≤ k ≤ 50, -38 ≤ l ≤ 38



Reflections collected	108598	473511
Independent reflections	24085 [R(int) = 0.0727]	30035 [R(int) = 0.2638]
Completeness to highest theta	98.4 %	99.9 %
Absorption correction	multi-scan	Semi-empirical from equivalents
Max. and min. transmission	1.000 and 0.724	0.9549 and 0.8729
Refinement method	Full-matrix least-squares on F <sup>2</sup>	Full-matrix least-squares on F <sup>2</sup>
Data/ Restraints/ parameter	24085 / 0 / 550	30035 / 381 / 604
Goodness of fit on F <sup>2</sup>	1.197	1.033
Final R indices [I > 2σ(I)] <sup>a,b</sup>	R1 = 0.109, wR2 = 0.3315	R1 = 0.0651, wR2 = 0.1473
R indices (all data) <sup>a,b</sup>	R1 = 0.1594, wR2 = 0.3829	R1 = 0.0966, wR2 = 0.1525

$wR2 = \frac{|\sum w(|Fo|^2 - |Fc|^2)|}{\sum w(Fo^2)^{1/2}}$ ,  $w = 1 / [\sigma^2(Fo^2) + (mP)^2 + nP]$  and  $P = [\max(Fo^2, 0) + 2Fc^2] / 3$  ( $m$  and  $n$  are constants);  $\sigma = [\sum [w(Fo^2 - Fc^2)^2] / (n - p)]^{1/2}$  b)  $R1 = \frac{\sum ||Fo| - |Fc||}{\sum |Fo|}$

#### 2.4.4 <sup>1</sup>H NMR Spectroscopic Data for UCMCM-10, -11, and -12

Solvent free materials were digested in 20% DCl in D<sub>2</sub>O diluted with d<sup>6</sup>-DMSO before performing NMR spectroscopic experiments.

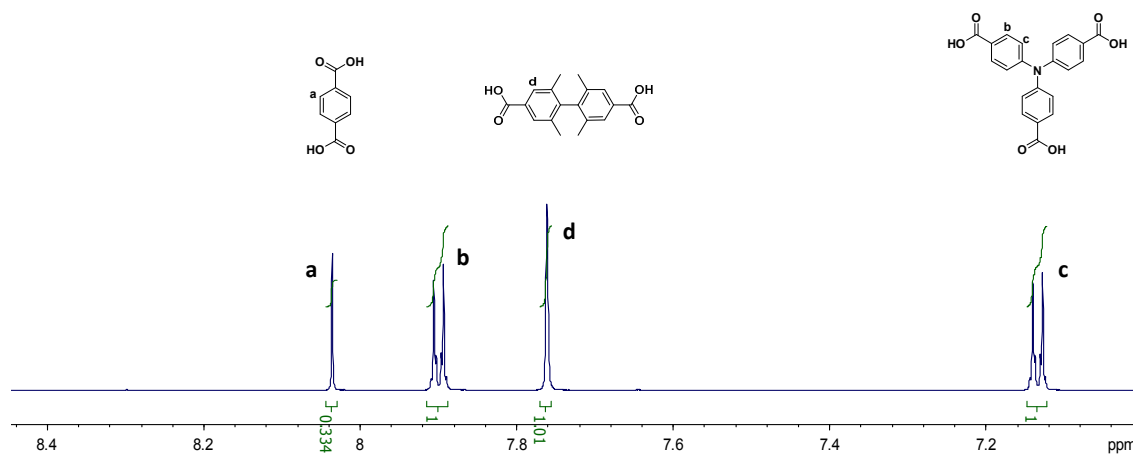


Figure 2. 12. <sup>1</sup>H NMR spectrum of activated UCMCM-10 digested in 20% DCl in D<sub>2</sub>O diluted with d<sup>6</sup>-DMSO.

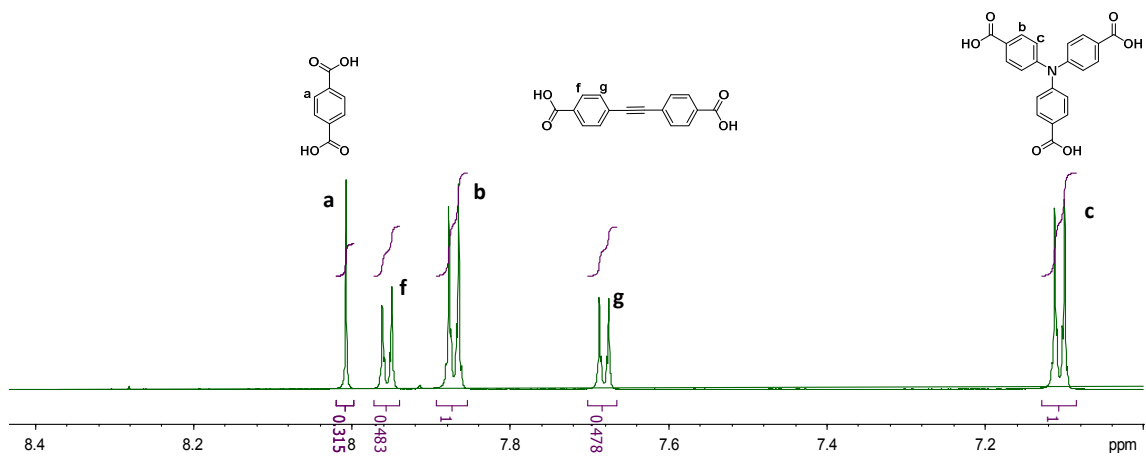


Figure 2. 13.  $^1\text{H}$  NMR spectrum of activated UMCM-11 digested in 20% DCl in  $\text{D}_2\text{O}$  diluted with  $\text{d}^6$ -DMSO.

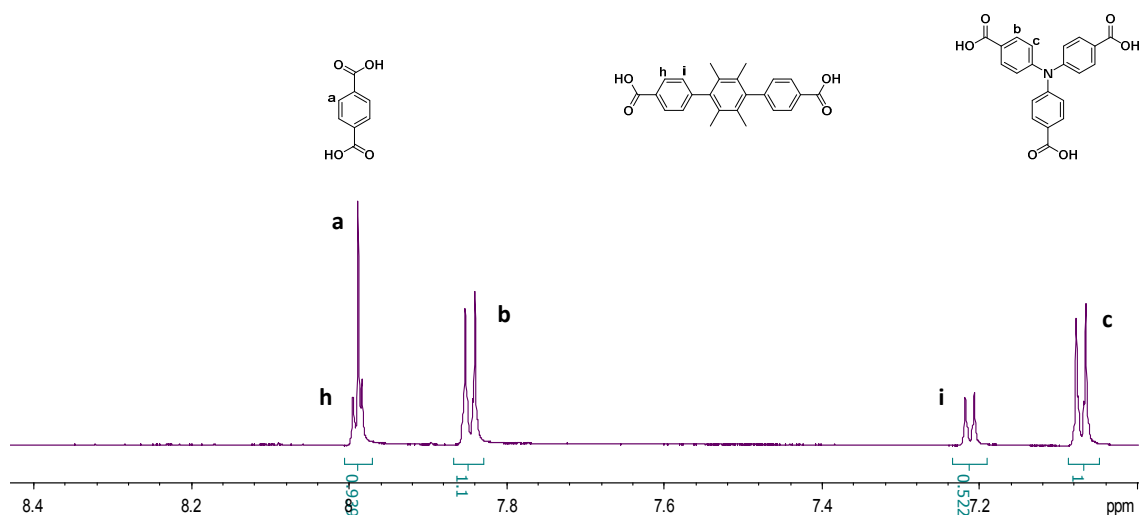


Figure 2. 14.  $^1\text{H}$  NMR spectrum of activated UMCM-12 digested in 20% DCl in  $\text{D}_2\text{O}$  diluted with  $\text{d}^6$ -DMSO.

### 2.4.5 TGA Traces of UMCM-10, -11, and -12

Thermogravimetric analyses were performed on a TA Instruments Q50. Samples were evacuated prior to analysis. The temperature was ramped from 25 °C to 600 °C with a rate of 2 °C/ min under a flow of N<sub>2</sub> gas.

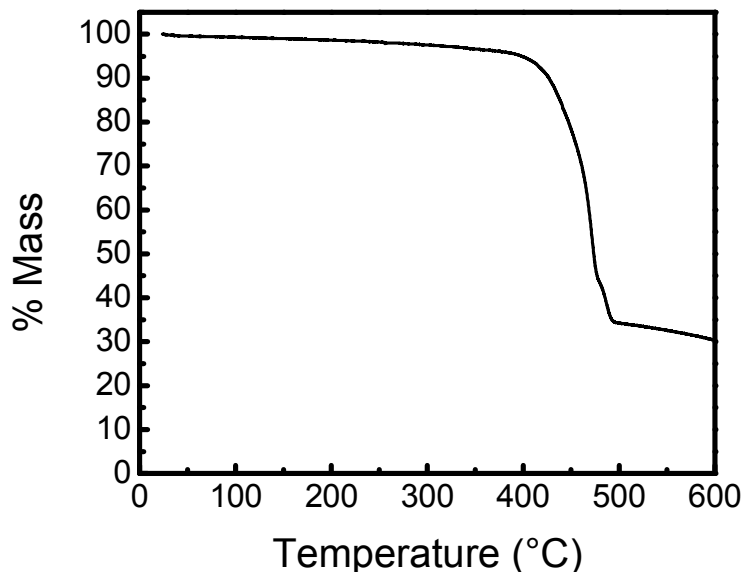


Figure 2. 15. TGA trace of activated UMCM-10.

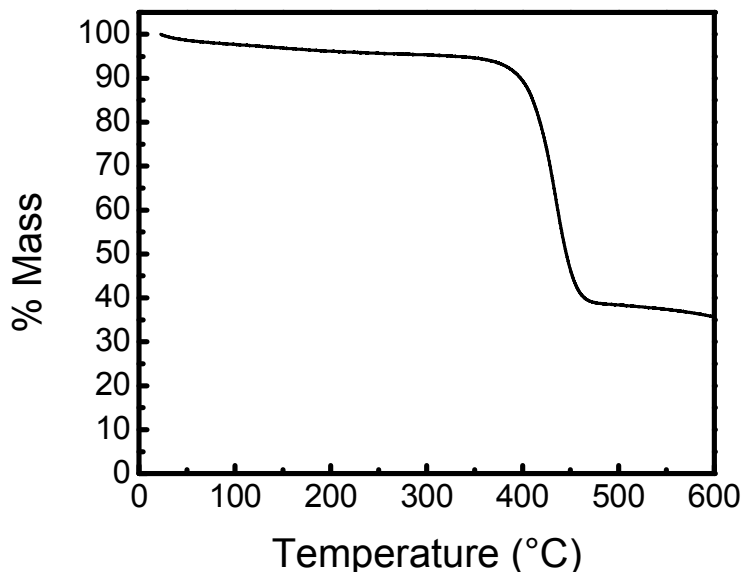


Figure 2. 16. TGA trace of activated UMCM-11.

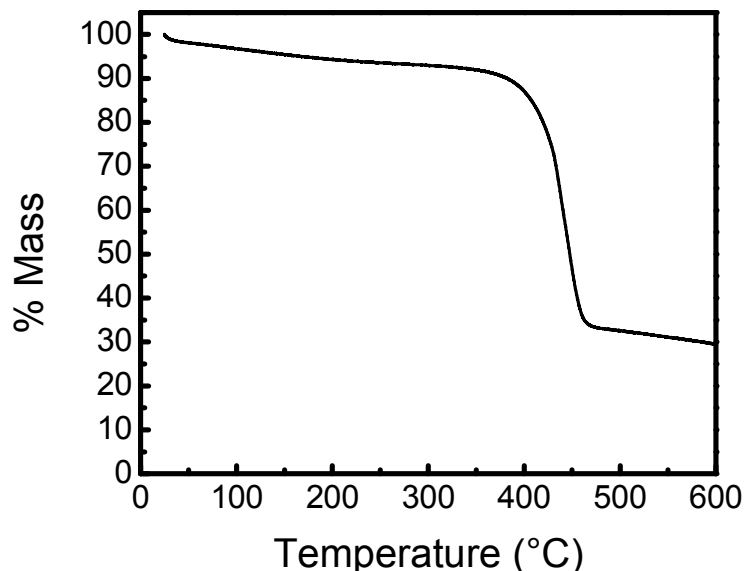


Figure 2. 17. TGA trace of activated UMCM-12.

#### 2.4.6 Gas Sorption Measurements of UMCM-4, -10, -11, and -12

N<sub>2</sub> adsorption/ desorption isotherms were measured volumetrically at 77K in the range of  $1.00 \times 10^{-5} \leq P/P_0 \leq 1.00$  with an Autosorb-1C outfitted with the micropore option by Quantachrome Instruments (Boyton Beach, Florida, U.S.A.) running version 1.2 ASwin software package. Ultra-high purity He (99.999%, for void volume determination) and N<sub>2</sub> (99.999%) were purchased from Cryogenic Gases and used as received.

Ar sorption experiments were performed in order to determine pore size distribution of materials at 87K in the range of  $1.00 \times 10^{-5} \leq P/P_0 \leq 1.00$ . Ultra-high purity Ar (99.999%) was purchased from Cryogenic Gasses. Pore size distributions were calculated applying Non-linear Density Functional Theory (NLDFT) zeolite/silica equilibrium transition kernel for Ar sorption at 87K based on cylindrical pore model as implemented in version 1.2 of the ASWin software package.

H<sub>2</sub> and CO<sub>2</sub> adsorption/ desorption isotherms were measured volumetrically at 77K and 195 K respectively with an Autosorb-1C outfitted with the micropore option by Quantachrome Instruments (Boyton Beach, Florida, U.S.A.) running version 1.2 ASwin software package. Ultra-high purity H<sub>2</sub> (99.999%) and CO<sub>2</sub> (99.999%) were purchased from Cryogenic Gases and used as received.

Table 2. 2. Predicted and experimental surface areas for activated materials obtained from N<sub>2</sub> isotherms

MCP	Predicted surface area (m <sup>2</sup> /g) <sup>45</sup>	Experimental BET surface area (m <sup>2</sup> /g) determined from BET plots following self-consistency criterion <sup>46</sup>
UMCM-4	3725	3632
UMCM-10	4475	4001
UMCM-11	4617	1525
UMCM-12	4756	4849

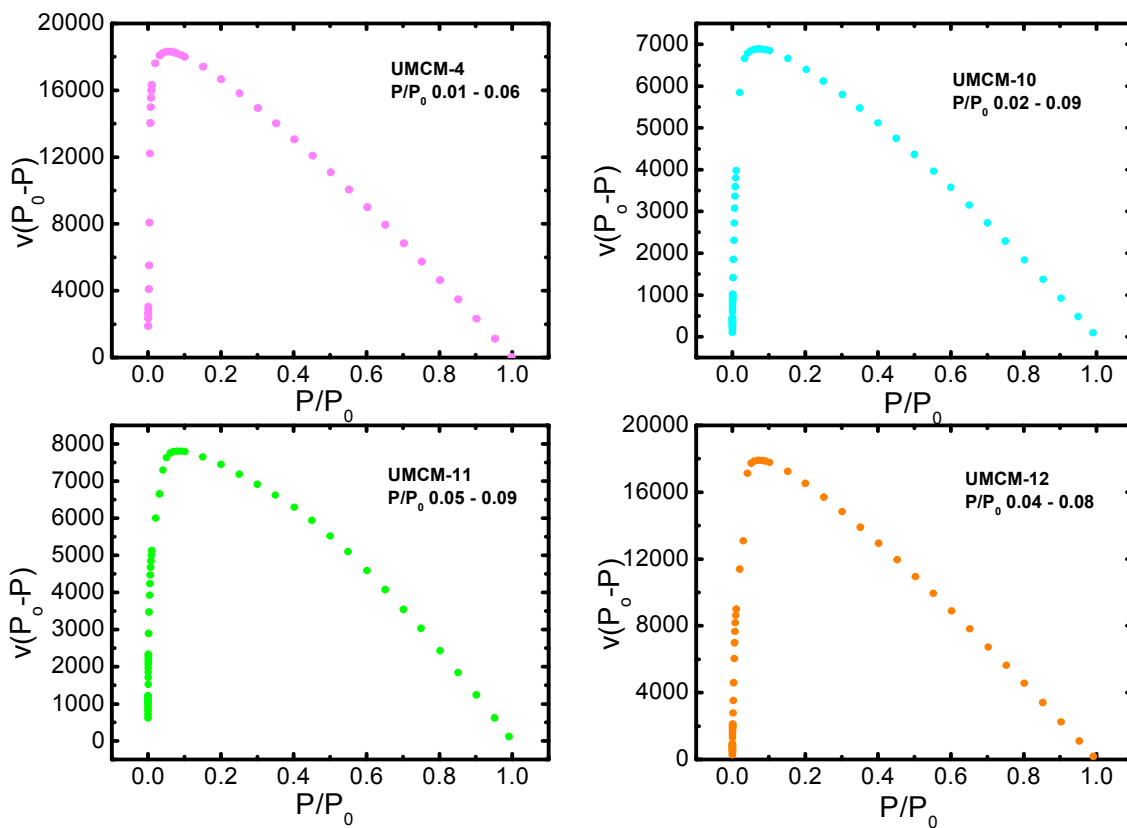


Figure 2. 18. Self-consistency plots for determining  $P/P_0$  range for BET analysis based on isotherms shown in Figure 2.5.

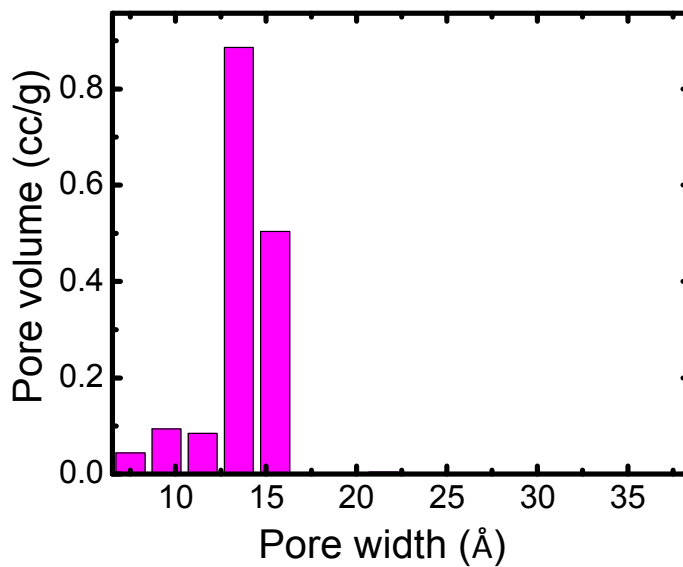


Figure 2. 19. Pore size distribution of activated UMCM-4.

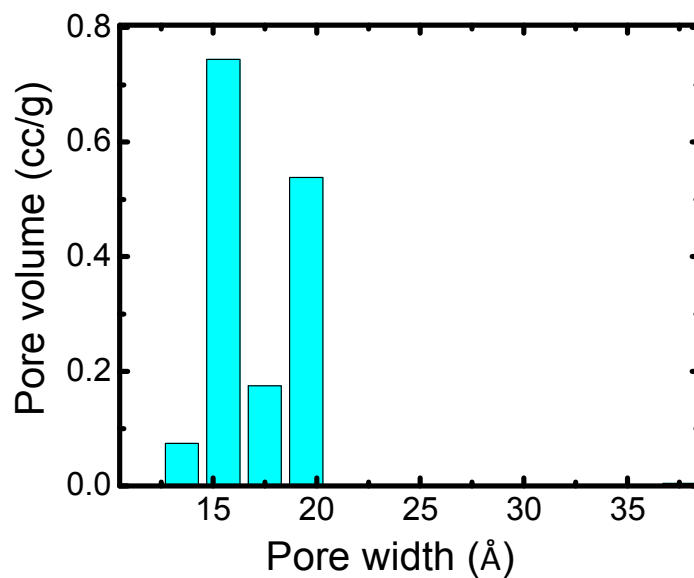


Figure 2. 20. Pore size distribution of activated UMCM-10.

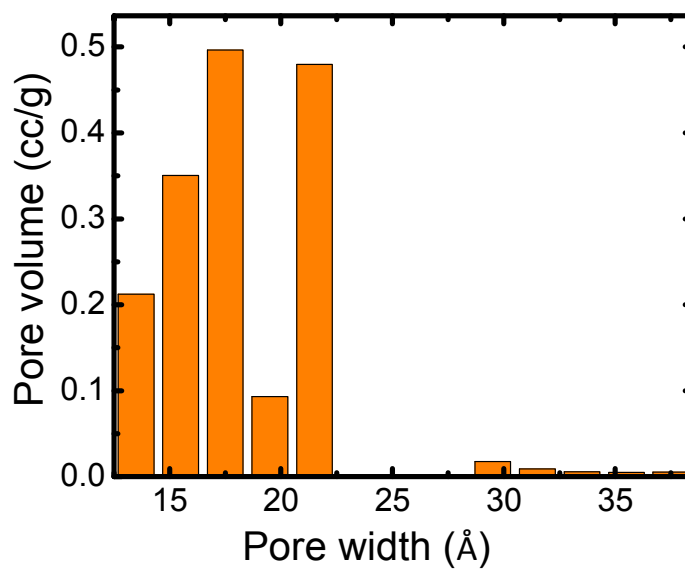


Figure 2. 21. Pore size distribution of activated UMCM-12.

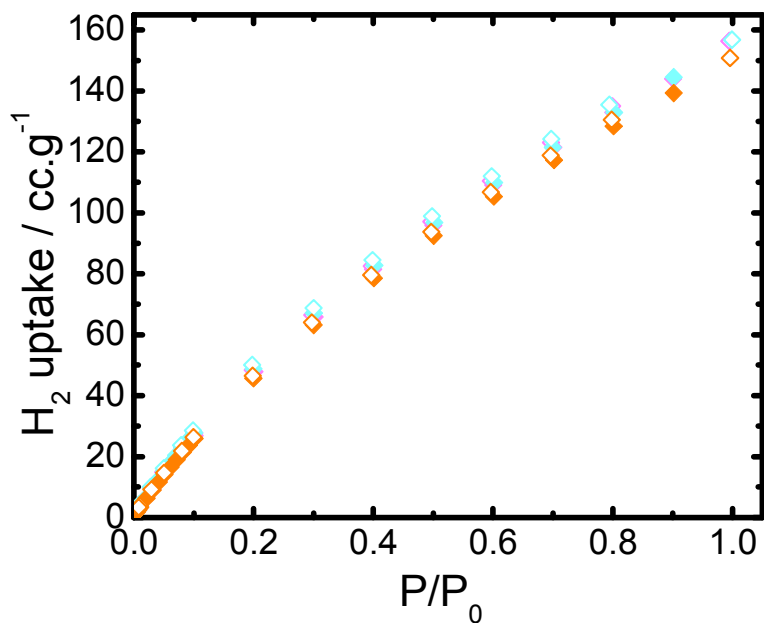


Figure 2. 22. H<sub>2</sub> sorption isotherms of UMCM-4 (purple), and -12 (orange), and -10 (blue).

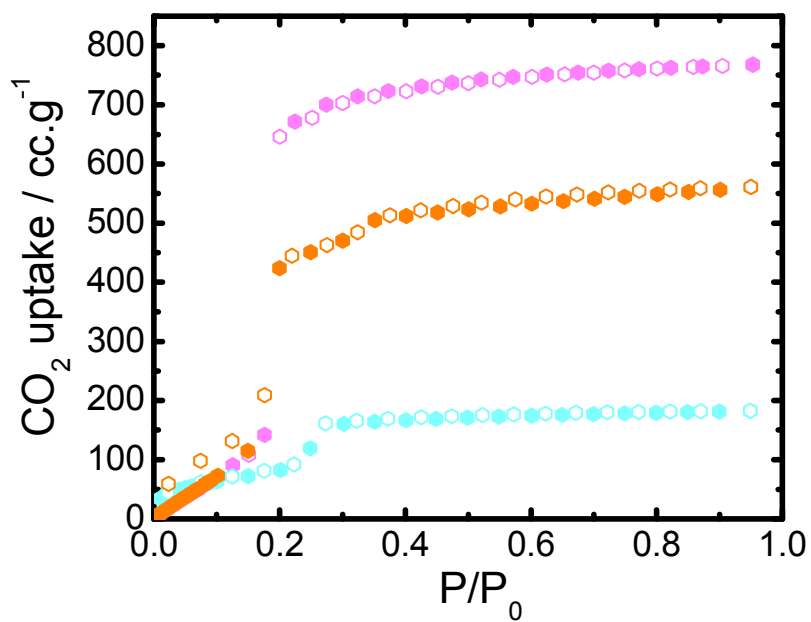


Figure 2. 23. CO<sub>2</sub> sorption isotherms of UMCM-4 (purple), and -12 (orange), and -10 (blue).



### 2.4.7 PXRD Patterns of UMCM-4, -10, and -12 at Elevated Temperatures and Air

Variable temperature powder X-ray diffraction data were collected on a Bruker D8 Advance Diffractometer having Bragg-Brentano geometry. The  $\text{CuK}\alpha$  radiation source was operated at 40 V and 40 mA. Activated samples were ground and evenly dispersed on a low background quartz plate placed on a hot stage. The diffraction patterns were collected at different temperatures at a 1 sec/step scan rate.

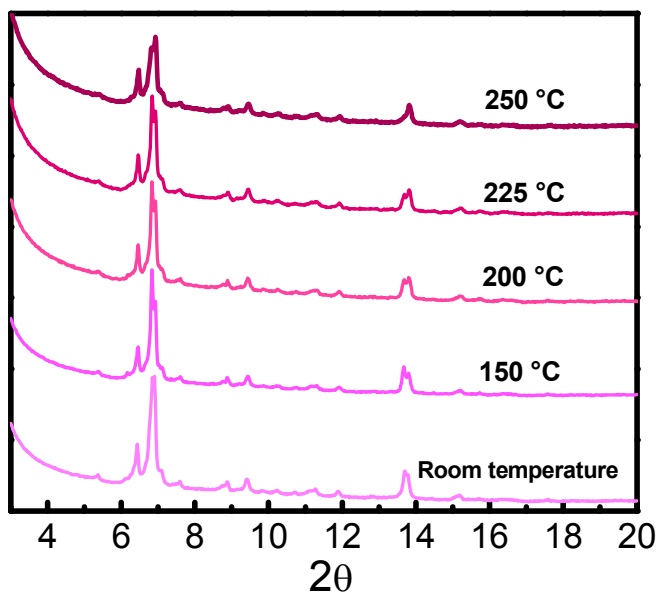


Figure 2. 24. PXRD patterns of activated UMCM-4 at different temperatures.

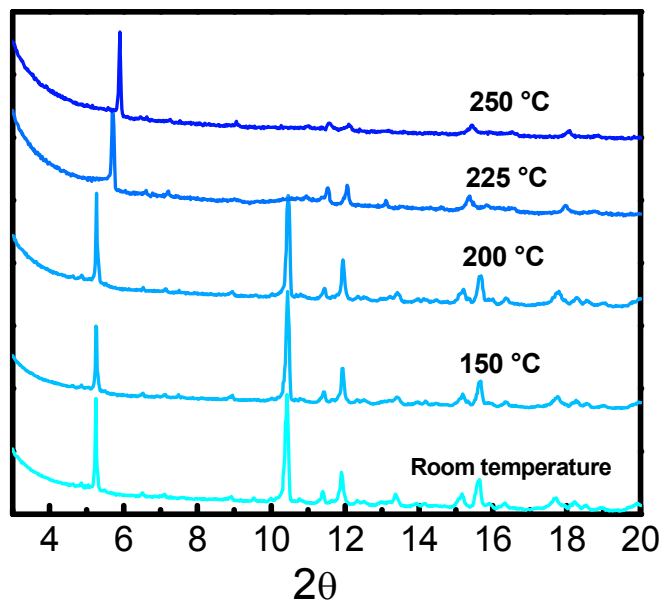


Figure 2. 25. PXRD patterns of activated UMCM-10 at different temperatures.

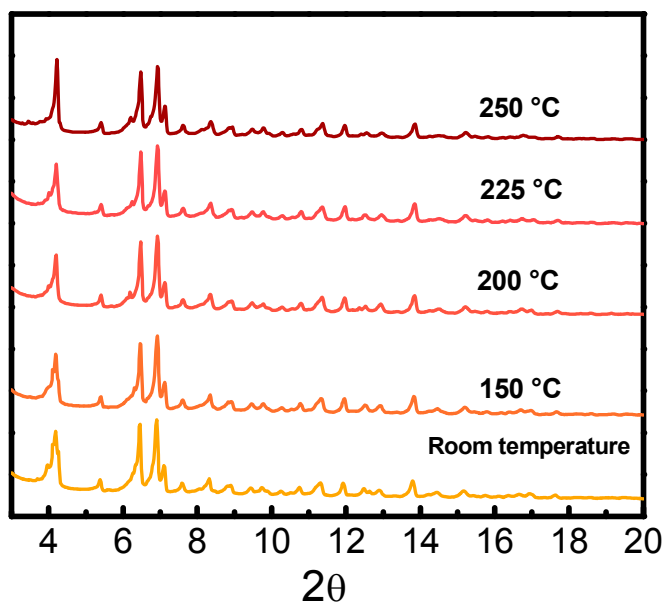


Figure 2. 26. PXRD patterns of activated UMCM-12 at different temperatures.

Samples after exposure to air for 12 hours were soaked in mineral oil before collection of powder X-ray diffraction data. Data were collected on Rigaku R-Axis Spider diffractometer with

an image plate detector and  $\text{CuK}\alpha$  radiation operating in transmission mode. The powder samples were rotated on the goniometer in  $\varphi$  and oscillated in  $\omega$  to minimize preferred orientation.

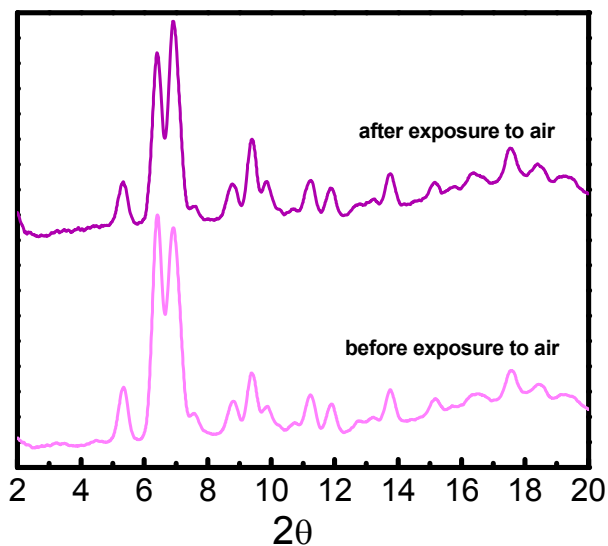


Figure 2. 27. PXRd patterns of activated UMCM-4 before and after exposure to air.

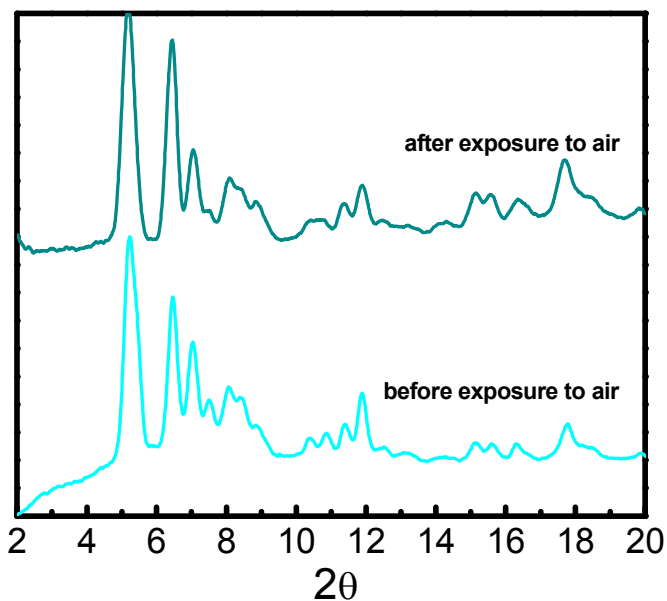


Figure 2. 28. PXRd patterns of activated UMCM-10 before and after exposure to air.

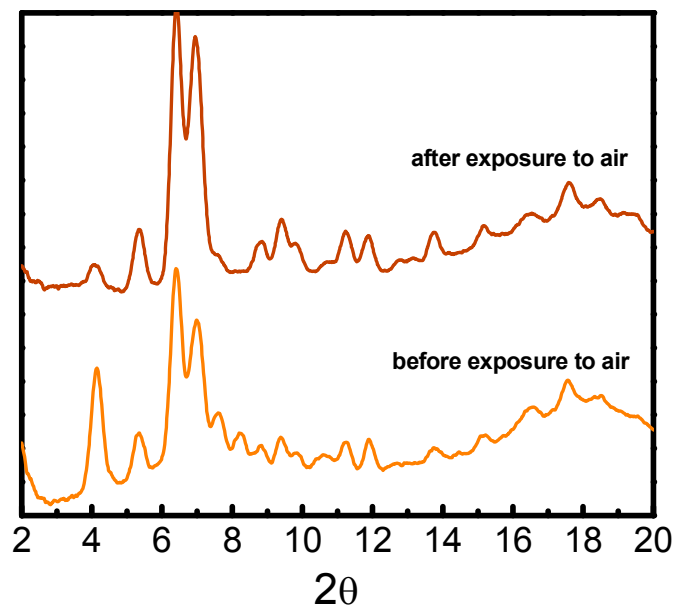


Figure 2. 29. PXRD patterns of activated UMCM-12 before and after exposure to air.

## 2.4.8 Microscopic Images of Dye Diffusion Experiments

MCP crystals were immersed in  $\text{CH}_2\text{Cl}_2$  solution saturated with dye and containing additional solid dye solution at room temperature for 1 day and then washed with fresh  $\text{CH}_2\text{Cl}_2$  5 times followed by immersion in mineral oil. Optical micrographs of crystals after dye impregnation were taken with a Spot Flex camera fixed to a Leica DMLP microscope. All scale bars indicate a distance of 100  $\mu\text{m}$ . In each case, the crystals were sectioned to confirm that dye had penetrated to the centers of the crystals rather than outer surfaces.

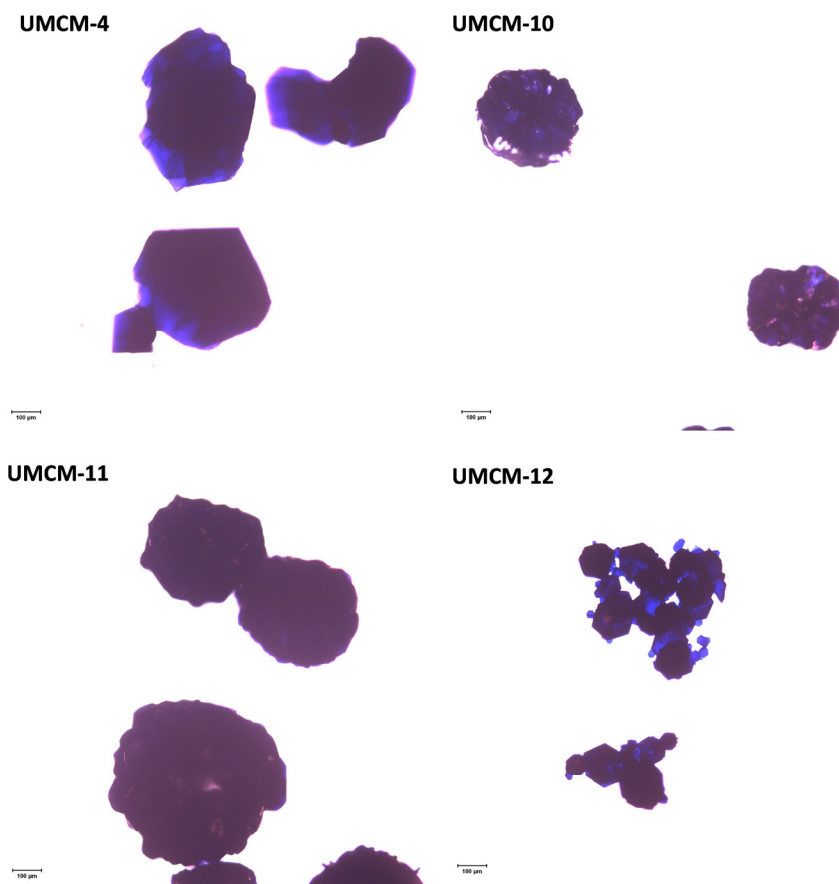


Figure 2. 30. Microscopic images of dyed crystals of UMCM-4, -10, -11, and -12 after Nile red dye diffusion.

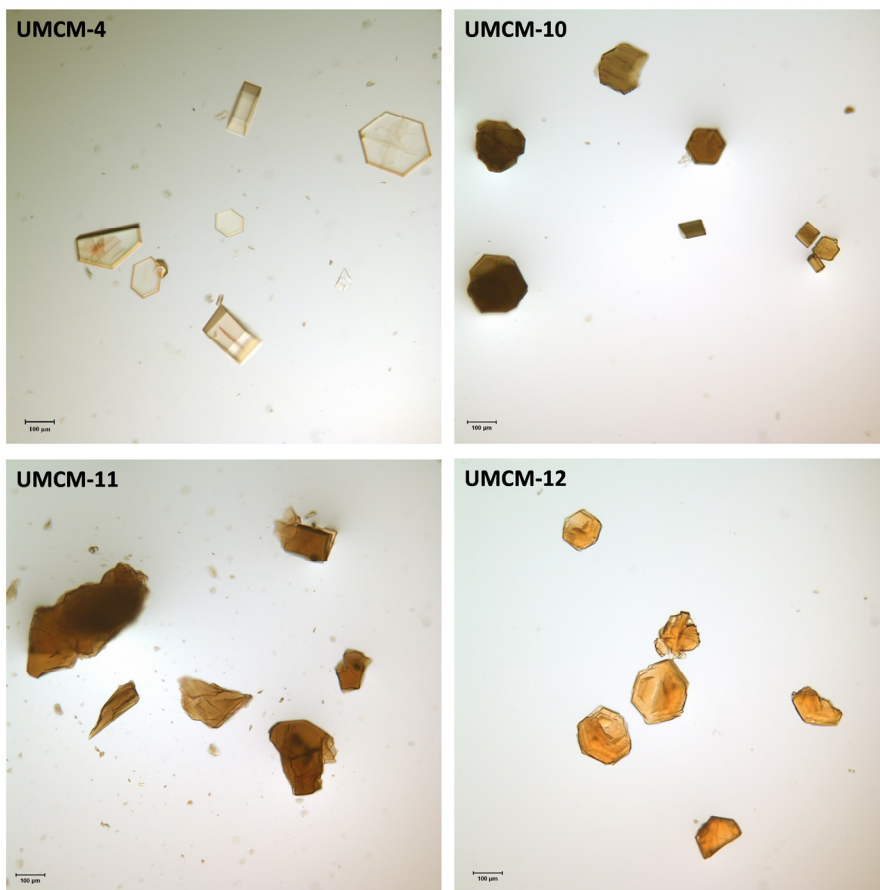


Figure 2. 31. Microscopic images of dyed crystals of UMCM-4, -10, -11, and -12 after Reichardt's dye diffusion.

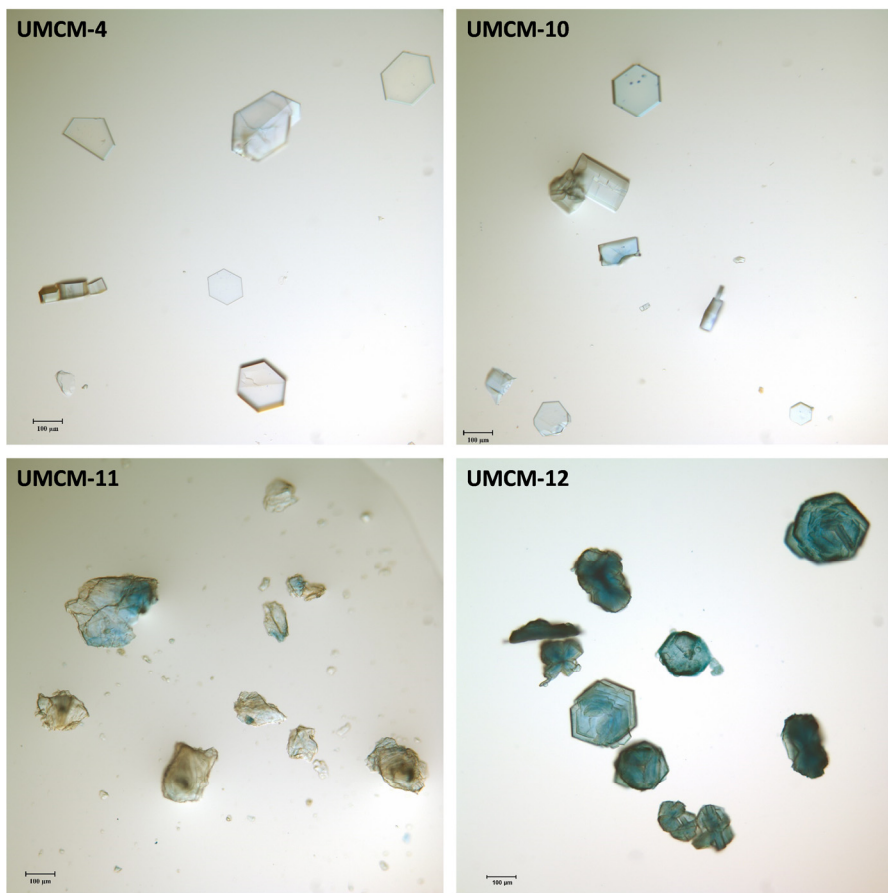


Figure 2. 32. Microscopic images of dyed crystals of UMCM-4, -10, -11, and -12 after Coomassie Brilliant Blue dye diffusion.

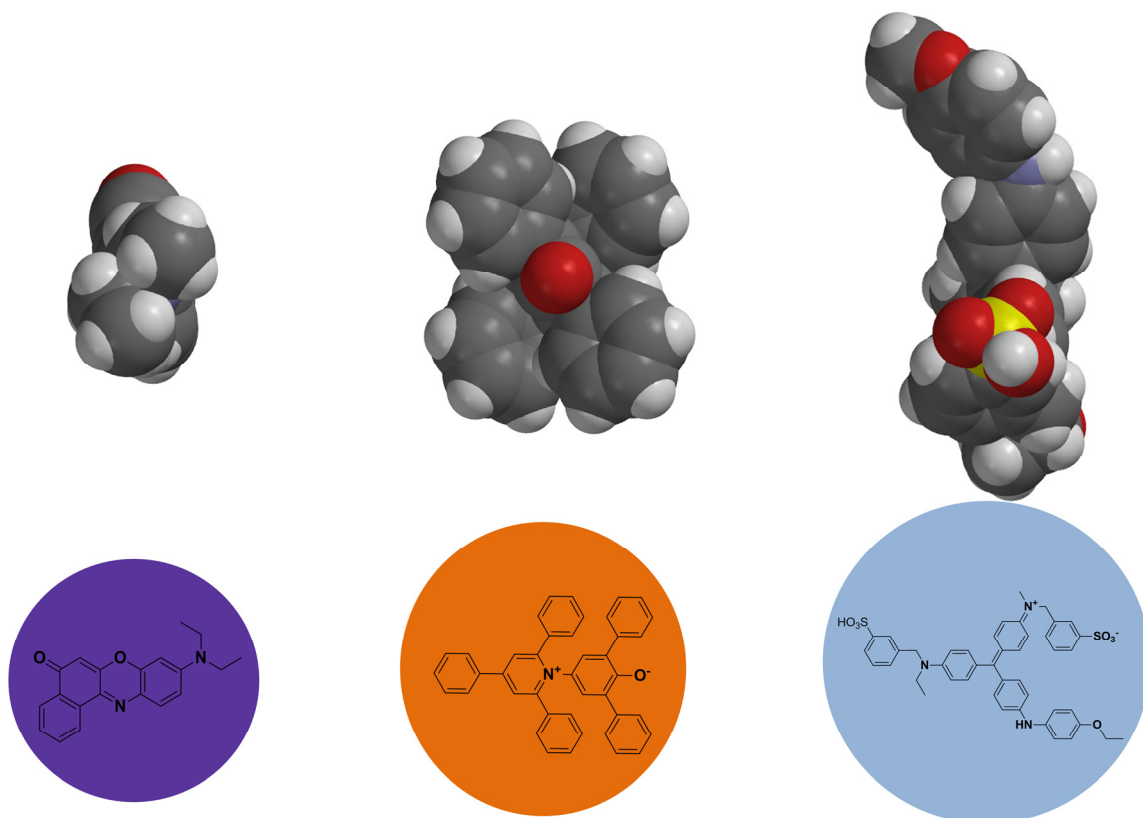


Figure 2. 33. Kinetic diameters of dye molecules were approximated using the minimum cross-sectional area and taking van der Waals radii of atoms into account.

#### 2.4.9 Linear Dichroism Experiment on UMCM-4 Crystals

Optical micrographs of UMCM-4 crystals housing (Figures 2.33) after Nile Red dye diffusion were taken with a Spot Flex camera fixed to a Leica DMLP microscope. The systematic alignment of dye inside the pores of UMCM-4 causes different absorbance of light linearly polarized with different direction.



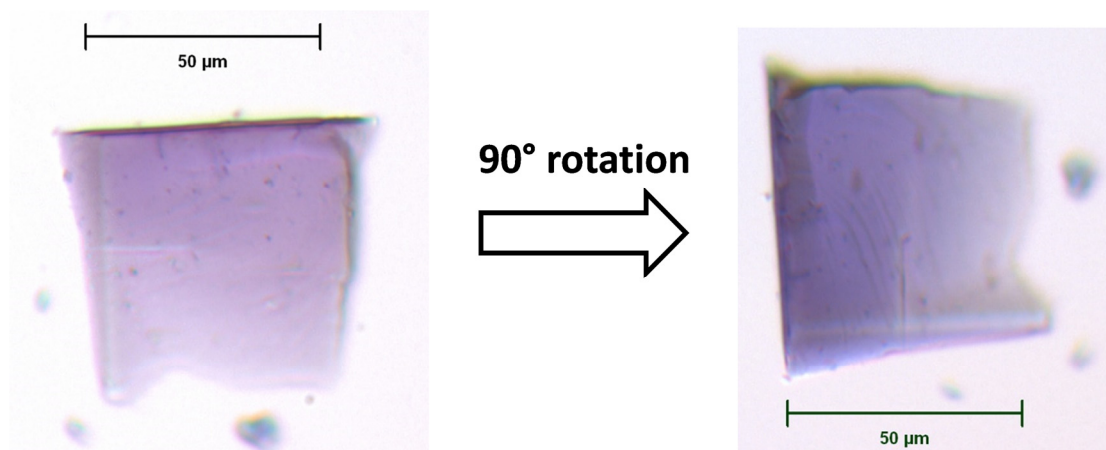


Figure 2. 34. Microscopic images of UCMCM-4 crystal housing oriented Nile Red dye molecules taken before and after 90° rotation with respect to plane polarized light. Exposure time was held constant.

## 2.5 References

1. A. Clearfield and M. Kuchenmeister, *ACS Symp. Ser.*, 1992, **499**, 128-144.
2. M. Kondo, T. Okubo, A. Asami, S.-i. Noro, T. Yoshitomi, S. Kitagawa, T. Ishii, H. Matsuzaka and K. Seki, *Angew. Chem. Int. Ed.*, 1999, **38**, 140-143. It should be noted that the pillared-layer strategy from crystal engineering standpoint was introduced before 1999. See for an example: V. A. Russell, C. C. Evans. W. Li, M. D. Ward, *Science*, 1997, **276**, 575-578.
3. At least one example derived from pinwheel trinuclear zinc carboxylate clusters shows systematic modulation of structure with variation of pillar. A. -L. Cheng, Y. Ma, Q. Sun and E. -Q. Gao, *CrystEngComm*, 2011, **13**, 2721-2726.
4. D. N. Dybtsev, H. Chun and K. Kim, *Angew. Chem. Int. Ed.*, 2004, **43**, 5033-5036.
5. H. Sakamoto, R. Matsuda and S. Kitagawa, *Dalton Trans.*, 2012, **41**, 3956-3961.
6. H. Sakamoto, R. Kitaura, R. Matsuda, S. Kitagawa, Y. Kubota and M. Takata, *Chem. Lett.*, 2010, **39**, 218-219.
7. B.-Q. Ma, K. L. Mulfort and J. T. Hupp, *Inorg. Chem.*, 2005, **44**, 4912-4914.
8. P. Nugent, Y. Belmabkhout, S. D. Burd, A. J. Cairns, R. Luebke, K. Forrest, T. Pham, S. Ma, B. Space, L. Wojtas, M. Eddaoudi and M. J. Zaworotko, *Nature*, 2013, **495**, 80-84.
9. P. Nugent, V. Rhodus, T. Pham, B. Tudor, K. Forrest, L. Wojtas, B. Space and M. Zaworotko, *Chem. Commun.*, 2013, **49**, 1606-1608.
10. Y.-Y. Lin, Y.-B. Zhang, J.-P. Zhang and X.-M. Chen, *Cryst. Growth Des.*, 2008, **8**, 3673-3679.
11. J. Seo, R. Matsuda, H. Sakamoto, C. Bonneau and S. Kitagawa, *J. Am. Chem. Soc.*, 2009, **131**, 12792-12800.
12. S. Ma, D. Sun, P. M. Forster, D. Yuan, W. Zhuang, Y.-S. Chen, J. B. Parise and H.-C. Zhou, *Inorg. Chem.*, 2009, **48**, 4616-4618.

13. R. Kitaura, K. Seki, G. Akiyama and S. Kitagawa, *Angew. Chem. Int. Ed.*, 2003, **42**, 428-431.
14. R. Kitaura, K. Fujimoto, S.-i. Noro, M. Kondo and S. Kitagawa, *Angew. Chem. Int. Ed.*, 2002, **41**, 133-135.
15. T. Gadzikwa, B.-S. Zeng, J. T. Hupp and S. T. Nguyen, *Chem. Commun.*, 2008, 3672-3674.
16. J. Seo, C. Bonneau, R. Matsuda, M. Takata and S. Kitagawa, *J. Am. Chem. Soc.*, 2011, **133**, 9005-9013.
17. T. K. Maji, R. Matsuda and S. Kitagawa, *Nat. Mater.*, 2007, **6**, 142-148.
18. B. Chen, S. Ma, F. Zapata, F. R. Fronczek, E. B. Lobkovsky and H.-C. Zhou, *Inorg. Chem.*, 2007, **46**, 1233-1236.
19. K. L. Mulfort and J. T. Hupp, *J. Am. Chem. Soc.*, 2007, **129**, 9604-9605.
20. K. Koh, A. G. Wong-Foy and A. J. Matzger, *J. Am. Chem. Soc.*, 2010, **132**, 15005-15010.
21. H. K. Chae, D. Y. Siberio-Pérez, J. Kim, Y. Go, M. Eddaoudi, A. J. Matzger, M. O'Keeffe and O. M. Yaghi, *Nature*, 2004, **427**, 523-527.
22. J. F. Eubank, F. Nouar, R. Luebke, A. J. Cairns, L. Wojtas, M. Alkordi, T. Bousquet, M. R. Hight, J. Eckert, J. P. Embs, P. A. Georgiev and M. Eddaoudi, *Angew. Chem. Int. Ed.*, 2012, **51**, 10099-10103.
23. M. Eddaoudi, J. Kim, N. Rosi, D. Vodak, J. Wachter, M. O'Keeffe and O. M. Yaghi, *Science*, 2002, **295**, 469-472.
24. X. Lin, I. Telepeni, A. J. Blake, A. Dailly, C. M. Brown, J. M. Simmons, M. Zoppi, G. S. Walker, K. M. Thomas, T. J. Mays, P. Hubberstey, N. R. Champness and M. Schröder, *J. Am. Chem. Soc.*, 2009, **131**, 2159-2171.
25. Crystal data for UMCM-10: C<sub>43</sub>H<sub>30</sub>NO<sub>13</sub>Zn<sub>4</sub>, M = 1030.23, monoclinic, a = 17.1259(4) Å, b = 32.5986(8) Å, c = 25.1806(18) Å, V = 13866.2(11) Å<sup>3</sup>, α = 90°, β = 99.471(7)°, γ = 90°, T = 233 K, space group P21/c, Z = 4, μ(CuKα) = 1.54187 Å<sup>-1</sup>, 108598 reflections measured, 24085 independent reflections (R<sub>int</sub> = 0.0727). The final R<sub>1</sub> values were 0.109 (I > 2σ(I)). The final wR(F<sub>2</sub>) values were 0.3315 (I > 2σ(I)). The final R<sub>1</sub> values were 0.1594 (all data). The final wR(F<sub>2</sub>) values were 0.3829 (all data). Crystal data for UMCM-12: C<sub>98</sub>H<sub>68</sub>N<sub>2</sub>O<sub>26</sub>Zn<sub>8</sub>, M = 2212.50, orthorhombic, a = 24.8949(5) Å, b = 42.564(3) Å, c = 32.7857(6) Å, V = 34741(3) Å<sup>3</sup>, α = 90°, β = 90°, γ = 90°, T = 95 K, space group Pnma, Z = 4, μ(CuKα) = 1.54187 Å<sup>-1</sup>, 473511 reflections measured, 30035 independent reflections (R<sub>int</sub> = 0.2638). The final R<sub>1</sub> values were 0.0651 (I > 2σ(I)). The final wR(F<sub>2</sub>) values were 0.1473 (I > 2σ(I)). The final R<sub>1</sub> values were 0.0966 (all data). The final wR(F<sub>2</sub>) values were 0.1525 (all data).
26. L. Liu, K. Konstas, M. R. Hill and S. G. Telfer, *J. Am. Chem. Soc.*, 2013, **135**, 17731-17734.
27. K. Koh, A. G. Wong-Foy and A. J. Matzger, *Angew. Chem. Int. Ed.*, 2008, **47**, 677-680.
28. H. K. Chae, J. Kim, O. D. Friedrichs, M. O'Keeffe and O. M. Yaghi, *Angew. Chem. Int. Ed.*, 2003, **42**, 3907-3909.
29. T.-H. Park, K. Koh, A. G. Wong-Foy and A. J. Matzger, *Cryst. Growth Des.*, 2011, **11**, 2059-2063.

30. J. K. Schnobrich, O. Lebel, K. A. Cychosz, A. Dailly, A. G. Wong-Foy and A. J. Matzger, *J. Am. Chem. Soc.*, 2010, **132**, 13941-13948.
31. J. K. Schnobrich, K. Koh, K. N. Sura and A. J. Matzger, *Langmuir*, 2010, **26**, 5808-5814.
32. T. Düren, F. Millange, G. Férey, K. S. Walton and R. Q. Snurr, *J. Phys. Chem. C*, 2007, **111**, 15350-15356.
33. FJI-I is constructed from Zn-paddlewheel, 4,4'-bipyridine and BTB and exhibits high surface area. However, it is not a pillared-layer MCP. D. Han, F. -L. Jiang, M. -Y. Wu, L. Chen, Q. -H. Chen and M. -C. Hong, *Chem. Commun.*, 2011, **47**, 9861-9863.
34. B. Liu, A. G. Wong-Foy and A. J. Matzger, *Chem. Commun.*, 2013, **49**, 1419-1421.
35. W. A. Chalifoux, R. McDonald, M. J. Ferguson and R. R. Tykwinski, *Angew. Chem. Int. Ed.*, 2009, **48**, 7915-7919.
36. M. P. Suh, H. J. Park, T. K. Prasad, D. -W. Lim, *Chem. Rev.*, 2012, **112**, 782-835.
37. K. A. Cychosz, R. Ahmad and A. J. Matzger, *Chem. Sci.*, 2010, **1**, 293-302.
38. I. M. Walton, J. M. Cox, J. A. Coppin, C. M. Linderman, D. G. Patel and J. B. Benedict, *Chem. Commun.*, 2013, **49**, 8012-8014.
39. E. W. Thulstrup and J. Michl, *Spectrochim. Acta. Part A*, 1988, **44**, 767-782.
40. T.-H. Park, K. Koh, A. G. Wong-Foy and A. J. Matzger, *Cryst. Growth Des.*, 2011, **11**, 2059-2063.
41. T. M. Fasina, J. C. Collings, J. M. Burke, A. S. Batsanov, R. M. Ward, D. Albesa-Jove, L. Porres, A. Beeby, J. A. K. Howard, A. J. Scott, W. Clegg, S. W. Watt, C. Viney and T. B. Marder, *J. Mater. Chem.*, 2005, **15**, 690-697.
42. H.-L. Jiang, D. Feng, T.-F. Liu, J.-R. Li and H.-C. Zhou, *J. Am. Chem. Soc.*, 2012, **134**, 14690-14693.
43. G. M. Sheldrick, *SHELXS '97 and SHELXL '97*. (University of Göttingen, Germany, 1997).
44. a) A. L. Spek, *J. Appl. Cryst.*, 2003, **36**, 7-13 ; b) A. L. Spek, *Acta Cryst. D65*, 2009, v. **51012**, 148-155.
45. T. Düren, F. Millange, G. Férey, K. S. Walton and R. Q. Snurr, *J. Phys. Chem. C*, 2007, **111**, 15350-15356.
46. J. Rouquerol, P. Llewellyn and F. Rouquerol, *Studies in Surface Science and Catalysis*, 2007, **160**, 49-56 (Eds.: F. R.-R. J. R. P.L. Llewellyn, N. Seaton), Elsevier.

## Chapter 3

### A Non-regular Layer Arrangement of a Pillared-layer Coordination Polymer: Avoiding Interpenetration via Symmetry Breaking at Nodes

A. Dutta, J. Ma, A. J. Matzger, *manuscript in preparation*.

#### 3.1 Introduction

Microporous coordination polymers (MCPs), materials built from organic bridging linkers and metal ions or clusters have witnessed rapid and extensive development over the last two decades. Pillared-layer MCPs possessing the metal paddlewheel secondary building unit (SBU) and both carboxylate and neutral nitrogen based linkers are one of the earliest and most-studied classes of MCPs. DMOF<sup>1</sup>  $[\text{Zn}_2(\text{BDC})_2(\text{DABCO})]_n$  represents a prototype coordination polymer of this category and it is composed of dinuclear Zn paddlewheel SBUs bridged by 1,4-benzenedicarboxylate (BDC) to generate 2D layers of  $\text{Zn}_2(\text{BDC})_2$  which are connected in the third dimension by 1,4-diazabicyclo[2.2.2]octane (DABCO) pillars. The rational modulation of this type of pillared-layer structure has been demonstrated by many groups and can generally be categorized in two ways: a) control of the pillar dimension by replacing the DABCO with 4,4'-bipyridine or related analogues<sup>2</sup> and/or b) altering the 2D layer with alternative dicarboxylates to vary the dimension of the 2D grid.<sup>2</sup> However, extension of the pillaring linker to 4,4'-bipyridine, for an example, promotes framework interpenetration. An approach to avoid this interpenetration is substitution with alkyl<sup>2</sup>/alkoxy chains<sup>3, 4</sup> at different positions from the aromatic core of the carboxylate linkers. The dangling side chains block the void space of the framework suppressing

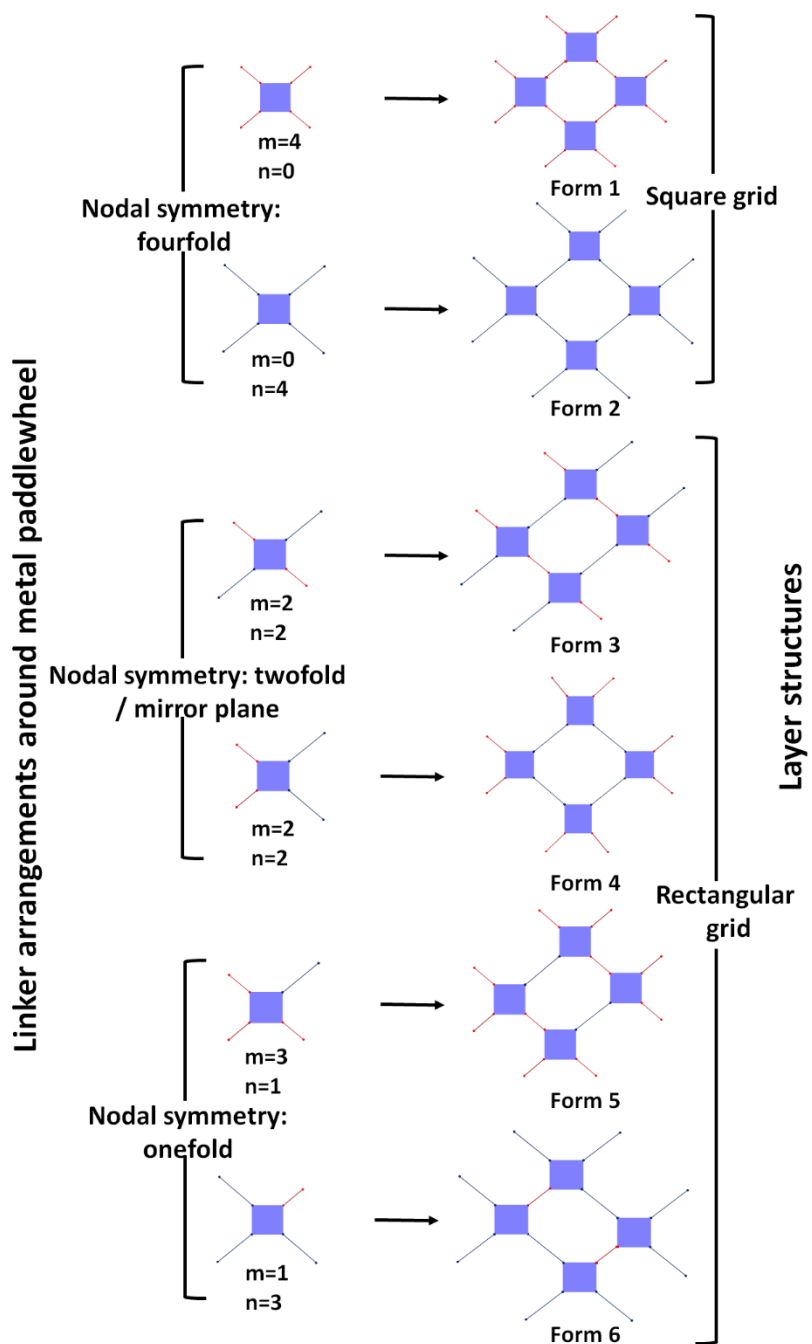


Figure 3. 1. Plausible arrangements of  $m$  short (red) and  $n$  long (blue) linkers around a 4-connected metal paddlewheel node (purple) ( $m+n=4$ ) and resultant layer structures from self-repetition of these units.

the intergrowth of the frameworks,<sup>2</sup> a strategy that also is effective for cubic MOFs.<sup>5</sup> However, the conformational freedom of carboxylate groups induced by the alkoxy side chains as well as alteration of the Zn coordination geometry to avoid the steric crowding between pendant

functionalities can lead to formation of an unexpected honeycomb-like structure rather than the preferred pillared-layer structure.<sup>4, 6</sup> These challenges associated with the production of a non-interpenetrated pillared-layer MCP emphasize a need for an alternative design strategy. Herein we report a strategy of symmetry breaking<sup>7-9</sup> at nodes in order to thwart interpenetration while preserving the pillared-layer structure. The strategy involves incorporation of two dicarboxylate linkers of differing lengths<sup>10</sup> with 4,4'-bipyridine in the presence of Zn(II) metal ion.<sup>11</sup> It was hypothesized that employing two different carboxylate linkers may avoid interpenetration by breaking the local fourfold symmetry<sup>1</sup> at the Zn paddlewheel nodes (Figure 1) by, for example, enabling the formation of a rectangular grid as opposed to the common square grid. Symmetry breaking at nodes can be explained if a low symmetry case is considered where m number of short and n number of long ditopic linkers are attached to a 4-connected Zn paddlewheel node (m+n=4) (Figure 3.1); this arrangement leads to a reduction of local symmetry at the node from fourfold to twofold or onefold depending on the m/n ratio and disposition of linkers. We envision that reduction of nodal symmetry originating from different linker arrangements may suppress the interpenetration of networks and serve as a complement to ligand-based symmetry breaking.<sup>7</sup>

### 3.2 Results and Discussion

In order to construct a layer composed of two dicarboxylate linkers, H<sub>2</sub>-BDC and 2,6-naphthalenedicarboxylic acid (H<sub>2</sub>-NDC), were chosen for initial study. Combining two linkers of different lengths with a 4-connected square Zn paddlewheel SBU yields six potential tilings (Figure 3.1) that upon self-repetition give rise to six forms (in parentheses): four BDC around a metal paddlewheel (Form 1), four NDC (Form 2), *trans*- two BDC: two NDC (Form 3), *cis*- two BDC: two NDC (Form 4), three BDC: one NDC (Form 5), and one BDC: three NDC (Form 6). The solvothermal reaction of a mixture of H<sub>2</sub>-BDC, H<sub>2</sub>-NDC with 4,4'-bipyridine (4,4'-bipy) in

a 1:1:1 molar ratio in the presence of Zn(II) resulted in a needle-shaped material, designated UMCM-15 (Section 3.4.1 and 3.4.2). UMCM-15 exhibits a distinct powder X-ray diffraction (PXRD) pattern in peak positions and intensities from those of  $[\text{Zn}_2(\text{BDC})_2(4,4'\text{-bipy})]_n$  and  $[\text{Zn}_2(\text{NDC})_2(4,4'\text{-bipy})]_n$ , two well-studied members of pillared-layer  $[\text{M}_2\text{L}_2\text{P}]_n$  family derived from a single carboxylate linker.<sup>2, 12</sup>  $^1\text{H}$  NMR spectroscopy experiments performed on acid digests of evacuated UMCM-15 indicate the presence of  $\text{H}_2\text{-BDC}$ ,  $\text{H}_2\text{-NDC}$ , and 4,4'-bipy in a ratio of  $\sim 1:3:2$  signaling a probable formation of Form 6 as described above (Section 3.4.3). Several attempts to grow single crystal of UMCM-15 suitable for single crystal structure determination were unsuccessful. Indexing the PXRD pattern of as-synthesized UMCM-15 revealed a unit cell with  $a = 18.629 \text{ \AA}$ ,  $b = 24.446 \text{ \AA}$ ,  $c = 14.020 \text{ \AA}$ ,  $\alpha = 90^\circ$ ,  $\beta = 135^\circ$ , and  $\gamma = 90^\circ$ . Based on the unit cell parameters and  $^1\text{H}$  NMR spectroscopic data a model of Form 6 was constructed and geometrically optimized with the Forcite module of Materials Studio Version 7. The calculated PXRD pattern was compared to the experimental one to find a good agreement confirming UMCM-15 is indeed Form 6. A Pawley refinement was performed to obtain the final unit cell parameters:  $a = 18.6749 \pm 0.0008 \text{ \AA}$ ,  $b = 24.3124 \pm 0.0009 \text{ \AA}$ ,  $c = 14.0068 \pm 0.0006 \text{ \AA}$ ,  $\alpha = 89.258 \pm 0.002^\circ$ ,  $\beta = 135.719 \pm 0.001^\circ$ , and  $\gamma = 90.789 \pm 0.002^\circ$  (final  $R_p$  2.80% and  $R_{wp}$  4.39%) (Section 3.4.4). UMCM-15 (Figure 3.2) consists of one BDC and three NDC linkers assembling around a Zn paddlewheel SBU to generate a 2D layer with two windows: a rectangular window of dimensions  $9.2 \times 7.5 \text{ \AA}^2$  and a square one of  $9.2 \times 9.2 \text{ \AA}^2$  (Figure 3.2b). The remaining axial positions of the metal SBU are occupied by 4,4'-bipy serving as pillars between adjacent layers of spacing  $7.4 \text{ \AA}$  (Figure 3.2a). Noteworthy, UMCM-15 is a coordination copolymer of three linkers incorporated into a framework, an addition to an extremely rare group of coordination terpolymers.<sup>13-15</sup> Production of UMCM-15 also illustrates

the power of the multilinker approach<sup>13-15</sup> as a tool of creating structural diversity in field of MCPs using commercial feedstocks.

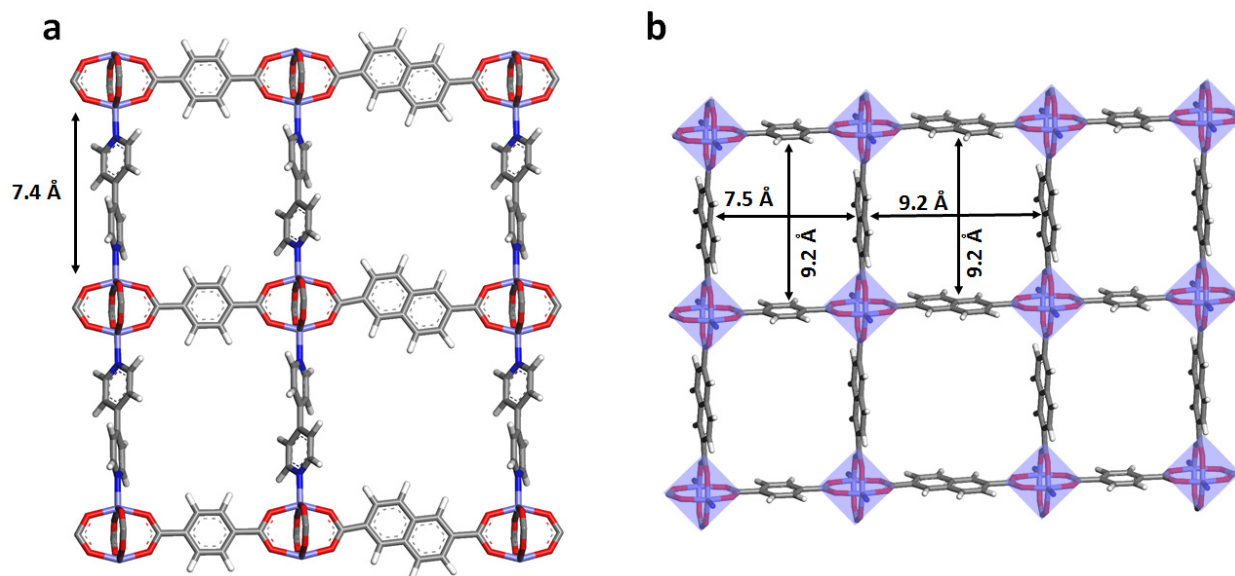


Figure 3. 2. a) Pillared-layer structure of UMCM-15 and b) layer arrangement of UMCM-15 showing a square and a rectangular pore window. Pore dimensions are measured with subtraction of the van der Waals radii of the atoms.

Utilization of the symmetry breaking strategy is envisioned to promote non-interpenetration of the framework. In order to test this notion, Nile red, a polycyclic organic dye was chosen which has a kinetic diameter (8.6 Å) comparable to the largest pore window of the non-interpenetrated model of UMCM-15. Here it must be noted that the pillared-layer MCPs derived from a single carboxylate linker,  $[\text{Zn}_2(\text{BDC})_2(4,4'\text{-bipy})]_n$  and  $[\text{Zn}_2(\text{NDC})_2(4,4'\text{-bipy})]_n$ , are two and three fold interpenetrated respectively. For comparison all three MCP crystals,  $[\text{Zn}_2(\text{BDC})_2(4,4'\text{-bipy})]_n$ ,  $[\text{Zn}_2(\text{NDC})_2(4,4'\text{-bipy})]_n$ , and UMCM-15, were immersed in dimethylformamide solution saturated with Nile red and containing additional solid dye at room temperature for one day. Nile red, possessing kinetic diameter larger than pore dimensions, cannot penetrate the pores of  $[\text{Zn}_2(\text{BDC})_2(4,4'\text{-bipy})]_n$  and  $[\text{Zn}_2(\text{NDC})_2(4,4'\text{-bipy})]_n$  (Figure 3.3). By contrast, the dye molecule enters the pores of UMCM-15 confirming the non-interpenetrated



nature of UMCM-15. From the standpoint of controlling the extent of interpenetration, there are various approaches to address this challenge such as installation of sterically bulky

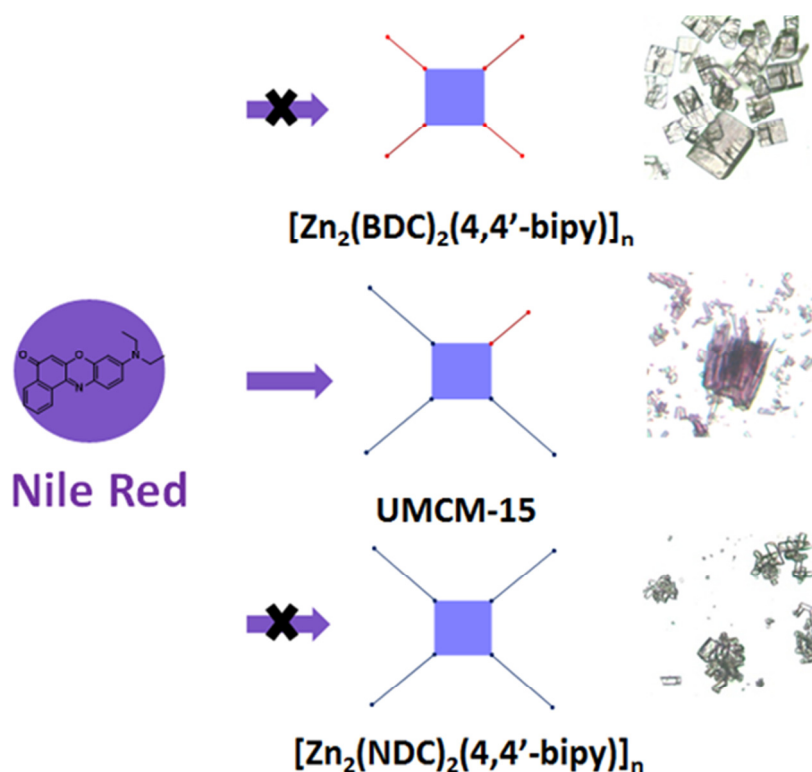


Figure 3. 3. Schematic of size exclusion results for Nile red incorporation into the pores of [Zn<sub>2</sub>(BDC)<sub>2</sub>(bipy)]<sub>n</sub>, [Zn<sub>2</sub>(NDC)<sub>2</sub>(bipy)]<sub>n</sub>, and UMCM-15. Nile red is represented in the purple sphere. The color of crystals indicate if dye is incorporated into corresponding MCP crystals.

functionalities on the organic linker,<sup>5, 16</sup> epitaxial growth,<sup>17, 18</sup> utilization of templates,<sup>19</sup> alteration of the reaction temperature and concentration,<sup>20, 21</sup> and use of reduced symmetry linkers<sup>7, 8, 22</sup> or non-self-dual nets.<sup>23</sup> However, the mechanism to avoid interpenetration in this study is fundamentally distinct and is an outcome of non-uniformity of distances between metal SBUs.<sup>10</sup> The overall network topology for [Zn<sub>2</sub>(BDC)<sub>2</sub>(4,4'-bipy)]<sub>n</sub>, [Zn<sub>2</sub>(NDC)<sub>2</sub>(4,4'-bipy)]<sub>n</sub>, and UMCM-15 is essentially same as *xah*<sup>24</sup> (standard presentation of the net is obtained from topological calculations performed in Topos<sup>25</sup>). However, the degree of interpenetration is not same in these MCPs which is believed to stem from different spacings between metal SBUs. In [Zn<sub>2</sub>(BDC)<sub>2</sub>(4,4'-bipy)]<sub>n</sub> and [Zn<sub>2</sub>(NDC)<sub>2</sub>(4,4'-bipy)]<sub>n</sub>, there exist a single distance between

metal SBUs in the layer which readily gives rise to a high symmetry network substructure.<sup>7</sup> However, UMCM-15 derived from two carboxylate linkers breaks the high nodal symmetry in the layer; this complexity ultimately eliminates the interpenetration. Note that these changes in local nodal symmetry are completely lost in a purely topological analysis.  $[\text{Zn}_2(\text{BDC})_2(4,4'\text{-bipy})]_n$ ,  $[\text{Zn}_2(\text{NDC})_2(4,4'\text{-bipy})]_n$ , and UMCM-15 all have the same *xah* net and yet behave very differently.

Given the fact that UMCM-15 is non-interpenetrated, a higher  $\text{N}_2$  uptake was expected than for MCPs derived from a single carboxylate linker. The  $\text{N}_2$  sorption isotherm of the

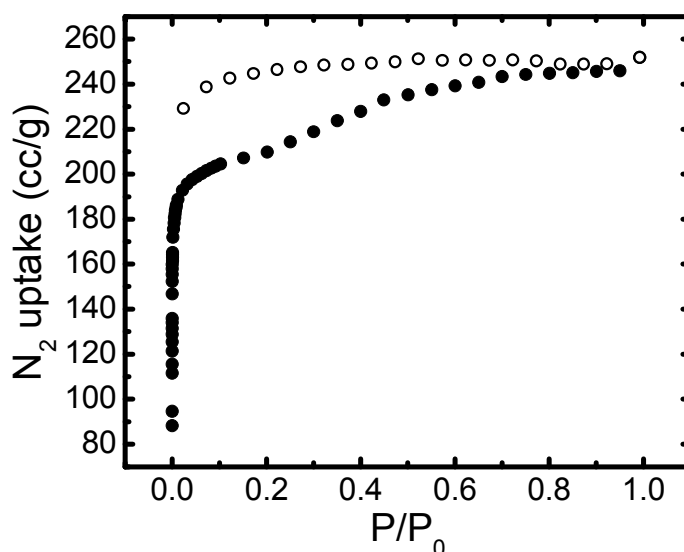


Figure 3. 4. Nitrogen sorption isotherm of activated UMCM-15 showing hysteresis.

activated material prepared by the flowing<sup>26</sup> supercritical  $\text{CO}_2$  activation<sup>27</sup> method shows hysteresis indicating a structural change upon activation and/or sorption experiments (Figure 3.4). Nevertheless, the BET surface area of UMCM-15 ( $810 \text{ m}^2/\text{g}$ ) is higher than that of  $[\text{Zn}_2(\text{BDC})_2(4,4'\text{-bipy})]_n$  ( $700 \text{ m}^2/\text{g}$ ) and  $[\text{Zn}_2(\text{NDC})_2(4,4'\text{-bipy})]_n$  (essentially non-porous) consistent with more void space in UMCM-15. The PXRD pattern of the material after

evacuation differs from the as-synthesized material indicating the flexible nature of UMCM-15. Notably the material regenerates the as-synthesized PXRD pattern upon re-soaking with the solvent of synthesis.

### 3.3 Conclusions

To conclude, breaking the nodal symmetry by incorporation of three linkers into a framework offers a largely unexploited approach to the production of porous materials lacking interpenetration. UMCM-15, a coordination terpolymer derived from two carboxylate linkers, 1,4-benzene dicarboxylate and 2,6-naphthalene dicarboxylate, in the layer and 4,4'-bipyridine pillars presents a powerful demonstration of this strategy. UMCM-15 is a non-interpenetrated MCP wherein its analogous pillared-layer MCPs derived from a single carboxylate linker are two- or three-fold interpenetrated. Employing two carboxylate linkers in the layer enabled formation of a non-regular layer arrangement with a rectangular grid structure as opposed to common square grids observed in pillared-layer coordination polymers. We also demonstrate here that the breaking the nodal symmetry in UMCM-15, although does not alter the overall network topology from its single carboxylate variants, reduces the interpenetration. Furthermore, utilization of commercially available linkers, in principle, allows use of a myriad of commercial ditopic linkers to generate a rich landscape of structurally diverse materials.

### 3.4 Experimental Section

#### 3.4.1 Synthesis of UMCM-15

H<sub>2</sub>-BDC (16.6 mg, 0.0999 mmol), H<sub>2</sub>-NDC (21.6 mg, 0.0999 mmol), 4,4'-bipy (15.6 mg, 0.0999 mmol) and Zn(NO<sub>3</sub>)<sub>2</sub>·6H<sub>2</sub>O (60.0 mg, 0.202 mmol) were dissolved in 9.0 mL of *N,N*-dimethylformamide. The mixture was sonicated for 30 min and the solution was clarified by filtration through a glass wool plug. The reaction mixture was heated to 85 °C. After 2 days,

needle-shaped crystals of a single phase were obtained. After cooling to room temperature, the product was isolated by decanting the mother liquor and washing with fresh DMF ( $3 \times 15$  mL). The yield of the reaction determined from the weight of the solvent-free material (18.0 mg) is 21.7% based on H<sub>2</sub>-BDC.

### 3.4.2 Morphology of UMCM-15

Optical images were taken with a Spot Insight Color camera fixed to a Leica DMIL microscope.

SEM image was collected on a Zeiss SEM-1455 VP instrument operating under 10 kV energy source in vacuum at a working distance of 5 mm.

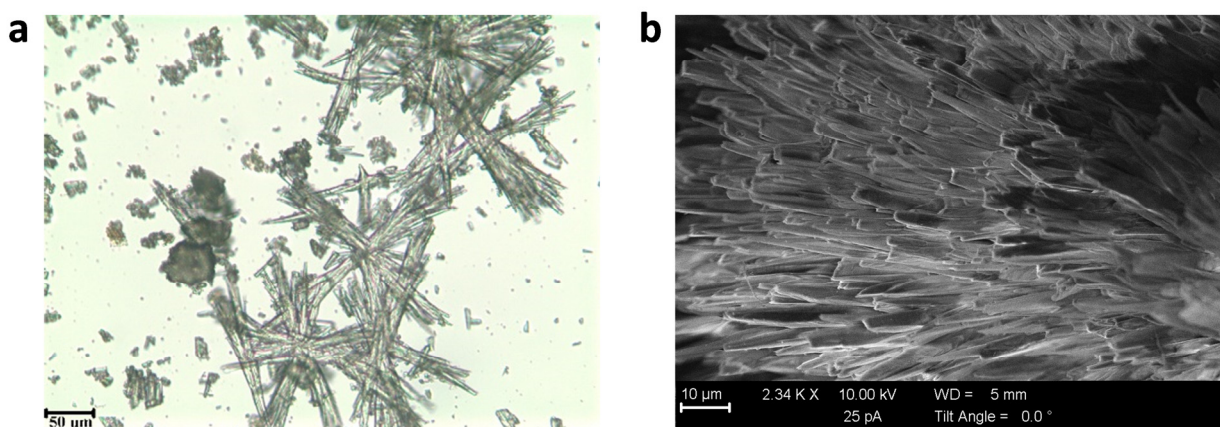


Figure 3. 5. a) Optical micrograph and b) scanning electron micrograph of UMCM-15.

### 3.4.3 $^1\text{H}$ NMR Spectroscopic Data of Digested UMCM-15

Solvent free materials were digested in 35 wt% DCl in  $\text{D}_2\text{O}$  and diluted with  $\text{DMSO-}d_6$  before performing  $^1\text{H}$  NMR spectroscopic experiments.

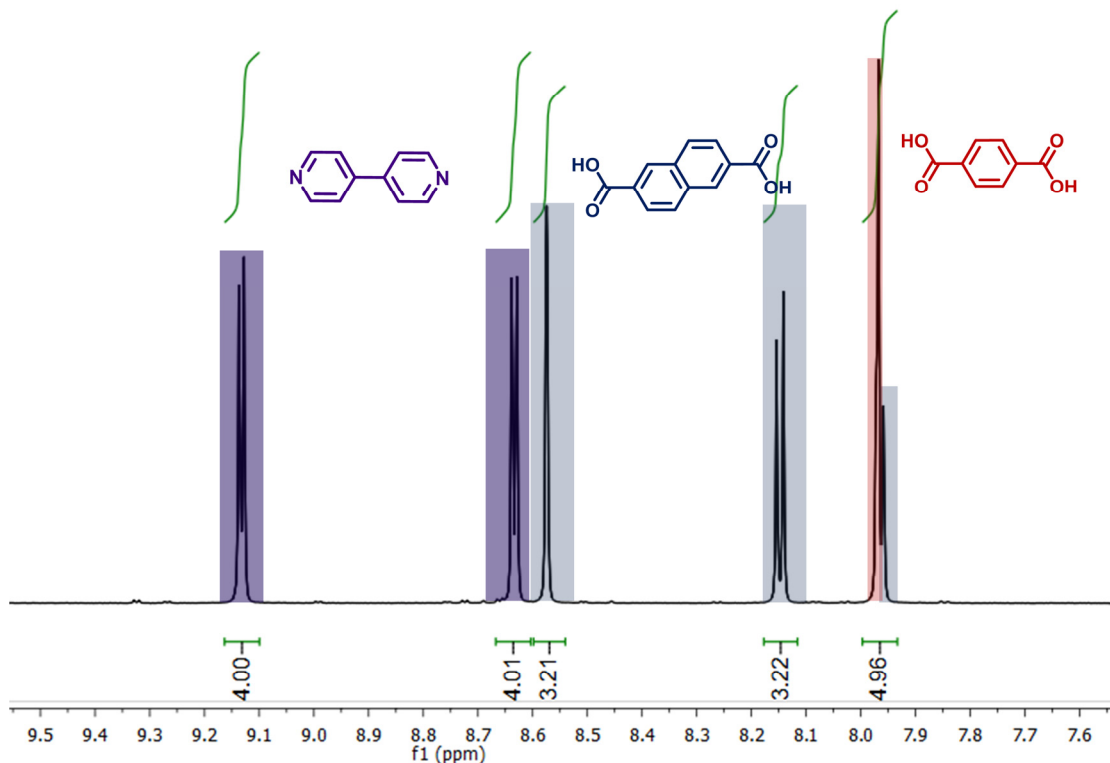


Figure 3. 6. Aromatic region of  $^1\text{H}$  NMR spectra for digested UMCM-15.

### 3.4.4 Structural Modelling and X-ray Diffraction Analyses

Powder X-ray diffraction data were collected on a Bruker D8 Advance Diffractometer having Bragg-Brentano geometry. The  $\text{CuK}\alpha$  radiation source was operated at 40 V and 40 mA. As-synthesized sample was ground and evenly dispersed on a low background quartz plate. The diffraction patterns were collected at a 0.5 sec/step scan rate.

Based on indexing results a model was constructed in the triclinic crystal system (space group 1) assembling the building units using Materials Studio 7 (Accelrys). A geometry optimization was performed applying the Forcite module using UFF forcefield. The convergence

conditions from coarse to ultra-fine were applied sequentially using default parameters. The simulated powder pattern was generated from the model structure and refined against the experimental data using a full pattern Pawley refinement. The Pawley refinement was applied to the model sequentially with specimen displacement, background, lattice parameters, and peak profile using Pseudo-Voigt function. The refinement was conducted sequentially with convergence quality from coarse to ultra-fine to give the final plot.

Table 3. 1. Pawley refinement results of UMCM-15

Sample name	Rwp	Rwp (without background)	Rp
UMCM-15	4.39%	4.91%	2.80%

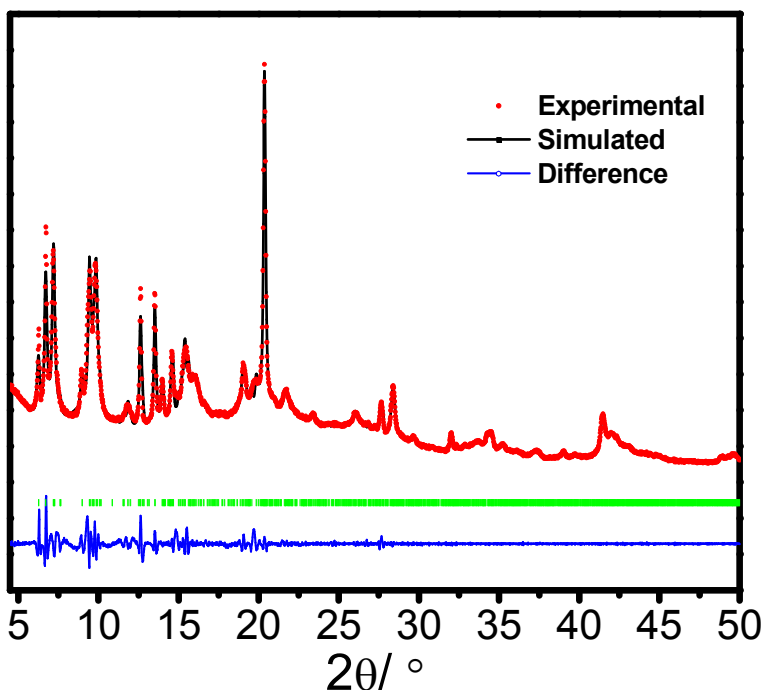


Figure 3. 7. Pawley refinement results from simulated and experimental powder X-ray diffraction pattern of UMCM-15.

Table 3. 2. Refined cell parameters and gemetrically optimized fractional atomic coordiantes of UMCM-15.

Space group: P1	$a = 18.6749 \pm 0.0008 \text{ \AA}$ , $b = 24.3124 \pm 0.0009 \text{ \AA}$ ,
-----------------	---

		$c = 14.0068 \pm 0.0006 \text{ \AA}$					
		$\alpha = 89.258 \pm 0.002^\circ, \beta = 135.719 \pm 0.001^\circ,$ $\gamma = 90.789 \pm 0.002^\circ$					
Atom	x	y	z	Atom	x	y	z
O1	-0.1141	0.57196	-0.0766	H84	0.47685	0.5894	0.26122
O2	0.60977	0.57352	0.64732	H85	0.28834	0.59137	0.04495
O3	0.7499	0.64754	0.78696	O86	0.77267	1.04568	0.63785
O4	0.75001	0.49708	0.78483	O87	0.7518	1.04123	0.77473
C5	0.75061	0.37492	0.78811	C88	0.7626	1.01641	0.70458
O6	0.63411	0.57745	0.51474	O89	0.6121	0.11835	0.63466
O7	-0.0901	0.57491	-0.2097	O90	-0.1121	0.11625	-0.0896
O8	0.76964	0.49981	0.6467	O91	0.75207	0.19353	0.77707
C9	0.7704	0.37719	0.63655	C92	0.75101	0.3161	0.78683
O10	0.77071	0.65215	0.65004	O93	-0.0877	0.11985	-0.2222
Zn11	0.74688	0.57205	0.81706	O94	0.63621	0.12093	0.50163
N12	0.74484	0.57092	0.95205	O95	0.77173	0.19618	0.63898
Zn13	0.77308	0.57615	0.61873	C96	0.77088	0.31837	0.63535
N14	0.7749	0.57613	1.48297	Zn97	0.74897	0.11724	0.8058
C15	-0.053	0.57308	-0.0897	N98	0.74723	0.11738	0.94145
C16	0.57278	0.57622	0.52756	Zn99	0.77525	0.12116	0.60752
C17	0.76002	0.67689	0.72037	N100	0.7774	0.12228	1.47244
C18	0.76028	0.40738	0.71301	C101	0.57504	0.11985	0.51471
C19	0.75994	0.47139	0.71482	C102	-0.0507	0.11748	-0.1024
C20	0.85822	0.59124	1.51014	C103	0.76121	0.28591	0.71045
C21	0.85494	0.59076	1.40652	C104	0.7617	0.22191	0.70885
C22	0.76453	0.57563	1.27339	C105	0.85549	0.09912	1.49598
C23	0.68026	0.56025	1.24879	C106	0.85138	0.09753	1.39178
C24	0.68755	0.56007	1.35541	C107	0.7651	0.11876	1.26138
C25	0.67012	0.59714	0.93153	C108	0.68608	0.14245	1.24034
C26	0.67469	0.59892	1.0361	C109	0.69438	0.14441	1.3479
C27	0.758	0.57455	1.16382	C110	0.66718	0.09802	0.91756
C28	0.83367	0.54778	1.18181	C111	0.67089	0.09831	1.02156
C29	0.82502	0.54594	1.0739	C112	0.75854	0.11766	1.15181
C30	0.75887	0.74078	0.72675	C113	0.83955	0.13732	1.17313
C31	0.76938	0.77772	0.65718	C114	0.83174	0.13749	1.066
C32	0.76758	0.83678	0.66683	H115	0.74272	0.29352	0.85024
C33	0.75517	0.86033	0.7465	H116	0.77945	0.2977	0.57092
C34	0.74482	0.824	0.81511	H117	0.92483	0.08085	1.6009
C35	0.74661	0.76608	0.80544	H118	0.91801	0.07901	1.41306
C36	0.75336	0.9194	0.75612	H119	0.61511	0.1601	1.13562

C37	0.76387	0.95632	0.68652	H120	0.63053	0.16485	1.33032
C38	0.77614	0.93101	0.60787	H121	0.59665	0.08146	0.8127
C39	0.77796	0.87309	0.59823	H122	0.60291	0.08288	1.00024
C40	0.13568	0.1236	0.01261	H123	0.91171	0.15315	1.27779
C41	0.24296	0.12248	0.13616	H124	0.89729	0.15475	1.08389
C42	0.27699	0.11985	0.26449	C125	0.05827	0.57771	0.02736
C43	0.20265	0.11803	0.2665	C126	0.06052	0.12192	0.01472
C44	0.09715	0.1189	0.14468	O127	0.77664	0.66706	0.74234
C45	0.38428	0.11899	0.38806	O128	0.77293	0.6606	0.69031
C46	0.45942	0.12054	0.38589	O129	0.76922	0.65414	0.63828
C47	0.4228	0.12282	0.25591	O134	0.7237	0.2819	0.8662
C48	0.31729	0.12388	0.1341	O137	0.6458	0.4105	0.6968
H49	0.74212	0.39559	0.85262	O141	0.1678	0.525	0.3106
H50	0.77855	0.39977	0.57298	O143	0.8286	0.3337	0.6386
H51	0.93121	0.60439	1.61748	O144	0.4199	0.5418	0.5577
H52	0.92553	0.60263	1.43052	O1	0.88589	0.57196	0.92344
H53	0.60576	0.5479	1.14176	O7	0.90988	0.57491	0.79027
H54	0.61903	0.54621	1.33447	Zn11	-0.2531	0.57205	-0.1829
H55	0.60321	0.61785	0.82882	Zn13	-0.2269	0.57615	-0.3813
H56	0.61082	0.62014	1.01733	Zn13	0.77308	0.57615	1.61873
H57	0.90218	0.52753	1.2843	N14	0.7749	0.57613	0.48297
H58	0.88613	0.52318	1.08893	O86	0.77267	0.04568	0.63785
H59	0.77941	0.75917	0.59257	O87	0.7518	0.04123	0.77473
H60	0.73464	0.84094	0.88075	O90	0.88794	0.11625	0.91042
H61	0.73799	0.73802	0.86234	O93	0.91227	0.11985	0.77778
H62	0.74316	0.93629	0.82176	Zn97	-0.251	0.11724	-0.1942
H63	0.78506	0.95734	0.54914	Zn97	0.74897	1.11724	0.8058
H64	0.78803	0.85464	0.53358	Zn99	-0.2248	0.12116	-0.3925
H65	0.10881	0.12588	-0.0905	Zn99	0.77525	0.12116	1.60752
H66	0.22727	0.11581	0.36817	Zn99	0.77525	1.12116	0.60752
H67	0.03839	0.11713	0.14907	N100	0.7774	0.12228	0.47244
H68	0.40896	0.11702	0.48978	O130	0.92	0.2849	0.2927
H69	0.47923	0.12387	0.24734	O131	0.9773	0.8826	0.2515
H70	0.29068	0.12591	0.0311	O132	0.4291	0.0551	0.7365
C71	0.13339	0.58229	0.02556	O133	0.2122	0.4151	0.6625
C72	0.24067	0.5811	0.14915	O135	0.935	0.8687	0.3341
C73	0.27473	0.5749	0.27708	O136	0.628	0.2145	0.8273
C74	0.20041	0.57039	0.27875	O138	0.6329	0.0762	0.278
C75	0.09489	0.57192	0.15698	O139	0.433	0.9418	0.2766
C76	0.38203	0.57336	0.40061	O140	0.736	0.0197	0.0017



C77	0.45715	0.57812	0.39884	O142	0.4793	0.3775	0.9507
C78	0.42047	0.58483	0.26937	O145	0.0874	0.7426	0.5426
C79	0.31497	0.58614	0.14756	O146	0.5028	0.12	0.9996
H80	0.10653	0.58701	-0.0773	O147	0.3298	0.256	0.3358
H81	0.22504	0.56538	0.38009	O148	0.8968	0.208	0.5272
H82	0.03614	0.56843	0.16114	O149	0.9383	0.301	0.8202
H83	0.40673	0.56819	0.50196				

### 3.4.5 Nile Red Diffusion Experiments

MCP crystals were immersed in dimethylformamide (DMF) solution saturated with dye and containing additional solid dye solution at room temperature for 1 day and then washed with fresh DMF five times followed by immersion in mineral oil. Optical micrographs of crystals after dye impregnation were taken with a Spot Flex camera fixed to a Leica DMLP microscope. In each case, the crystals were sectioned to confirm if dye had penetrated to the centers of the crystals rather being confined to the outer surface.

### 3.4.6. TGA Trace of UMCM-15

Thermogravimetric analyses were performed on a TA Q50 equipment. Samples were

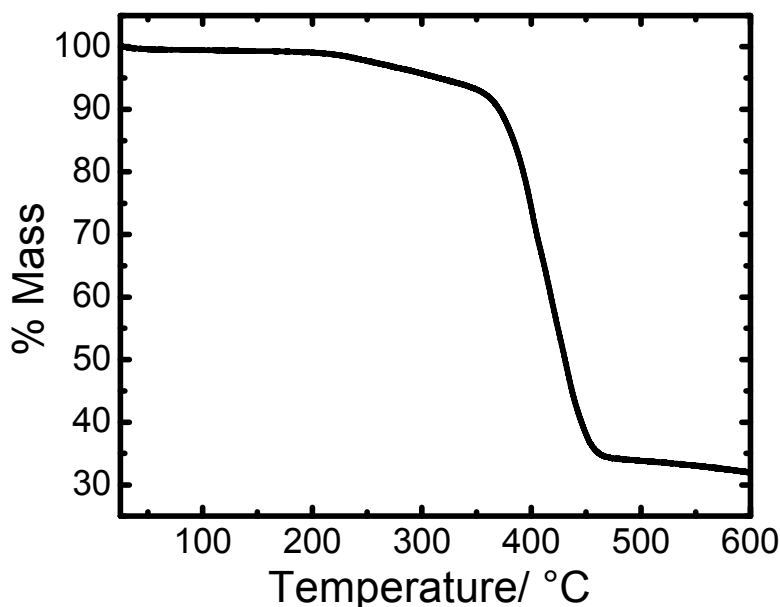


Figure 3. 8. TGA trace of activated UMCM-15.

activated before experiments. The temperature was ramped from 25 °C to 600 °C with a rate of 2 °C/ min under a flow of N<sub>2</sub> gas.

### 3.4.7 Activation of UMCM-15 and Gas Sorption Experiments

All materials were exchanged in fresh DMF for 24 hr before flowing supercritical CO<sub>2</sub> activation.<sup>28</sup>

N<sub>2</sub> adsorption/desorption isotherms were measured volumetrically at 77K in the range of  $1.00 \times 10^{-5} \leq P/P_0 \leq 1.00$  with an Autosorb-1C outfitted with the micropore option by Quantachrome Instruments (Boyton Beach, Florida, U.S.A.) running version 1.2 of the ASwin software package. Ultra-high purity He (99.999%, for void volume determination) and N<sub>2</sub> (99.999%) were purchased from Cryogenic Gases and used as received.

### 3.5 References

1. D. N. Dybtsev, H. Chun and K. Kim, *Angew. Chem. Int. Ed.*, 2004, **43**, 5033-5036.
2. H. Chun, D. N. Dybtsev, H. Kim and K. Kim, *Chem. Eur. J.*, 2005, **11**, 3521-3529.
3. S. Henke, A. Schneemann, A. Wütscher and R. A. Fischer, *J. Am. Chem. Soc.*, 2012, **134**, 9464-9474.
4. S. Henke, R. Schmid, J.-D. Grunwaldt and R. A. Fischer, *Chem. Eur. J.*, 10, **16**, 14296-14306.
5. T.-H. Park, K. Koh, A. G. Wong-Foy and A. J. Matzger, *Cryst. Growth Des.*, 2011, **11**, 2059-2063.
6. S. Henke and R. A. Fischer, *J. Am. Chem. Soc.*, 2011, **133**, 2064-2067.
7. J. K. Schnobrich, O. Lebel, K. A. Cychosz, A. Dailly, A. G. Wong-Foy and A. J. Matzger, *J. Am. Chem. Soc.*, 2010, **132**, 13941-13948.
8. Y. Xie, H. Yang, Z. U. Wang, Y. Liu, H.-C. Zhou and J.-R. Li, *Chem. Commun.*, 2014, **50**, 563-565.
9. L. Qin, J.-S. Hu, Y.-Z. Li and H.-G. Zheng, *Cryst. Growth Des.*, 2011, **11**, 3115-3121.
10. K. Koh, J. D. Van Oosterhout, S. Roy, A. G. Wong-Foy and A. J. Matzger, *Chem. Sci.*, 2012, **3**, 2429-2432.
11. In this context it should be noted that two differentially functionalized BDC linkers have been employed to increase the structural complexity in pillared-layer MOFs (see reference 3). However, mixing two linkers of differing lengths to construct a pillared-layer MCP is without precedent.
12. B. Chen, C. Liang, J. Yang, D. S. Contreras, Y. L. Clancy, E. B. Lobkovsky, O. M. Yaghi and S. Dai, *Angew. Chem. Int. Ed.*, 2006, **45**, 1390-1393.
13. A. Dutta, A. G. Wong-Foy and A. J. Matzger, *Chem. Sci.*, 2014, **5**, 3729-3734.

14. L. Liu, K. Konstas, M. R. Hill and S. G. Telfer, *J. Am. Chem. Soc.*, 2013, **135**, 17731-17734.
15. L. Liu and S. G. Telfer, *J. Am. Chem. Soc.*, 2015, **137**, 3901-3909.
16. O. K. Farha, C. D. Malliakas, M. G. Kanatzidis and J. T. Hupp, *J. Am. Chem. Soc.*, 2010, **132**, 950-952.
17. O. Shekhah, H. Wang, M. Paradinas, C. Ocal, B. Schupbach, A. Terfort, D. Zacher, R. A. Fischer and C. Woll, *Nat. Mater.*, 2009, **8**, 481-484.
18. D. Zacher, K. Yussenko, A. Bétard, S. Henke, M. Molon, T. Lahnorg, O. Shekhah, B. Schüpbach, T. de los Arcos, M. Krasnopolski, M. Meilikhov, J. Winter, A. Terfort, C. Wöll and R. A. Fischer, *Chem. Eur. J.*, 2011, **17**, 1448-1455.
19. S. Ma, D. Sun, M. Ambrogio, J. A. Fillinger, S. Parkin and H.-C. Zhou, *J. Am. Chem. Soc.*, 2007, **129**, 1858-1859.
20. J. Zhang, L. Wojtas, R. W. Larsen, M. Eddaoudi and M. J. Zaworotko, *J. Am. Chem. Soc.*, 2009, **131**, 17040-17041.
21. J. I. Feldblyum, A. G. Wong-Foy and A. J. Matzger, *Chem. Commun.*, 2012, **48**, 9828-9830.
22. W. Lu, Z. Wei, Z.-Y. Gu, T.-F. Liu, J. Park, J. Park, J. Tian, M. Zhang, Q. Zhang, T. Gentle Iii, M. Bosch and H.-C. Zhou, *Chem. Soc. Rev.*, 2014, **43**, 5561-5593.
23. H. K. Chae, D. Y. Siberio-Perez, J. Kim, Y. Go, M. Eddaoudi, A. J. Matzger, M. O'Keeffe and O. M. Yaghi, *Nature*, 2004, **427**, 523-527.
24. In a standard representation, linkers are simplified in their centers and zero-, one-, and two coordinated nodes are removed. The topology of these pillared-layer structures is revealed to be a **xah** using the standard representation. On the other hand, in cluster presentation the clusters are simplified as points in their centers and zero-, one-, and two coordinated nodes are removed. The net is **pcu  $\alpha$ -Po** in cluster presentation.
25. a) V. A. Blatov, *Int. Union Crystallogr. Comm. Crystallogr. Comput. Newsl.*, 2006, **7**, 4-8. b) E. V. Alexandrov, V. A. Blatov, A. V. Kochetkov and D. M. Proserpio, *CrystEngComm*, 2011, **13**, 3947-3958.
26. B. Liu, A. G. Wong-Foy and A. J. Matzger, *Chem. Commun.*, 2013, **49**, 1419-1421.
27. A. P. Nelson, O. K. Farha, K. L. Mulfort and J. T. Hupp, *J. Am. Chem. Soc.*, 2009, **131**, 458-460.

## Chapter 4

### **Porous Solids Arising from Synergistic and Competing Modes of Assembly: Combining Coordination Chemistry and Covalent Bond Formation**

Published: A. Dutta, K. Koh, A. G. Wong-Foy, A. J. Matzger, *Angew. Chem. Int. Ed.*, 2015, **54**,  
3983-3987.

#### **4.1 Introduction**

In past two decades the field of porous materials has witnessed rapid advances in the ability to create defined sorbents with exceptional and tunable properties. Two key materials classes contributing to this change are a) coordination polymers possessing micro and/or mesoporosity, often termed metal-organic frameworks (MOFs)<sup>1</sup> and b) organic polymers wherein directional covalent bonding is exploited to define a porous network as exemplified by covalent organic frameworks (COFs).<sup>2</sup> Though the details of the assembly processes associated with the production of these two classes of materials are significantly different, reversibility of bond formation is critical for yielding crystalline porous solids. Specifically for coordination polymers, slow decomposition of amide solvent liberating free amine (thus changing the pH of reaction mixture) drives the reversible acid-base reaction between the conjugate base of the linker and metal ions leading to the assembly of the framework.<sup>3</sup> On the other hand, formation of covalent organic frameworks is generally facilitated by reversible coupling between reactive groups installed on organic cores such as boroxine,<sup>2</sup> borazine,<sup>4</sup> azodioxy,<sup>5</sup> imine/enamine,<sup>6</sup> or

hydrazone<sup>7</sup> linkage formation. Despite the fact that much research has been focused on these two material classes individually, design and synthesis of extended frameworks employing both reversible coordination processes and reversible covalent bond formation is without precedent.<sup>8</sup> Here we investigate a system where both coordination processes and covalent bond formation occur and examine the outcome of the competitive processes in order to understand the factors influencing each mode of assembly. We also demonstrate that this approach enables access to multiple phases from a set of commercially available or readily accessible reagents.

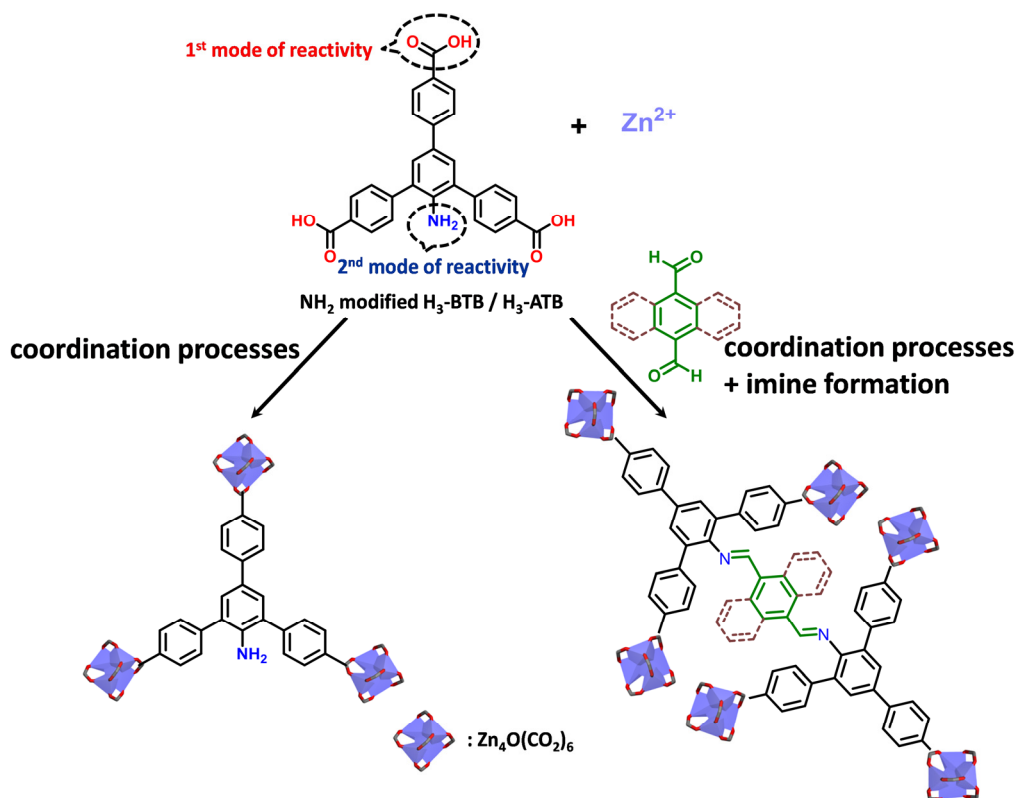


Figure 4. 1. Conceptual representation of different materials generated from coordination processes only and combination of coordination processes and imine formation.

## 4.2 Results and Discussion

A derivative of the widely used linker 1,3,5-tris(4-carboxyphenyl)benzene ( $\text{H}_3\text{-BTB}$ )<sup>9</sup> was chosen for this study where the central benzene ring was modified with a second site of

reactivity: a primary amino group (Figure 4.1). This functionality provides an opportunity for imine formation to take place upon reaction with a carbonyl group. It should be noted that the reaction between a carbonyl moiety and an amino group is one of the reactions successfully employed for the synthesis of crystalline COFs.<sup>6a</sup> The reaction of the modified H<sub>3</sub>-BTB (hereafter 2,4,6-tris(4-carboxyphenyl)aniline or H<sub>3</sub>-ATB) with Zn(II) at 85 °C results in the formation of colorless block-shaped crystals after 20 hr (Section 4.4.1). The powder X-ray

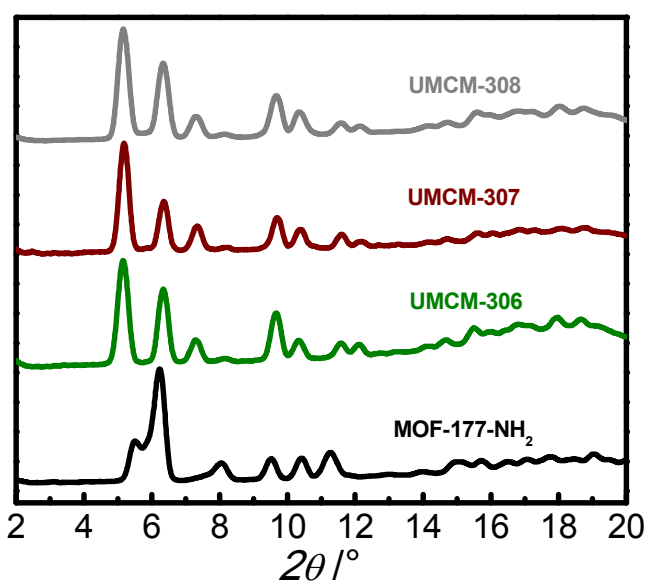


Figure 4. 2. PXRD patterns of MOF-177-NH<sub>2</sub> (black), UCMCM-306 (green), UCMCM-307 (red), and UCMCM-308 (grey).

diffraction pattern of this material (Figure 4.2) corresponds closely to that of MOF-177<sup>9</sup> (Section 4.4.2) and so this material is termed MOF-177-NH<sub>2</sub>. This finding is significant in light of the numerous other phases possible for a combination of BTB and Zn(II).<sup>10</sup>

The effect of addition of terephthalaldehyde, a dialdehyde with a *para* disposition of functional groups, on the assembly of MOF-177-NH<sub>2</sub> was next examined (Figure 4.1). Three potential outcomes were expected as a consequence of the dialdehyde addition: a) formation of

MOF-177-NH<sub>2</sub> with or without dangling aldehyde residues b) generation of a novel phase resulting from combination of coordination processes and imine formation and/or c) formation of a different phase derived solely from H<sub>3</sub>-ATB. The solvothermal reaction of H<sub>3</sub>-ATB and terephthalaldehyde in a 1:1.5 molar ratio in the presence of Zn(II) results in a yellow colored rod-shaped material designated UMCM-306 (Section 4.4.1). The powder X-ray diffraction pattern of this material exhibits distinct peak positions and intensities as compared to those of MOF-177-NH<sub>2</sub> (Figure 4.2). <sup>1</sup>H NMR spectroscopy experiments performed on acid digests of evacuated UMCM-306 indicate the presence of terephthalaldehyde and H<sub>3</sub>-ATB in the ratio of 1:2.8 (Section 4.4.4). This finding in combination with the unique PXRD pattern signals the probable occurrence of case (b). Unambiguous confirmation of structure of UMCM-306, obtained from a single crystal X-ray diffraction study (Section 4.4.3), revealed that the structure dramatically differs from the structure of MOF-177-NH<sub>2</sub>. The product crystallizes in the space group *P4<sub>2</sub>/mnm* and the framework consists of octahedral Zn<sub>4</sub>O(O<sub>2</sub>CR)<sub>6</sub> secondary building units (SBUs) linked together by two ATB linkers condensed with a single terephthalaldehyde residue (Figure 3b). Condensation of two primary amino groups from ATB linkers with one terephthalaldehyde molecule gives rise to two covalent imine linkages, which effectively provides a hexatopic linker coordinated to tetrahedral Zn<sub>4</sub>O metal clusters. However, it should be noted that the occurrence of the di-imine linkage in the structure is ~70% complete as indicated by the <sup>1</sup>H NMR spectroscopy results and supported by the single X-ray diffraction data suggesting that the imine formation is not complete in this case. For additional structural confirmation, especially to further confirm the presence of imine linkages, Raman spectroscopy was also employed. Comparison of the Raman spectrum of UMCM-306 with that of MOF-177-NH<sub>2</sub> (Section 4.4.5) reveals differences especially in two primary wavenumber regions: 3300-3500

$\text{cm}^{-1}$  and  $1500\text{-}1800\text{ cm}^{-1}$ . UMCM-306 shows no detectable peak at the former region whereas MOF-177- $\text{NH}_2$  exhibits a peak at  $3398\text{ cm}^{-1}$  attributable to  $\text{NH}_2$  stretching. Moreover, the emergence of a peak at  $1634\text{ cm}^{-1}$  in UMCM-306 can be ascribed to the formation of a new

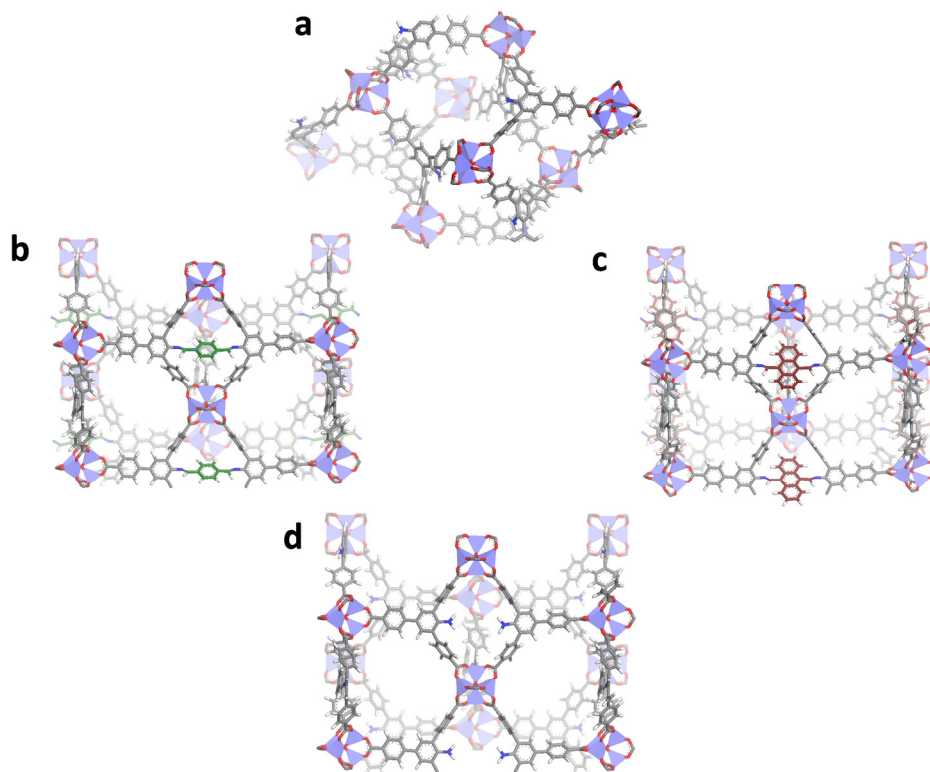


Figure 4. 3. Structures of materials: a) MOF-177- $\text{NH}_2$ , b) UMCM-306, c) UMCM-307, and d) UMCM-308. (a, c, and d are generated from the models and validated by powder X-ray diffraction data; b is obtained from single X-ray diffraction data).

imine linkage in UMCM-306 which is absent in MOF-177- $\text{NH}_2$ .

Given the fact that both coordination processes between the carboxylates and metal ions as well as covalent imine bond formation occur in the assembly of UMCM-306, the system was selected as a platform for investigating the competition between coordination processes and imine formation. We hypothesized that a major contributor influencing this competition would be the relative rate of imine formation vs coordination processes which can be affected by different variables including the incubation time of amino functionalized linker and the



dialdehyde as well as the extent of solvent decomposition/base formation within the reaction mixture. To determine if the incubation time of the two organic components plays a role in phase selection, a series of experiments were conducted with timed addition of terephthalaldehyde. The dialdehyde was added after various delay times (delay time  $t = 1, 6, 9, 12, 15, 16, 18, 19, 20, 24$  hr) into the homogenous reaction mixture (in cases of  $t = 1, 6, 9, 12, 15, 16,$  and  $18$  hr) or heterogeneous reaction mixture (in cases of  $t = 19, 20, 24$  hr) containing H<sub>3</sub>-ATB and Zn(NO<sub>3</sub>)<sub>2</sub>·6H<sub>2</sub>O at 85 °C and all reactions mixtures were analyzed after 30 hr. Two morphologically different phases were observed: rod-shaped UMCM-306 at early delay times and primarily block-shaped MOF-177-NH<sub>2</sub> at late stages of addition (Figure 4.4) indicating that the incubation time of the two organic components is critical in dictating the outcome of the

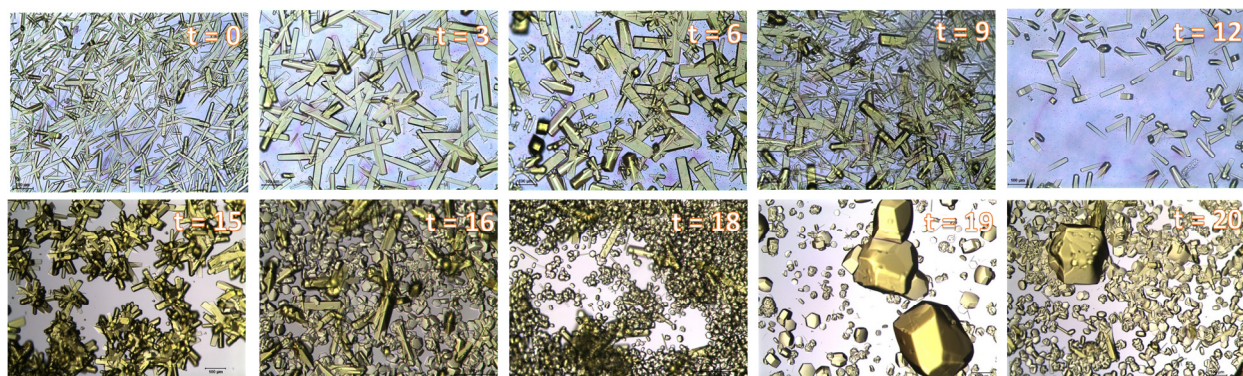


Figure 4. 4. Optical micrographs of UMCM-306 and MOF-177-NH<sub>2</sub> at different delay times ( $t$  in hr) of terephthalaldehyde addition.

competition. However, the appearance of MOF-177-NH<sub>2</sub> upon delayed addition of dialdehyde in homogenous reaction mixtures ( $18 \geq t \geq 16$ ) may be a consequence of the extent of solvent decomposition/base formation upon extended reaction rather than only a result of short incubation time of the two organic components. To investigate the role of solvent decomposition/base formation on the competition of the two processes, a series of solutions containing Zn(NO<sub>3</sub>)<sub>2</sub>·6H<sub>2</sub>O in *N,N*-dimethylformamide (DMF) were prepared and pre-heated at

85 °C for 1, 2, 4, 8, 16, and 17 hours prior to addition of the organic components. The preheated solutions for 1, 2, 4, and 8 hr lead to formation of UMCM-306 whereas the ones heated for 16 and 17 hr afford primarily MOF-177-NH<sub>2</sub> crystals (Section 4.4.6). These observations demonstrate that the duration of the aging of Zn(NO<sub>3</sub>)<sub>2</sub>·6H<sub>2</sub>O and DMF also controls the competition between the coordination processes and imine formation presumably *via* tuning the extent of solvent decomposition/base formation. For the solutions preheated for relatively short times, imine formation outperforms coordination processes resulting in formation of UMCM-306, whereas coordination processes competes with the imine formation in cases of preheated solutions for longer times leading to MOF-177-NH<sub>2</sub>.<sup>11</sup>

To explore the generality of the approach of combining coordination polymerization with covalent imine bond formation and its potential to accommodate a diversity of aldehyde partners, a bulkier dialdehyde, anthracene-9,10-dialdehyde was chosen. The solvothermal reaction of H<sub>3</sub>-ATB and anthracene-9,10-dialdehyde with Zn(II) yields orange colored rod-shaped crystals designated UMCM-307. Comparison of powder X-ray diffraction patterns of this material with UMCM-306 reveals nearly identical peak positions and intensities of the two materials confirming their isostructural nature (Figure 4.2 and 4.3). <sup>1</sup>H NMR spectroscopy experiments performed on acid digests of evacuated UMCM-307 show the presence of anthracene-9,10-dialdehyde and H<sub>3</sub>-ATB in a 1:3.8 ratio. This result is consistent with the generation of the desired motif arising from both coordination processes and imine formation with the di-imine formation efficiency of ~50% (Section 4.4.4).

To further extend the above strategy to another class of carbonyl compounds, a diketone, 1,4-diacetylbenzene, was employed to react with H<sub>3</sub>-ATB and Zn(II) under solvothermal conditions.<sup>12</sup> The reaction affords colorless rod-shaped crystals designated UMCM-308. This

material exhibits a powder X-ray diffraction pattern closely matching with those of UMCM-306 and -307 suggesting the isostructural nature of all these materials (Figure 4.2). However, the  $^1\text{H}$  NMR spectrum obtained after acid digestion of evacuated UMCM-308 shows the presence of only  $\text{H}_3\text{-ATB}$  indicating that the organic part of the framework exclusively consists of the ATB linker without incorporation of the diketone residue (Section 4.4.4); this observation demonstrates the formation of a different phase derived solely from  $\text{H}_3\text{-ATB}$  (case c described above in the introduction). Moreover, the Raman spectrum possesses a peak at  $3390\text{ cm}^{-1}$  assigned to  $\text{NH}_2$  stretching and also very similar features in the  $1500\text{-}1800\text{ cm}^{-1}$  wavenumber region as  $\text{MOF-177-NH}_2$  (Section 4.4.5). These results confirm that UMCM-308 is a polymorphic framework<sup>10,13</sup> of  $\text{MOF-177-NH}_2$  (Figure 4.3). In other words,  $\text{MOF-177-NH}_2$  and UMCM-308 are composed of an identical SBU and linker but differ in net topology and pore structure. This finding highlights that a combination of a SBU and a linker can assemble in more than one arrangement in principle yet in practice only a few phases can be obtained depending on reaction parameters. For example,  $\text{Zn}_4\text{O}(\text{O}_2\text{CR})_6$  with the BTB linker has been reported to yield three MOFs possessing different net topologies:  $\text{MOF-177}$  (*qom*),  $\text{Zn/BTB}$  (*ant*), and  $\text{Zn/BTB}$  (*tsx*).<sup>10</sup> Surprisingly, UMCM-308, derived from  $\text{Zn}_4\text{O}(\text{O}_2\text{CR})_6$  with amino modified BTB linker, adopts an *rtl*<sup>14</sup> net distinct from these three MOFs (Figure 4.5). The difference between these nets originates from the linker orientations in the 2<sup>nd</sup> or 3<sup>rd</sup> coordination sphere (CS) connecting the trigonal and octahedral nodes. Despite the same CS1 in these nets, wherein each tritopic linker is connected to 3 octahedral SBUs and each octahedron is attached to 6 tritopic linkers, CS2 and/or CS3 are different; this outcome stems from the various orientations of linkers about the octahedral SBU in CS1 (Figure 4.5). The diketone acts as a phase-directing agent<sup>15</sup> favoring the *rtl* net. This finding prompted us to examine if the interaction of the amino group on  $\text{H}_3\text{-ATB}$

with an aromatic monoaldehyde/monoketone is adequate to direct a phase like UMCM-306 or -308, perhaps through torsion angle change induced in the ATB linker. Solvothermal reaction of

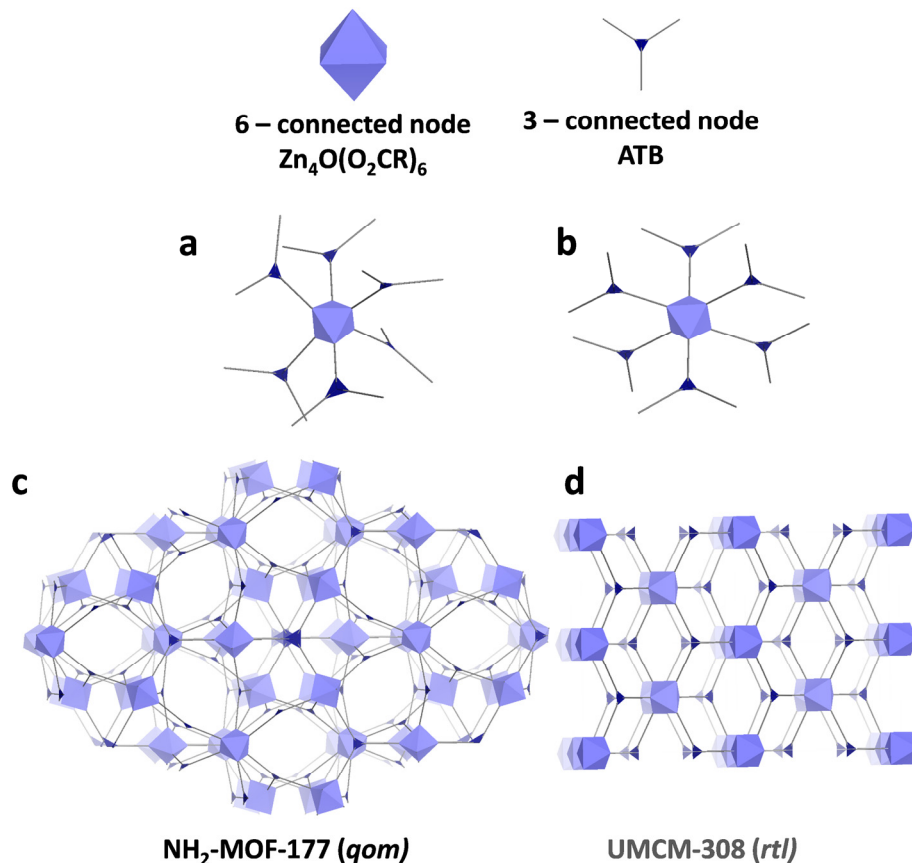


Figure 4. 5. Comparison of the linker orientations in CS1 (a and b) and underlying network topologies (c and d) of two polymorphic frameworks NH<sub>2</sub>-MOF-177 and UMCM-308 constructed from same 6-connected and 3-connected nodes.

H<sub>3</sub>-ATB with Zn(II) was carried out in presence of benzaldehyde or acetophenone to yield materials exhibiting nearly identical PXRD patterns as MOF-177-NH<sub>2</sub>. This fact verifies that presence of two carbonyl moieties in *para* positions of the carbonyl partner is critical for production of UMCM-306 or related phases suggesting a role, no matter how transient, of linking two amino modified BTB linkers covalently.

The N<sub>2</sub>-sorption studies of activated materials show high N<sub>2</sub> uptakes (Figure 4.6). N<sub>2</sub>-sorption isotherms of all these porous solids can be classified as Type I with a sharp uptake below P/P<sub>0</sub> = 0.05. Applying the BET model over the proper ranges<sup>16</sup> of the isotherms yields BET surface areas as follows: 4631 m<sup>2</sup>/g for MOF-177-NH<sub>2</sub>, 2820 m<sup>2</sup>/g for UMCM-306, 2520 m<sup>2</sup>/g for UMCM-307, and 1190 m<sup>2</sup>/g for UMCM-308. The surface area of UMCM-308 is significantly lower than the predicted one which is indicative of structural change of the material upon

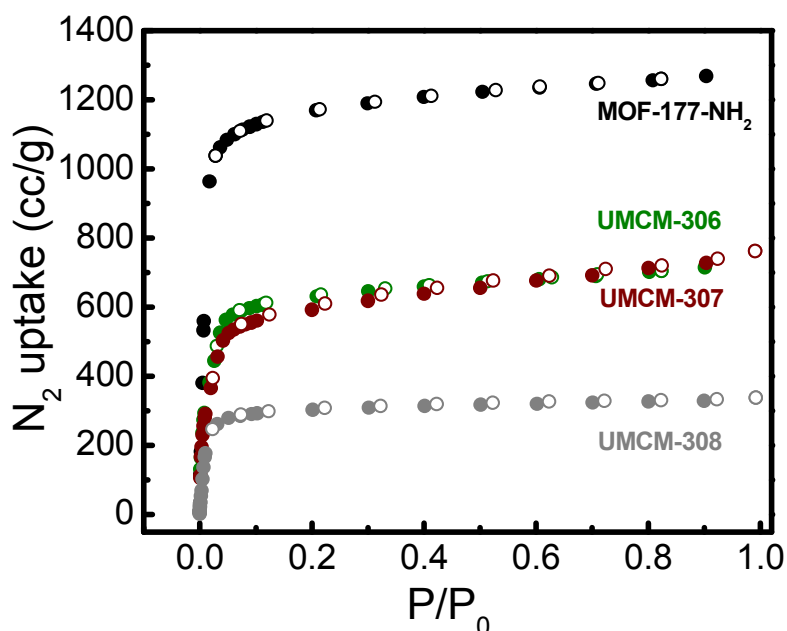


Figure 4. 6. Nitrogen sorption isotherms for MOF-177-NH<sub>2</sub> (black), UMCM-306 (green), and UMCM-307 (red).

activation as judged by PXRD (Section 4.4.1). Notably, the surface areas of the materials resulting from both coordination processes and imine formation are higher than those of COF-42, -43<sup>6a</sup> or -300<sup>7</sup> wherein imine formation alone is exploited for materials synthesis.

### 4.3 Conclusions

To conclude, employing coordination processes in tandem with imine formation presents a link between two orthogonal classes of porous materials as exemplified by metal-organic frameworks (MOFs) and covalent organic frameworks (COFs). This approach of combining two

different linkage modes in a single material, in addition to be a compelling materials discovery method, offers a platform for developing fundamental understanding of factors influencing competing modes of assembly. The incubation time of the organic components as well as the extent of solvent decomposition/base formation have been identified as key parameters in governing the competition between coordination processes and imine formation. Moreover, even temporary formation of reversible connections between components may be leveraged to make new phases. It was found that using a diketone in place of a dialdehyde unit leads to formation of a polymorphic framework of MOF-177-NH<sub>2</sub> wherein the assembly of octahedral Zn<sub>4</sub>O(O<sub>2</sub>CR)<sub>6</sub> with triangular ATB nodes gives rise to a *rtl* net without incorporation of a dicarbonyl compound. This network topology is otherwise unavailable from functionalized/non-functionalized BTB linker and Zn(II). There is ongoing work based on an array of commercially available or readily accessible multifunctional aldehydes and amine functionalized carboxylate linkers that can be combined using the described approach with the potential of providing a rich landscape of structurally complex materials derived from simple feedstocks.

## 4.4 Experimental Section

### 4.4.1 Synthesis of Materials

#### *Preparation of H<sub>3</sub>-ATB:*

2,4,6-Tribromoaniline (1.80 g, 5.61 mmol), 4-(methoxycarbonyl)phenylboronic acid (5.63 g, 31.3 mmol), K<sub>2</sub>CO<sub>3</sub> (1.16 g, 8.42 mmol), 170 mL 1,4-dioxane, and 10 mL H<sub>2</sub>O were added to a pressure vessel equipped with a magnetic stir bar. The resulting mixture was sparged with N<sub>2</sub> gas for 30 min. Pd(PPh<sub>3</sub>)<sub>4</sub> (0.901 g, 0.842 mmol) was added into the mixture, the vessel was sealed, and the mixture was heated to 110 °C for 48 hr. After cooling the reaction mixture to room temperature the solvent was removed under reduced pressure. The residue was dissolved in

200 mL CH<sub>2</sub>Cl<sub>2</sub> and washed with H<sub>2</sub>O (3×200 mL) followed by brine (300 mL). The organic layer was dried over anhydrous Na<sub>2</sub>SO<sub>4</sub>. The crude product was subjected to column chromatography (hexanes/ethyl acetate) to yield a light yellow solid (2.25 g, yield 83.2 %). <sup>1</sup>H NMR (500 MHz, CDCl<sub>3</sub>) δ 8.18 (*d*, 4H, *J* = 8.32 Hz), 8.06 (*d*, 2H, *J* = 8.32 Hz), 7.69-7.62 (*m*, 6H), 7.46 (*s*, 2H), 3.96 (*s*, 6H), 3.93 (*s*, 3H). HRMS (EI) calcd for C<sub>30</sub>H<sub>25</sub>NO<sub>6</sub> (*m/z*): 495.1682; found: 495.1680. The solid (2.00 g, 4.03 mmol), KOH (2.6 g, 40.0 mmol), 1,4-dioxane (80 mL), and H<sub>2</sub>O (20 mL) were added into a pressure vessel. The resultant suspension was heated to 110 °C for 12 hr. After cooling to room temperature the reaction mixture was filtered and solvent was removed under reduced pressure. The residue was dissolved in H<sub>2</sub>O (150 mL) and the solution was acidified with concentrated HCl *via* drop-wise addition until pH of the solution was 1. The target compound was collected by filtration, washed thoroughly with H<sub>2</sub>O, and dried under vacuum to afford H<sub>3</sub>-ATB (yield 1.65 g, 90.1%). <sup>1</sup>H NMR (500 MHz, DMSO-*d*<sub>6</sub>): δ 12.97 (*br*, 3H), 8.06 (*d*, 4H, *J* = 8.32 Hz), 7.94 (*d*, 2H, *J* = 8.51 Hz), 7.81 (*d*, 2H, *J* = 8.51 Hz), 7.70 (*d*, 4H, *J* = 8.32 Hz), 7.48 (*s*, 2H), 4.70 (*br*, 2H). <sup>13</sup>C NMR (125 MHz, DMSO-*d*<sub>6</sub>): 167.27, 167.18, 143.97, 143.70, 141.99, 129.99, 129.93, 129.63, 129.41, 128.54, 128.36, 127.78, 126.77, 125.72. HRMS (EI) calcd for C<sub>27</sub>H<sub>19</sub>NO<sub>6</sub> (*m/z*): 453.1212; found: 453.1230.

*Synthesis of MOF-177-NH<sub>2</sub>:*

H<sub>3</sub>-ATB (25.0 mg, 0.055 mmol) and Zn(NO<sub>3</sub>)<sub>2</sub>·6H<sub>2</sub>O (43.2 mg, 0.145 mmol) were dissolved in 5.7 mL of anhydrous *N,N*-dimethylformamide. The mixture was sonicated for 15 min and the solution was clarified by filtration through a glass wool plug. The reaction mixture was heated to 85 °C. After 20 hr, colorless block-shaped crystals of a single phase were obtained. After cooling to room temperature the product was isolated by decanting the mother liquor and



washing with fresh DMF (3×15 mL). The yield of the reaction determined from the weight of the solvent-free material (26.0 mg) is 40.1% based on H<sub>3</sub>-ATB.

*Synthesis of UMCM-306:*

H<sub>3</sub>-ATB (25.0 mg, 0.055 mmol), terephthalaldehyde (11.0 mg, 0.0822 mmol), and Zn(NO<sub>3</sub>)<sub>2</sub>·6H<sub>2</sub>O (43.2 mg, 0.145 mmol) were dissolved in 5.7 mL of anhydrous *N,N*-dimethylformamide. The mixture was sonicated for 15 min and the solution was clarified by filtration through a glass wool plug. The reaction mixture was heated to 85 °C. After 24 hr, yellow colored rod-shaped crystals of a single phase were obtained. After cooling to room temperature, the product was isolated by decanting the mother liquor and washing with fresh DMF (3×15 mL). The yield of the reaction determined from the weight of the solvent-free material (20.5 mg) is 36.5% based on H<sub>3</sub>-ATB.

*Synthesis of UMCM-307:*

H<sub>3</sub>-ATB (44.0 mg, 0.097 mmol), anthracene-9,10-dialdehyde (11.4 mg, 0.0492 mmol), and Zn(NO<sub>3</sub>)<sub>2</sub>·6H<sub>2</sub>O (84.5 mg, 0.284 mmol) were dissolved in 14.0 mL of anhydrous *N,N*-dimethylformamide. The mixture was sonicated for 15 min and the solution was clarified by filtration through a glass wool plug. The reaction mixture was heated to 85 °C. After 40 hr, orange colored rod-shaped crystals of a single phase were obtained. After cooling to room temperature, the product was isolated by decanting the mother liquor and washing with fresh DMF (3×15 mL). The yield of the reaction determined from the weight of the solvent-free material (36.8 mg) is 35.8% based on H<sub>3</sub>-ATB.

*Synthesis of UMCM-308:*

H<sub>3</sub>-ATB (6.25 mg, 0.014 mmol), 1,4-diacetylbenzene (21.0 mg, 0.133 mmol), and Zn(NO<sub>3</sub>)<sub>2</sub>·6H<sub>2</sub>O (11.0 mg, 0.037 mmol) were dissolved in 1.25 mL of anhydrous *N,N*-



dimethylformamide. The mixture was sonicated for 30 min and the solution was clarified by filtration through a glass wool plug. The reaction mixture was heated to 85 °C. After 20 hr, colorless rod-shaped crystals were obtained contaminated by ~5% MOF-177-NH<sub>2</sub>. After cooling to room temperature, the product was isolated by decanting the mother liquor and washing with fresh DMF (3×3 mL). The yield of the reaction determined from the weight of the solvent-free material (5.4 mg) is 33% based on H<sub>3</sub>-ATB.

#### **4.4.2 PXRD Patterns of MOF-177-NH<sub>2</sub>, UMCM-306, -307, and -308**

Samples for powder X-ray diffraction were soaked in mineral oil before collection of data. Data were collected on Rigaku R-Axis Spider diffractometer with an image plate detector and CuK $\alpha$  radiation operating in transmission mode. The powder samples were rotated on the goniometer in  $\varphi$  and oscillated in  $\omega$  to minimize preferred orientation.

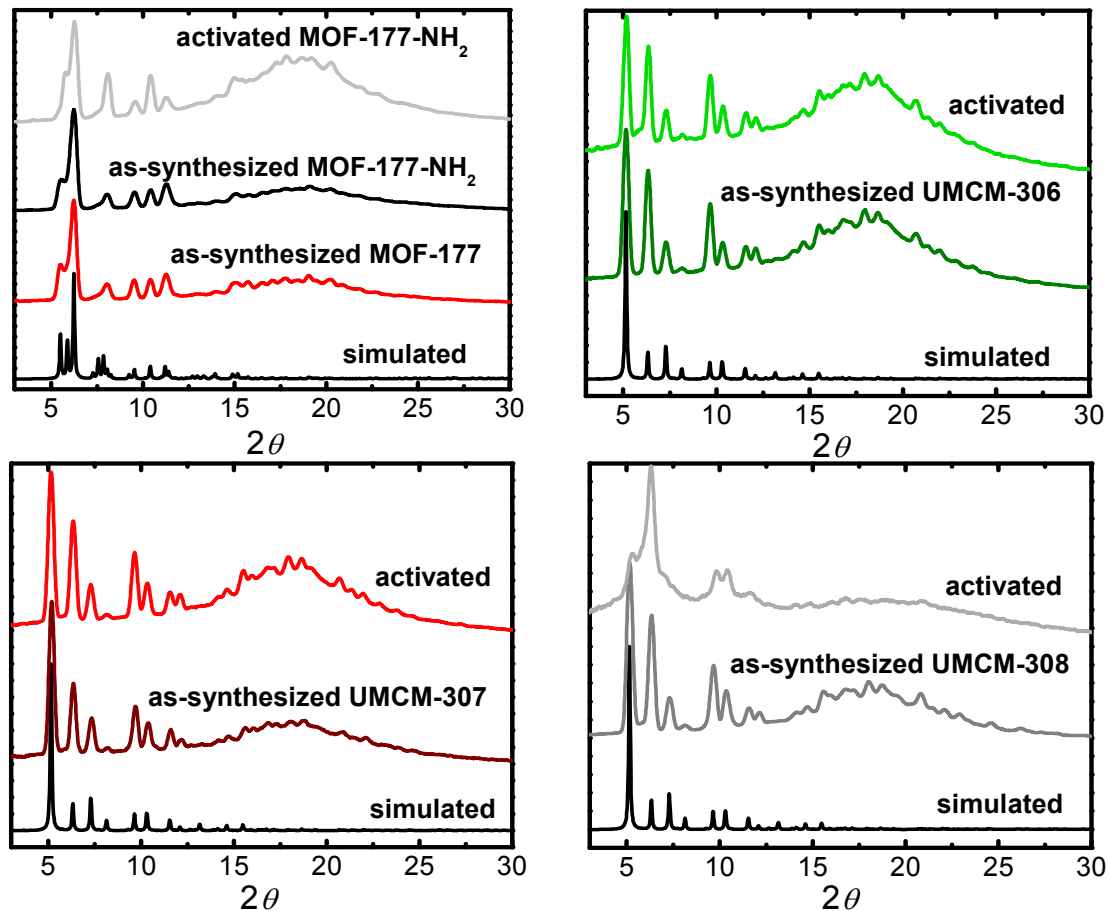


Figure 4. 7. Comparison of simulated and as-synthesized PXRD patterns of materials.

#### 4.4.3 Single Crystal X-ray Diffraction for UMCM-306

Crystals of UMCM-306 exchanged in  $\text{CH}_2\text{Cl}_2$  were coated in Paratone N oil. A clear yellow rod-shaped crystal ( $0.12 \text{ mm} \times 0.02 \text{ mm} \times 0.02 \text{ mm}$ ) was mounted on a cryoloop. X-ray diffraction data were collected on a Rigaku AFC10K Saturn 944+ CCD-based X-ray diffractometer equipped with a low temperature device and Micromax-007HF Cu-target micro-focus rotating anode ( $\lambda = 1.54187 \text{ \AA}$ ) operated at 1.2 kW power (crystal-to-detector distance was 42.00 mm) at 233K. A total of 1767 images were collected with an oscillation width of  $1.0^\circ$  in  $\omega$ . The exposure time was 30 sec for the low angle images, 120 sec for high angle images. The integration of the data yielded a total of 126420 reflections to a maximum  $2\theta$  value of  $113.84^\circ$  of

which 3614 were independent and 2675 were greater than  $2\sigma(I)$ . Decay of the crystal during data collection was negligible. The structure was solved by direct methods and refined against all data in the the space group  $P 4_2/m n m$  with  $Z = 2$  for the formula  $C_{50}H_{26}N_2O_{13}Zn_4$  using SHELXL-97 in the Crystal Structure (v. 4.0) software package.<sup>18</sup> All non-hydrogen atoms were refined anisotropically with the hydrogen atoms placed at calculated positions (C-H = 0.93 Å) using a riding model with isotropic thermal parameters 1.2 times that of the attached carbon atom. Full matrix least-squares refinement based on  $F^2$  converged at  $R1 = 0.1647$  and  $wR2 = 0.4256$  based on  $I > 2\sigma(I)$ ,  $R1 = 0.1808$  and  $wR2 = 0.4413$  for all data. The SQUEEZE<sup>19</sup> subroutine of the PLATON program suite was used to address the disordered solvent/oil in the large cavity present in the structure. Additional refinement details are given in the CIF file.

Table 4. 1. Crystal data and structure refinement for UMCM-306

Compound	UMCM-306
Empirical formula	$C_{50}H_{26}N_2O_{13}Zn_4$
Formula Weight	1124.21
Temperature of run	233K
Crystal dimensions	$0.12 \times 0.02 \times 0.02 \text{ mm}^3$
Wavelength	1.54187 Å
Crystal system	Tetragonal
Space group	$P 4_2/m n m$
Unit cell parameters	$a = 24.1097(7) \text{ Å}$ $b = 24.1097(7) \text{ Å}$ $c = 17.0615(12) \text{ Å}$ $9917.5(8) \text{ Å}^3$ $\alpha = 90.00^\circ$ $\beta = 90.00^\circ$ $\gamma = 90.000(3)^\circ$
$Z$	2
Density (calculated)	$0.376 \text{ g/cm}^3$
Absorption coefficient	$0.685 \text{ mm}^{-1}$
$F(000)$	1128
Theta range for data collection	2.60 to 56.90
Index ranges	$-26 \leq h \leq 26$ , $-26 \leq k \leq 26$ , $-18 \leq l \leq 17$
Reflections collected	126420
Independent reflections	3614 $R(\text{int}) = 0.0812$
Completeness to highest theta	100 %
Absorption correction	Multi-scan
Max. and min. transmission	0.675 and 0.464
Refinement method	Full-matrix least-squares on $F^2$

Data/ Restraints/ parameter	3614 / 0 / 151
Goodness of fit on $F^2$	1.828
Final R indices $I > 2\sigma(I)^{a,b}$	R1 = 0.1647, wR2 = 0.4256 <sup>a,b</sup>
R indices (all data) <sup>a,b</sup>	R1 = 0.1808, wR2 = 0.4413

a)  $wR2 = \frac{|\sum w(|Fo|^2 - |Fc|^2)|}{\sum w(Fo^2)^{1/2}}$ ,  $w = 1 / (\sigma^2(Fo^2) + (mP)^2 + nP)$  and  $P = \max(Fo^2, 0) + 2Fc^2 / 3$  ( $m$  and  $n$  are constants);  $\sigma = \sum w(Fo^2 - Fc^2)^2 / (n - p)^{1/2}$  b)  $R1 = \frac{\sum ||Fo| - |Fc||}{\sum |Fo|}$

#### 4.4.4 $^1H$ NMR Spectroscopic Data of Digested MOF-177-NH<sub>2</sub>, UMCM-306, -307, and -308

Solvent free materials were digested in 35 wt% DCl in D<sub>2</sub>O diluted with DMSO-*d*<sub>6</sub> solution before performing  $^1H$  NMR spectroscopic experiments.

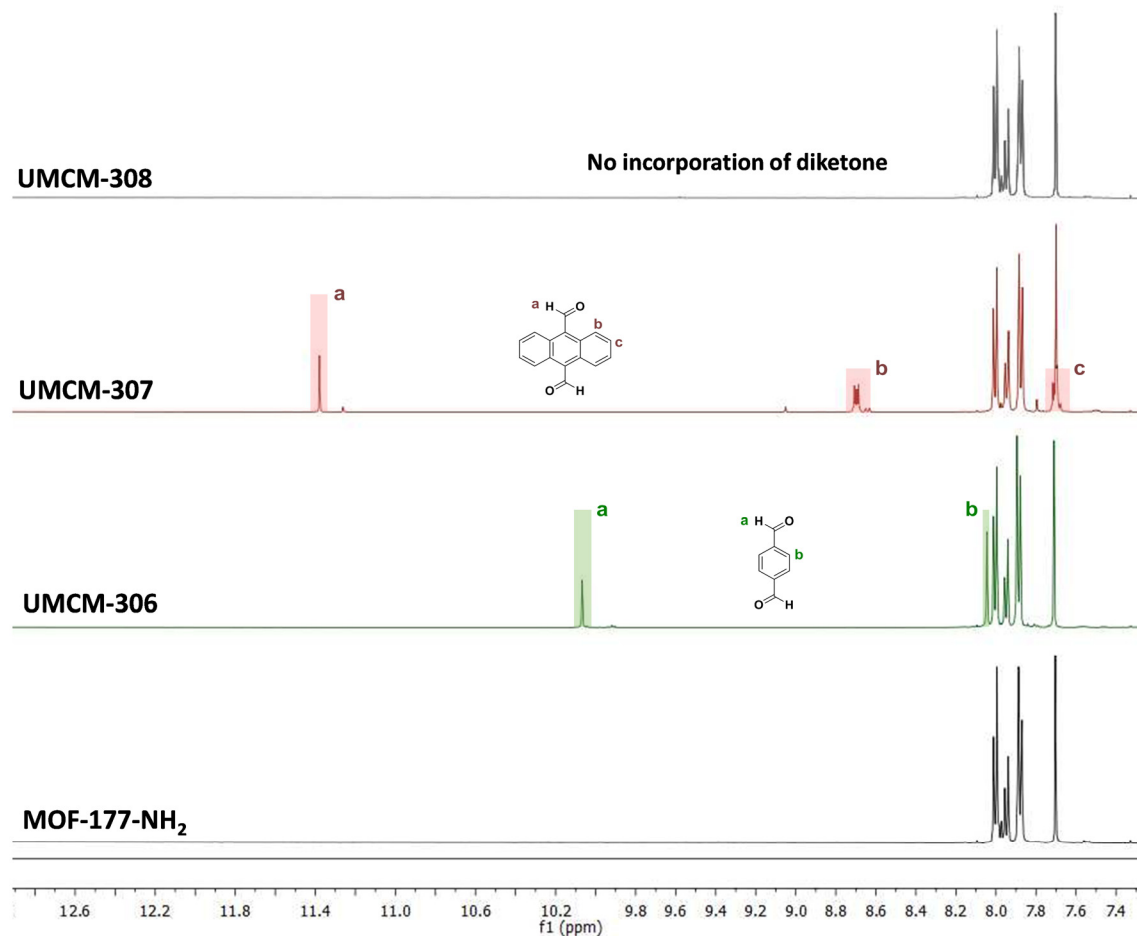


Figure 4. 8.  $^1H$  NMR spectra of digested MOF-177-NH<sub>2</sub>, UMCM-306, -307, and -308.

#### 4.4.5 Raman Spectroscopic Data of MOF-177-NH<sub>2</sub>, UMCM-306, and -308

Raman spectroscopic experiments were performed using a Renishaw inVia Raman Microscope equipped RenCam CCD detector, 633 nm laser, 1800 lines/nm grating, and 50  $\mu\text{m}$  slit. Spectra were collected in extended scan mode in the range of 4000-100  $\text{cm}^{-1}$  and then analyzed using Wire 3.4 software package. Calibration was performed for all experiments using a silicon standard.

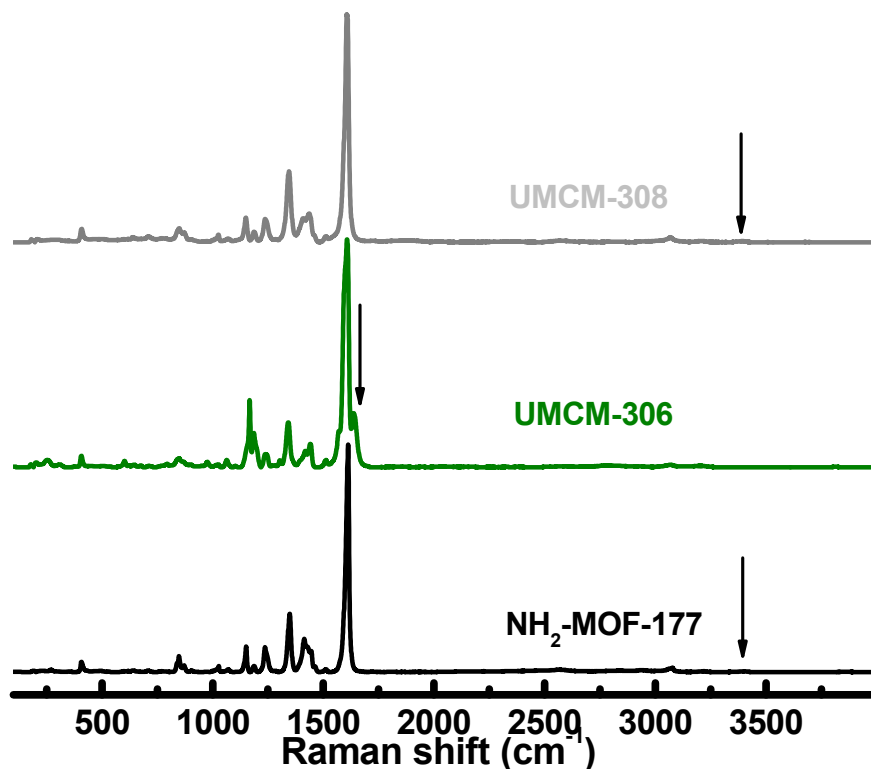


Figure 4. 9. Full Raman spectra of materials showing presence of imine C=N stretching at 1634  $\text{cm}^{-1}$  in UMCM-306 and NH<sub>2</sub> stretching in MOF-177-NH<sub>2</sub> and UMCM-308 at  $\sim 3400 \text{ cm}^{-1}$ .

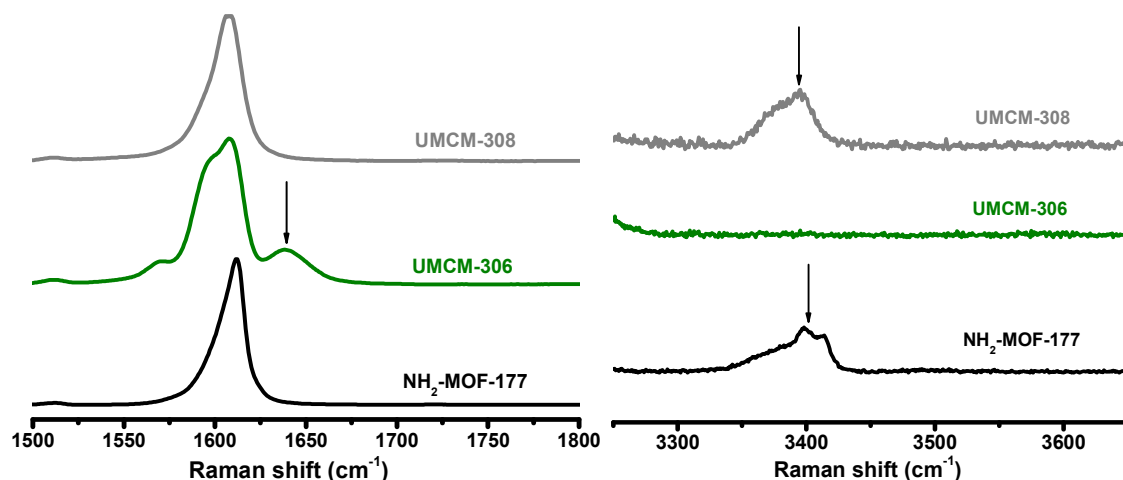
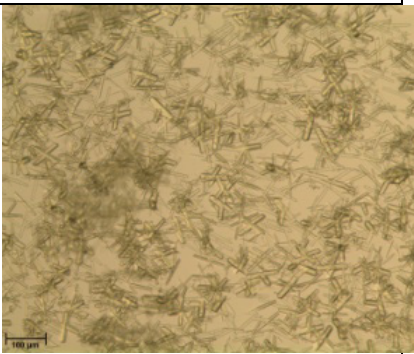
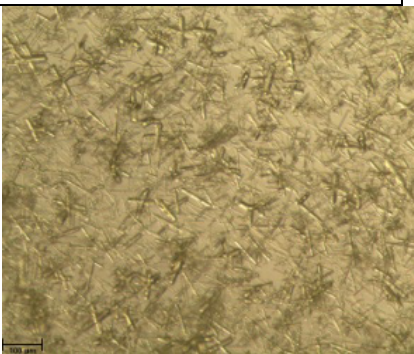
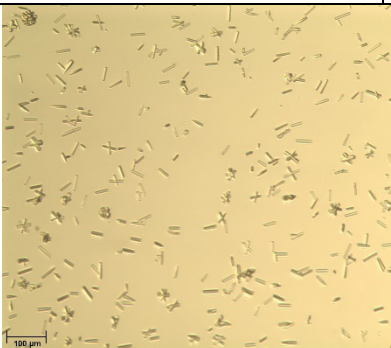
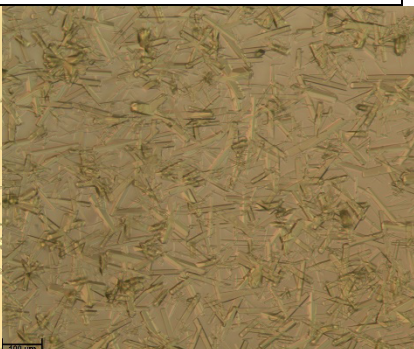
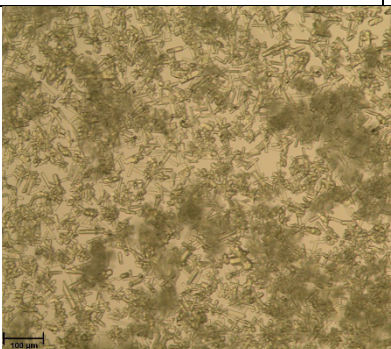
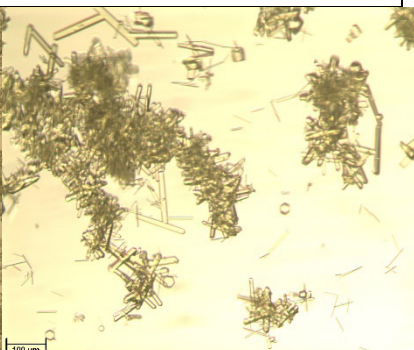
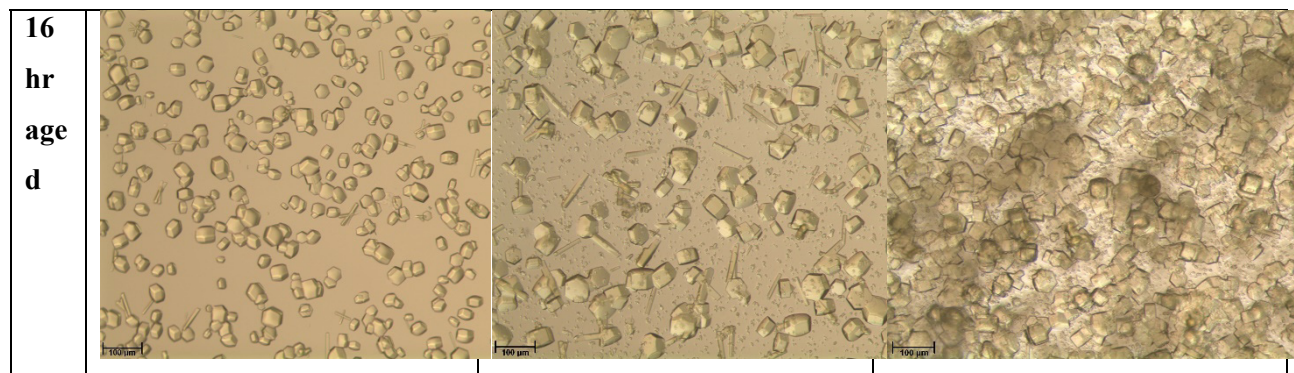


Figure 4. 10. Partial Raman spectra of materials showing presence of imine C=N stretching at  $1634\text{ cm}^{-1}$  in UCMCM-306 and  $\text{NH}_2$  stretching in MOF-177- $\text{NH}_2$  and UCMCM-308 at  $\sim 3400\text{ cm}^{-1}$ .

#### 4.4.6 Microscopic Images after Aging Experiments

Five different vials containing  $\text{Zn}(\text{NO}_3)_2 \cdot 6\text{H}_2\text{O}$  (14.5 mg, 0.048 mmol) and DMF (1.5 mL) were preheated (aged) at  $85\text{ }^\circ\text{C}$  for 1, 2, 4, 8, 16 hours.  $\text{H}_3\text{-ATB}$  (8.33 mg, 0.018 mmol) and terephthalaldehyde (3.67 mg, 0.027 mmol) dissolved in 0.5 mL fresh DMF were added in each pre-heated vial through septum lid using a syringe. The reaction mixtures were again heated to  $85\text{ }^\circ\text{C}$  and analyzed after 6, 10, and 22 hr *via* optical microscopy. The images were taken with a Spot Insight Color camera fixed to a Leica DMIL microscope. All scale bars indicate a dimension of  $100\text{ }\mu\text{m}$ .

	After 6 hr in oven	After 10 hr in oven	After 22 hr in oven
1 hr age d	No crystals	No crystals	
2 hr age d	No crystals	No crystals	
4 hr age d	No crystals		
8 hr age d	No crystals		



#### 4.4.7 TGA Traces of MOF-177-NH<sub>2</sub>, UMCM-306, -307, and -308

Thermogravimetric analyses were performed on a TA Q50 equipment. Samples were activated before experiments. The temperature was ramped from 25 °C to 600 °C with a rate of 2 °C/ min under a flow of N<sub>2</sub> gas.



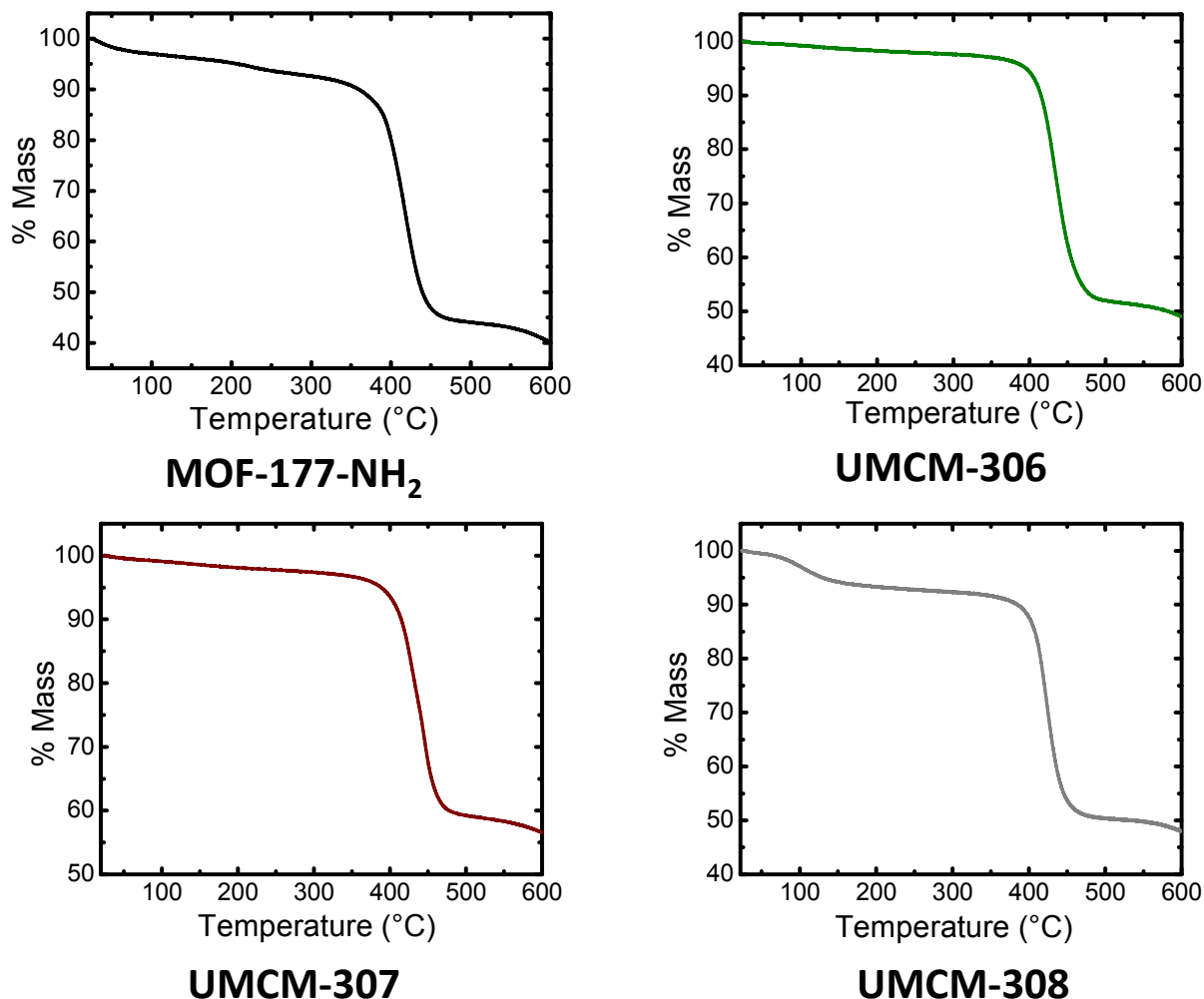


Figure 4. 11. TGA traces of activated materials.

#### 4.4.8 Activation of Materials and Gas Sorption Measurements

All materials were exchanged in fresh DMF for 24 hr before flowing supercritical CO<sub>2</sub> activation.<sup>20</sup>

N<sub>2</sub> adsorption/desorption isotherms were measured volumetrically at 77K in the range of  $1.00 \times 10^{-5} \leq P/P_0 \leq 1.00$  with an Autosorb-1C outfitted with the micropore option by Quantachrome Instruments (Boyton Beach, Florida, U.S.A.) running version 1.2 of the ASwin

software package. Ultra-high purity He (99.999%, for void volume determination) and N<sub>2</sub> (99.999%) were purchased from Cryogenic Gases and used as received.

#### 4.5 References

1. H. Li, M. Eddaoudi, M. O'Keeffe, O. M. Yaghi, *Nature*, 1999, **402**, 276-279.
2. A. P. Côté, A. I. Benin, N. W. Ockwig, M. O'Keeffe, A. J. Matzger, O. M. Yaghi, *Science* 2005, **310**, 1166-1170.
3. a) S. Hausdorf, J. Wagler, R. Moßig, F. O. R. L. Mertens, *J. Phys. Chem. A*, 2008, **112**, 7567-7576; b) S. Hausdorf, F. Baitalow, J. Seidel, F. O. R. L. Mertens, *J. Phys. Chem. A*, 2007, **111**, 4259-4266.
4. T. E. Reich, K. T. Jackson, S. Li, P. Jena, H. M. El-Kaderi, *J. Mater. Chem.*, 2011, **21**, 10629-10632.
5. D. Beaudoin, T. Maris, J. D. Wuest, *Nat. Chem.*, 2013, **5**, 830-834.
6. a) F. J. Uribe-Romo, J. R. Hunt, H. Furukawa, C. Klöck, M. O'Keeffe, O. M. Yaghi, *J. Am. Chem. Soc.*, 2009, **131**, 4570-4571 b) C. R. DeBlase, K. E. Silberstein, T.-T. Truong, H. D. Abruña, W. R. Dichtel, *J. Am. Chem. Soc.*, 2013, **135**, 16821-16824.
7. F. J. Uribe-Romo, C. J. Doonan, H. Furukawa, K. Oisaki, O. M. Yaghi, *J. Am. Chem. Soc.*, 2011, **133**, 11478-11481.
8. In this context it should be noted that *in situ* ligand formation from irreversible covalent coupling in tandem with coordination chemistry has been demonstrated. See for example: Zhao, D.; Yuan, D.; Yakovenko, A.; Zhou, H.-C. *Chem. Commun.*, 2010, **46**, 4196.
9. H. K. Chae, D. Y. Siberio-Perez, J. Kim, Y. Go, M. Eddaoudi, A. J. Matzger, M. O'Keeffe, O. M. Yaghi, *Nature*, 2004, **427**, 523-527.
10. S. R. Caskey, A. G. Wong-Foy, A. J. Matzger, *Inorg. Chem.*, 2008, **47**, 7751-7756.
11. A role for diethylamine as a competitive species for imine formation cannot be ruled out as an additional contributing factor.
12. To best of our knowledge, ketimine COFs are absent from the literature.
13. As we have noted earlier, and in contrast to its misuse in the field, such framework materials must not be termed "polymorphs". Polymorphs have a strict isomeric relationship that is not easily satisfied in porous material containing varying degrees of solvation. This fact motivates the use of the present term "polymorphic frameworks". The distinction is critical because, for example, stability ordering of polymorphic framework materials is expected to be solvent dependent whereas this is forbidden for true polymorphs. In fact the closest molecular analogy is in solvate stability where solvate inclusion engenders relative stability relationship that can depend strongly on solvent and temperature. In molecular compounds such relationships are sometimes termed "pseudopolymorphic". Thus by this logic one could consider the different topologies of coordination polymers to be pseudopolymorphs. However, such a term is esoteric and subject to debate even within the small molecule community and so "polymorphic framework" is preferred.
14. V. A. Blatov, L. Carlucci, G. Ciani, D. M. Proserpio, *CrystEngComm*, 2004, **6**, 378-395.
15. Z. Zhang, M. J. Zaworotko, *Chem. Soc. Rev.*, 2014, **43**, 5444-5455.

16. J. Rouquerol, P. Llewellyn, F. Rouquerol, in *Studies in Surface Science and Catalysis, Vol. Volume 160* (Eds.: F. R.-R. J. R. P.L. Llewellyn, N. Seaton), Elsevier, 2007, pp. 49-56.
17. The surface area of UMCM-308 is significantly lower than the predicted one which is indicative of the loss of the structural integrity of the material upon activation as judged by PXRD pattern.
18. G. M. Sheldrick, *SHELXS '97 and SHELXL '97*. (University of Göttingen, Germany, 1997).
19. a) A. L. Spek, *J. Appl. Cryst.*, 2003, **36**, 7-13 ; b) A. L. Spek, *Acta Cryst. D65*, 2009, v. **51012**, 148-155.
20. B. Liu, A. G. Wong-Foy and A. J. Matzger, *Chem. Commun.*, 2013, **49**, 1419-1421.